University of California
Santa Barbara

Understanding Membrane Formation in Nonsolvent-Induced Phase Separation

A dissertation submitted in partial satisfaction
of the requirements for the degree

Doctor of Philosophy
in
Chemical Engineering

by

Jan Ulric Macaraeg Garcia

Committee in charge:

Professor Glenn H. Fredrickson, Chair
Professor Hector D. Ceniceros
Professor M. Scott Shell
Professor Todd M. Squires

December 2020

The Dissertation of Jan Ulric Macaraeg Garcia is approved.

Professor Hector D. Ceniceros

Professor M. Scott Shell

Professor Todd M. Squires

Professor Glenn H. Fredrickson, Committee Chair

December 2020

Understanding Membrane Formation in Nonsolvent-Induced Phase Separation

by

Jan Ulric Macaraeg Garcia

For my Lola.

Acknowledgements

When I began my PhD, I mistakenly believed that scientific discovery was the goal of the program. Now five years wiser, I finally understand that the research project was only the means to an end. I am the real product of my PhD: my development as a scientist, a teacher, a presenter, a writer, a manager, and a critical thinker were the real goals—and I owe my development to so many people these past five years.

First and foremost, I will be forever grateful to Professor Glenn Fredrickson. He accepted me into his group despite my challenges with mathematics and inexperience as a coder. He taught me how to think critically, to not believe claims without reason, even from someone more accomplished than me. He gave me countless opportunities to travel the world—from Sweden to Japan—and he never turned down any of my reasonable crazy ideas, like mentoring two high-school students to do PhD-level work. He never dissuaded my wacky presentation style. Most of all, he showed me, by example, what it takes to become a world-renowned scientist. There have been myths circling around the department and in conferences that Glenn does not sleep—I have not found evidence to the contrary. For these past five years, and for everything to come in the future, thank you, Glenn.

I am grateful to my committee, Professors Hector Ceniceros, Scott Shell, and Todd Squires. My research progress in annual meetings was marginal, yet I only received encouragement and words of wisdom, specifically on how to multi-task and how to become a more disciplined writer. I thank you not only for giving me tips on becoming a better scientist, but also exemplifying what it takes to become a great teacher.

I would like to thank Dr. Kris Delaney. His sharp mind and attention to detail always caught my silly mistakes, from illogical thinking, mathematical misformulations, and of course, coding bugs. When I prepare figures for a scientific document and slides for a technical presentation, I always ask myself, "would Kris like this approach?" In his spare time, he implements new software features I need for my research, and even finds performance improvements in the code that nobody knew existed. I also benefited from his great propensity for mentoring students. My research took a sharp turn for the better when he asked me to think about which future version of me I would like to see. I think I picked the right universe. Thank you, Kris.

I would like to thank Prof. Douglas Tree. During his post-doc days in UCSB, he pioneered the membrane project and founded our in-house phase-field software. Needless to say, this PhD would have been impossible without Doug. I also inherited much of Doug's workflow in coding, submitting jobs to the clusters, data analysis scripting, figure preparation, and even writing manuscripts. Doug was also the perfect role model for any PhD student; he gave many unsolicited—but not unwanted—advice, including the nitty-gritty of grad school and academia. I always look to Doug's work as my standard of excellence. Doug, thank you for being my mentor.

I would like to thank Tatsuhiro Iwama-san. He has always been patient with my slow progress in software feature development and demonstrating the formation of the asymmetric pore-size distribution. Despite my shortcomings, he still invited me for an internship in Asahi Kasei to complement my training. I now appreciate the difficulties of experimental work and the real challenges and motivations in understanding membrane formation. I also saw a whole new world. The Japanese took pride in their work, and they approached it with a great sense of community. I tried to adopt as much as I could

from the Japanese workstyle to improve my work, but it was challenging to find a cheap steady supply of Japanese sweets and energy drinks in Santa Barbara. I also thank Tatsu for making my stay in Japan as comfortable as possible. He forced his colleagues to be my friends, and it worked. He also encouraged my long-weekend sightseeing travels by bullet train. Perhaps in a couple of years, I could write this whole paragraph in Japanese. Thank you, Tatsu.

I would like to thank our collaborators from the University of Texas, Austin. Professor Benny Freeman has been very gracious and has always promoted my work not only within MWET but also outside academia. Alexander Bridge has been an enthusiastic collaborator, always willing to share his insights as an expert polymer membrane experimentalist. I still look forward to co-authoring a publication with both of you in the future.

I would like to thank Prof. Douglas Tree's students, especially Rami Alhasan, for their help in developing new features and debugging the phase-field code.

I would like to thank my interns, Joshua Lee, Eva Chan, and James Raj, who contributed not only to my research but perhaps even more to my development as a teacher and manager. Thank you for your patience with my inexperience and it is my honor and pleasure to promote your accomplishments.

I would like to thank Dr. Mukul Tikekar for serving as my personal mentor in fluid dynamics and continuum mathematics. I also appreciate his help in developing new features in and debugging the phase-field code. His mental acuity never fails to come up with an alternative solution to a perplexing problem. I look forward to your implementation of viscoelasticity in the phase-field software.

I would like to thank Mike Burroughs for our late-night discussions about the ideal research career and deciding between industry and academia. I also appreciate how you always looked out for me, like when we escaped the Thomas Fire with Patrice to San Luis Obispo. Nothing builds friendship stronger than adversity.

I would like to thank Dr. Jimmy Liu for serving as my personal mentor in mathematics, coding, and logical thinking. Jimmy showed me that assuming the best in people and following one's interests will lead to a happy life.

I would like to thank Dr. Manik Goyal for teaching me the beauty of living a balanced life. I have never met someone so productive in his work yet always finds the time for personal development and socialization.

I would like to thank Dr. Kevin Shen for his friendship and helping me with expanding my professional network. I will never forget our day stuck in Denver after COVID cancelled March meeting.

I would like to thank Dr. Carol Tsai for welcoming me to the group with her kindness. She exemplifies resilience—a most admirable trait that I try to adopt in my own life. Thank you for the opera fun facts and the bundt cakes.

I would like to thank Prof. Joshua Lequieu and Dr. Douglas Grzetic for showing me the ways of productivity. Thank you for your friendship and advice in my development as a scientist.

I would like to thank Kimberlee Keithley for nurturing my humanity. Her Valentine's chocolate is still the richest, and her Halloween pumpkin pie the sweetest. Thank you for helping me out in the farm.

I would like to thank Dan Sun for keeping me from insanity during quarantine. She introduced me to authentic Sichuan cuisine and to the joys and sorrows of walking long distances while carrying groceries, especially our midnight walk of terror through the Santa Barbara Airport. Why, Dan, why? Thanks for the laughs. I will never forget your 3D eyes and beautiful gums.

I acknowledge all other members of the GHF ensemble, in the past, present, and future. Though we did not spend much time together during my tenure in Santa Barbara, you contributed to the integral of my PhD, and I look forward to meeting you somewhere down the road of life.

I would like to thank all my friends in Japan, especially Kimiya Murakami-san, Kazu Hirosawa-san, and Tsugumi Ooi-san. I enjoyed our hike to the summit of Hoei-san. Perhaps next time we can go all the way to the top of Mt. Fuji.

I would like to thank Mizuki Kamata for being my secret weapon in understanding Japanese culture, learning the Japanese language, and preparing me for my successful job interviews. I will never forget our trip to Odaiba. Thank you, Mizuki-sensei.

I would like to thank Catherine and Kelsea Vallance for sharing their home with me during the pandemic. I would also like to acknowledge Frieda, Patricia, and Penny who

delivered fresh eggs everyday. Of course, I cannot forget about Onyx and my best friend, Chappy, who never failed to visit me every night for a pet therapy session. I will never forget the softness of your ears, and your addiction to blueberries.

I would like to thank Mommy Gigi, Tito Ormel, Rhamone, Thea, and of course, Mama Erming, for always thinking of my happiness, freezing any delicious leftovers from their first-class parties. I really appreciate your willingness to drive me back-and-forth from Los Angeles to Santa Barbara just to spend time with you and the rest of the Agdeppa clan in Los Angeles.

I would like to thank the Macaraeg family in the Philippines for sending emotional support in my illogical pursuit of a PhD. I would like to especially acknowledge Nanay Jo and Ninang Evelyn for taking care of my beloved Lola in her final days. I regret not being present to say goodbye in person. Thank you.

Finally, I would like to thank my favourite family in the world: Papa, Mama, Kara, and Leom, for supporting me in my adventures away from home. I love you.

Curriculum Vitæ

Jan Ulric Macaraeg Garcia

Education

2020	Ph.D. in Chemical Engineering, University of California, Santa Barbara, United States
2015	M.Sc. in Chemical Engineering, University of Alberta. Canada
2013	B.Sc. in Chemical Engineering, University of Alberta. Canada

Presentations

2020	Modeling membrane formation in nonsolvent-induced phase separation. *Lunch and Learn with Air Liquide Advanced Separations.* Invited Talk. Virtual Seminar.
2020	Arrested mobility and thermal fluctuation effects on the mass transfer induced phase separation of ternary polymer solutions. *American Physical Society March Meeting.* Denver, Colorado.
2019	Coarsening kinetics of ternary polymer solutions with mobility and viscosity contrasts. *American Physical Society March Meeting.* Boston, Massachusetts.

Professional employment

2016-2020	Graduate Student Researcher. Department of Chemical Engineering. UC Santa Barbara, United States.
2019	Research Intern. Asahi Kasei Corporation. Fuji, Shizuoka, Japan.
2012	Research Process Intern. Heavy Oil Technology Development. Shell Canada Ltd. Calgary, Alberta, Canada.
2010	Research Intern. CanmetEnergy. Devon, Alberta, Canada.

Teaching

Winter 2019	Reader. Equilibrium Statistical Mechanics. ChE 210B
Winter 2018	Teaching Assistant. Engineering Thermodynamics. ChE 110A
Winter 2017	Teaching Assistant. Engineering Thermodynamics. ChE 110A

Awards

2016-2019	Natural Sciences and Engineering Research Council of Canada (NSERC) Post-Graduate Scholarship (PGS-D)

2013-2014	Natural Sciences and Engineering Research Council of Canada (NSERC) Canada Graduate Scholarship (CGS-M)
2008-2012	Canada Millennium Scholarship Foundation, National Excellence Award
2008-2012	President's Centenary Entrance Citation, University of Alberta

Publications

JU Garcia, JV Raj, DR Tree, KT Delaney, GH Fredrickson. *Roles of the dope composition and the glass-transition concentration in nonsolvent-induced phase separation.* In preparation.

JU Garcia, DR Tree, T Iwama, KT Delaney, GH Fredrickson. *Coarsening dynamics of ternary polymer solutions with mobility and viscosity contrasts.* In preparation.

JU Garcia, T Iwama, EY Chan, DR Tree, KT Delaney, GH Fredrickson. *Mechanisms of asymmetric membrane formation in nonsolvent-induced phase separation. ACS Macro Letters.* (2020), 9, 11, 1617-1624.

DR Tree, LF Dos Santos, CB Wilson, TR Scott, JU Garcia, GH Fredrickson. *Mass-transfer driven spinodal decomposition in a ternary polymer solution. Soft Matter.* (2019), 15, 461404628.

Abstract

Understanding Membrane Formation in Nonsolvent-Induced Phase Separation

by

Jan Ulric Macaraeg Garcia

Polymer membranes are essential to water security: they purify our drinking water, desalinate seawater into potable water, and treat wastewater before its release to the environment. The separation performance of these membranes is largely determined by their microstructure. An asymmetric microstructure is advantageous: the smaller pores on the feed-side of the membrane enable separation while larger pores deeper into the membrane provide mechanical support without hindering transport of the permeate across the membrane. Nonsolvent-induced phase separation (NIPS) is a typical way to make these asymmetric membranes. In NIPS, a polymer solution film is immersed in a nonsolvent bath, inducing phase separation of the film into a polymer-rich phase that becomes the membrane matrix and a polymer-poor phase that becomes the membrane pores. Due to our limited understanding of NIPS, membrane manufacturers continue to rely on experimental heuristics to link NIPS process parameters to the resulting membrane morphologies.

In this dissertation, we demonstrate the mechanisms of asymmetric membrane formation using phase-field simulations. We show that mass-transfer-induced spinodal decomposition, thermal fluctuations, and structural arrest are essential and sufficient to the formation of asymmetric morphologies. Specifically, we show that the competition between the propagation of the phase-separation and glass-transition fronts determines the degree of pore-size asymmetry of the membrane. We also explore how these formation mechanisms change with the glass-transition concentration and dope composition,

two important parameters in the formulation of NIPS systems.

To complement our study of membrane formation, we also examine coarsening dynamics in the bulk near a glass transition, implemented as a mobility and viscosity contrast between the polymer-rich and polymer-poor phases. In the case of polymer-poor clusters in a polymer-rich matrix, the glass transition imposes structural arrest. In the opposite case, the glass transition changes the transient concentration of the polymer-rich phase, thus leading to a change in shape of the discrete domains. This effect introduces several complexities to the coarsening process, including inversion of the polymer-rich and polymer-poor phases—a phenomenon normally attributed to viscoelastic phase separation.

Contents

Chapter 1

Making Polymer Membranes

1.1 Background

Clean water is essential to life, but water security continues to be a global challenge. Today, three out of ten people lack access to safe drinking water, and six out of ten do not have access to safely-managed sanitation services [1]. As global population and industrial activity continue to grow, expanding our water supply to unconventional sources such as desalination [2, 3] and potable water reuse [4, 5], becomes paramount; this need underscores the importance of water filtration technologies to our quality of life, not only today but for decades to come.

Water filtration can be classified according to membrane pore diameter: microfiltration (0.1 µm - 10 µm), ultrafiltration (10 Å - 1000 Å), and reverse osmosis (3 Å - 5 Å). Microfiltration removes colloids and bacteria ($\sim$ 1 µm), ultrafiltration rejects dissolved proteins and viruses ($\sim$ 1000 Å), and reverse osmosis filters particles as small as monovalent ions ($<$ 10 Å) [6]. Today, these membranes are ubiquitous; they can be found in any industry that uses and produces water: oil and gas, materials, pharmaceuticals, food, wastewater treatment, and of course, production of potable water.

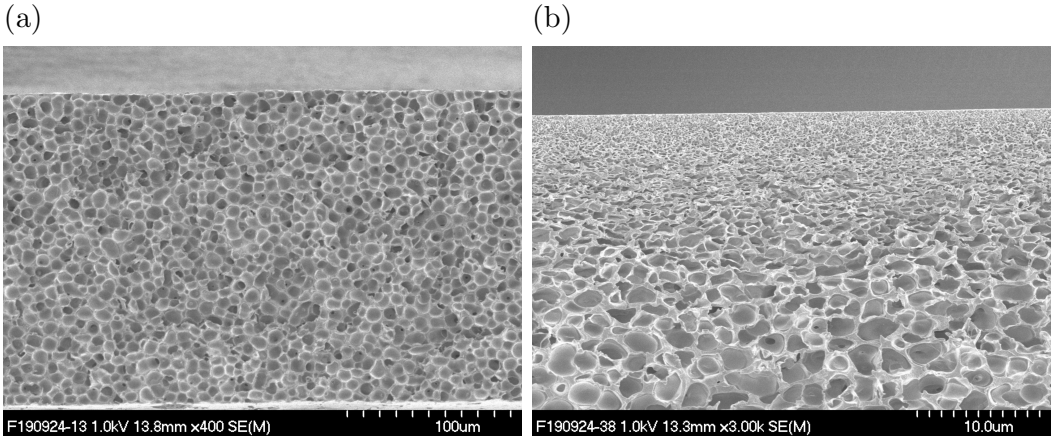

Figure 1.1: Scanning electron microscopy (SEM) images of membrane cross-sections for (a) a symmetric and (b) an asymmetric polymer membrane. Preparation and characterization details of both membranes are described in Appendix A.

The commercial success of membrane separation can be attributed to the development of asymmetric membranes. Figure 1.1 shows a side-by-side comparison of (a) symmetric microstructure whose pores are homogeneous in size and (b) an asymmetric morphology that exhibits a positive pore-size gradient from the top of the film to the bottom. Before Loeb and Sourirajan invented asymmetric membranes in 1964 [7], membrane separation was limited to lab benches due to their low permeate flux. Flux through a symmetric membrane is inversely proportional to its thickness—economics favors the thinnest membranes possible. However, membranes need finite thickness for structural integrity. Balancing these two requirements is challenging for symmetric membranes—and is only possible for membranes of large enough pores. The asymmetric structure solves this trade-off problem: a thin layer of small pores enables separation while a thick layer of large pores provides mechanical support without diminishing the flux. Today, symmetric membranes are limited to microfiltration while asymmetric membranes are used for ultrafiltration and as the porous support for reverse osmosis.

Asymmetric membranes can be made in two ways [8]. Membranes built from a single material are made by phase inversion—the transformation of a one-phase polymer

solution into a two-phase mixture: a polymer-rich phase that eventually solidifies, forming the membrane matrix, and a polymer-poor phase that in the end, becomes the membrane pores. The term "phase inversion" describes how the polymer transforms from the liquid state to the solid membrane matrix—simply put, phase inversion is phase separation followed by solidification [9]. Alternatively, asymmetric membranes can be formed as composite thin films. Composite membranes consist of two different materials—one for the selective layer and the other for the porous support—joined together by solution coating or interfacial polymerization [10]. These techniques allow tighter control of the selective layer's thickness, enabling higher flux. Despite this advantage, composites have not supplanted phase inversion membranes for two reasons. First, composite membranes require multiple fabrication steps, making their production less economical. Second, the composite's porous support is in fact, a phase inversion membrane on its own. Thus, phase inversion techniques are essential to the fabrication of all asymmetric membranes.

Phase inversion techniques are identified with their method of phase separation [6]. The simplest procedure is to cast a hot polymer solution and allow it to cool down to room temperature. The key to this process—called thermally induced phase separation (TIPS)—is to choose a substance that acts as a solvent in high temperatures but acts as a nonsolvent in room temperature. Control of membrane morphology relies heavily on cooling rates. In practice, TIPS is normally used for making symmetric membranes—however, it can be used to make asymmetric membranes from materials that cannot be processed with other techniques [6]. Instead of relying on temperature, other methods induce phase separation by the introduction of nonsolvent. In solvent evaporation, a polymer is dissolved in a mixture of a volatile solvent and a non-volatile nonsolvent. After casting, the film is allowed to dry—evaporation of the volatile solvent enriches the film in nonsolvent, causing the membrane to precipitate. In another technique, called vapor induced phase separation (VIPS) [11], the nonsolvent is absorbed into the film from

the atmosphere. Most applications of VIPS use water as the nonsolvent. As VIPS relies on vapor absorption, phase separation takes longer to complete, contrasting VIPS with liquid nonsolvent induced phase separation (NIPS) [12, 13]. In NIPS, the cast polymer solution film is immersed in a nonsolvent bath. Nonsolvent enters the film, displacing solvent; the film is enriched in nonsolvent, causing phase separation. After its invention in 1964 [7], manufacturers quickly adopted NIPS and developed it by systematic trial and error [6].

Today, NIPS users follow well-established heuristics with limited understanding of the underlying physics. This approach is not adequate in explaining the various morphologies found in NIPS membranes. In addition to the asymmetric pores shown in Figure 1.1, membrane makers often have to consider the formation of macrovoids [14]—large, elongated pores that reduce the membrane's mechanical integrity. To further complicate matters, macrovoids come in various shapes and sizes. As separation performance is closely tied to membrane structure, determining how fabrication leads to these various morphologies is essential. Industry needs to gain fundamental understanding of NIPS to design membranes for optimal separations.

The NIPS process was first explained by Strathmann and co-workers by tracing the average composition of the film on top of equilibrium phase diagrams for the polymer-nonsolvent-solvent system [15, 16, 17]. Although conceptually helpful, their approach presents an oversimplification as precipitation rates are not captured in their description. Precipitation rates should change with film depth—otherwise, asymmetric membrane structures would not be observed. Smolders et al. [18, 19, 20] argued that upon immersion, the top of the film precipitates first. This precipitation is fast—not giving enough time for domain coarsening, resulting in very small pores. The precipitated top layer then acts as a barrier to the loss of solvent and gain of nonsolvent for the rest of the film. Thus, precipitation rate decreases from the top of the film to the bottom. As

precipitation rate decreases, pore size increases due to more coarsening before solidification. Unfortunately, these precipitation paths are difficult to observe experimentally. In response, one-dimensional mass transfer models of the immersed film have been developed to quantify precipitation delay and polymer concentrations immediately before phase separation [21, 22, 23, 24, 25, 26, 27, 28]. However, prediction of membrane microstructures remained out of reach since phase separation kinetics were not treated in these mass-transfer models.

In Chapter 2, we will outline the derivation of our phase-field model to simulate the formation of membrane microstrustructures in NIPS. In Chapter 3, we will demonstrate the mechanisms necessary to form asymmetric membrane morphologies. We then consider membrane formation for different dope formulations in Chapter 4. To complement our NIPS studies, we will examine the additional effects of hydrodynamics and a glass transition to bulk phase separation in Chapter 5. Finally, we summarize our findings and include suggestions for future projects in Chapter 6.

1.2 Permissions and Attributions

1. The content of Chapter 3 has previously appeared in *ACS Macro Letters* [29]. It is reproduced here with the permission of the American Chemical Society.

2. The SEM images shown in Figure 1.1 were prepared and characterized in collaboration with Mr. Tatsuhiro Iwama using the facilities of Asahi Kasei Corporation, Fuji, Shizuoka, Japan.

3. The image analyses shown in Figures A.1 and A.2 were prepared in collaboration with Mr. James V. Raj through the Future Leaders in Advanced Materials program of the Materials Research Laboratory, UC Santa Barbara.

Chapter 2

Modeling Membrane Formation

2.1 Background

Nonsolvent-induced phase separation (NIPS) is a typical process to make polymer membranes. In NIPS, a polymer solution is cast into a homogeneous film, then immersed in a nonsolvent bath. The film is enriched in nonsolvent, inducing phase separation of the film to a polymer-rich membrane matrix and the polymer-poor pores. NIPS can be conceptualized as a series of physical phenomena: (1) the mass transfer exchange of solvent and nonsolvent, (2) the phase separation of the film, (3) the coarsening of domains, and (4) the solidification of the polymer-rich phase that fixes the membrane microstructure. Strathmann and co-workers [15, 17] were the first to rationalize membrane formation by tracking a fictitious time-dependent film composition profile through a ternary (polymer, nonsolvent, solvent) phase diagram that shows the compositions where the film remains homogeneous, phase separates, or solidifies. Building on this concept, several groups derived 1D mass transfer models to predict film composition profiles and to estimate the delay time between the immersion of the film and the onset of phase separation [21, 22, 23, 24, 25, 26, 27, 28]. The studies that followed then tackled

microstructure prediction in 2D. These studies treated mass transfer and phase separation simultaneously using various simulation methods in the mesoscale: lattice Boltzmann, [30] smoothed particle hydrodynamics, [31] and phase-field simulations. [32, 33, 34] Though these studies predicted mass-transfer-induced pore formation, they fell short of explaining the formation of important microstructural features. In particular, none of the simulations so far have shown microstructures where pore sizes increase from the film-bath interface to the bottom of the film, a feature peculiar to NIPS membranes. Thus, we also need to understand the roles played by domain coarsening and solidification of the polymer-rich phase, parts of the membrane formation process largely left unexplored by previous studies.

2.2 Derivation of a phase-field model

Predicting membrane morphologies requires simultaneous treatment of mass transfer and phase separation kinetics in the mesoscale, making phase-field methods well-suited for the task [35, 36]. A phase-field model describes the microstructure of a material by tracking a set of order parameters, called "phase-fields," that vary continuously in the bulk and across interfacial domains. These methods circumvent the need to explicitly track interfaces, a challenging task for systems of more than one dimension [35]. Phase-field methods also allow access to length-scales and time-scales impractical for particle-based simulations. The challenge, however, lies with the formulation of models consistent with the thermodynamics and kinetics of the specific system of interest.

The two-fluid model—introduced by de Gennes [37] in 1976—presents a rigorous approach to incorporate dynamics into field-based methods. The model consists of two momentum balances—one for each fluid species—connected by drag forces to ensure conservation of momentum for the whole system. Building on this concept, Doi and

Onuki [38] introduced a formalism to derive equations of motion consistent with the two-fluid model. Tree et al. [33] extended this formalism to three components and derived a phase-field model for the NIPS system. Sections 2.2.1, 2.2.2, and 2.2.3, largely follow the development outlined in the methods paper by Tree et al. [33]

2.2.1 Incompressibility assumption

Our model consists of three components: the polymer (p), the nonsolvent (n), and the solvent (s). Each component is described by a scalar volume fraction field, $\phi_i(\boldsymbol{r})$, and a vector-valued velocity field $\boldsymbol{v}_i(\boldsymbol{r})$, where $i \in \{p, n, s\}$, and $\boldsymbol{r}$ represents spatial position. Following Flory's mixing lattice model [39], we characterize the molecular size of each species with its degree of polymerization, N_i, while assuming constant partial molar volume, *i.e.,* constant monomer size for all species. This assumption translates to an incompressible system,

$$\boldsymbol{\nabla} \cdot \boldsymbol{v} = 0 \tag{2.1}$$

where we define the total mixture velocity,

$$\boldsymbol{v} = \sum_{i}^{p,n,s} \phi_i \boldsymbol{v}_i. \tag{2.2}$$

In the equations that follow, the polymer and nonsolvent volume fractions, ϕ_p and ϕ_n, are treated as independent phase-fields, while the solvent volume fraction, ϕ_s, is implicitly determined from the incompressibility assumption, $\phi_s = 1 - \phi_p - \phi_n$.

2.2.2 The Rayleighian

The Rayleighian—a functional of the component velocity fields—is at the center of the Doi-Onuki formalism [38]. Equations of motion can be derived from the Rayleighian by finding its extrema. The Rayleighian functional, R, consists of three terms:

$$R[\{\boldsymbol{v}_i\}] = \dot{F}[\{\boldsymbol{v}_i\}] + \Phi[\{\boldsymbol{v}_i\}] - \lambda G[\{\boldsymbol{v}_i\}] \tag{2.3}$$

where $\dot{F}[\{\boldsymbol{v}_i\}]$ is the time derivative of the Helmholtz free energy of mixing, $\Phi[\{\boldsymbol{v}_i\}]$ is the dissipation potential, and $G[\{\boldsymbol{v}_i\}]$ is a Lagrangian constraint with multiplier, λ.

Free energy

The free energy is the extension of the Flory–Huggins–de Gennes functional [40] for a ternary system:

$$F[\{\phi_i\}] = \frac{k_B T}{\mathrm{v}_0} \int \mathrm{d}\mathbf{r} \left[f_0(\{\phi_i\}) + \frac{1}{2} \sum_i^{p,n,s} \kappa_i \left|\nabla \phi_i\right|^2 \right] \tag{2.4}$$

where k_B is Boltzmann's constant, T is the absolute temperature and v_0 is the reference volume. The integrand has two terms. The first term, $f_0(\{\phi_i\})$, is the homogeneous free energy of mixing defined by the Flory-Huggins model:

$$f_0(\{\phi_i\}) = \sum_i^{p,n,s} \frac{\phi_i}{N_i} \ln \phi_i + \frac{1}{2} \sum_{i \neq j}^{p,n,s} \chi_{ij} \phi_i \phi_j \tag{2.5}$$

where N_i is the degree of polymerization and χ_{ij} are the Flory-Huggins interaction parameters. The second term in Equation 2.4 is the interfacial free energy. In this model, the gradient coefficients, κ_i, are treated as constants. We take the time derivative of

Equation 2.4 to get

$$\dot{F}[\{\boldsymbol{v}_i\}] = \int \mathrm{d}\mathbf{r} \left[\sum_i^{p,n} \phi_i \boldsymbol{v}_i \cdot \boldsymbol{\nabla} \mu_i \right] \tag{2.6}$$

where the chemical potential μ_i is defined as

$$\mu_i = \frac{\delta F}{\delta \phi_i}. \tag{2.7}$$

Dissipation potential

The dissipation potential represents one half of the rate of energy dissipation of the fluid:

$$\Phi[\{\boldsymbol{v}_i\}] = \frac{1}{2} \int \mathrm{d}\mathbf{r} \left[\sum_i^{p,n,s} \zeta_i \left(\boldsymbol{v}_i - \boldsymbol{v}_m \right)^2 + \boldsymbol{\sigma}^{(\mathrm{v})} : \boldsymbol{\nabla} \boldsymbol{v} \right]. \tag{2.8}$$

The dissipation potential includes two terms. The first term is the total drag force in the system. Contribution from each species is computed relative to a friction-centered "medium velocity,"[38]

$$\boldsymbol{v}_m = \frac{1}{\zeta} \sum_i^{p,n,s} \zeta_i \boldsymbol{v}_i \tag{2.9}$$

where ζ_i is the friction per volume of component i, and $\zeta = \sum_i \zeta_i$ is the total friction density. The friction coefficient density, ζ_i, is assumed to be proportional to the monomer friction coefficient and the component density:

$$\zeta_i = \mathrm{v}_0^{-1} \zeta_0 \phi_i \tag{2.10}$$

where the friction coefficient of a monomer of size b in a solvent of viscosity η_s is defined by the Stokes-Einstein relation, $\zeta_0 = \eta_s b$, omitting the factor of 6π for convenience. The second term in Equation 2.8 is the non-local viscous dissipation. The viscous stress

tensor, $\boldsymbol{\sigma}^{(v)}$, is assumed to be quasi-Newtonian:

$$\boldsymbol{\sigma}^{(\mathrm{v})} = \eta(\{\phi_i\})[\boldsymbol{\nabla v} + (\boldsymbol{\nabla v})^{\mathrm{T}}] \tag{2.11}$$

where $\eta(\{\phi_i\})$ is a concentration-dependent solution viscosity.

Lagrangian constraint

Finally, the Lagrangian constraint in the Rayleighian enforces system incompressibility:

$$\lambda G[\{\boldsymbol{v}_i\}] = \int \mathrm{d}\mathbf{r}\, p(\boldsymbol{\nabla} \cdot \boldsymbol{v}) \tag{2.12}$$

where the Lagrange multiplier is defined as the pressure, p.

2.2.3 Model summary

Substituting Equations 2.6, 2.8, and 2.12 into Equation 2.3 fully specifies the Rayleighian. Stationary values of the Rayleighian with respect to $\boldsymbol{v}_i$ give equations of motion for the component velocities. Further mathematical manipulation leads to two convection-diffusion equations (one for each independent phase-field) linked to a momentum equation, with the incompressibility constraint:

$$\frac{\partial \phi_i}{\partial t} + \boldsymbol{v} \cdot \boldsymbol{\nabla} \phi_i = \boldsymbol{\nabla} \cdot \left[\sum_j^{p,n} M_{ij} \boldsymbol{\nabla} \mu_j \right] \tag{2.13}$$

$$-\boldsymbol{\nabla} p + \boldsymbol{\nabla} \cdot \left[\eta(\boldsymbol{\nabla v} + \boldsymbol{\nabla v}^T) \right] = \boldsymbol{\nabla} \cdot \boldsymbol{\Pi} \tag{2.14}$$

$$\boldsymbol{\nabla} \cdot \boldsymbol{v} = 0 \tag{2.15}$$

where the divergence of the osmotic stress tensor is calculated as,

$$\boldsymbol{\nabla} \cdot \boldsymbol{\Pi} = \sum_{i}^{p,n} \phi_i \boldsymbol{\nabla} \mu_i, \tag{2.16}$$

and the matrix of mobility coefficients is given by

$$M_{pp} = \frac{b^2}{\eta_s} \phi_p (1 - \phi_p) \tag{2.17a}$$

$$M_{pn} = M_{np} = -\frac{b^2}{\eta_s} \phi_p \phi_n \tag{2.17b}$$

$$M_{nn} = \frac{b^2}{\eta_s} \phi_n (1 - \phi_n). \tag{2.17c}$$

Note that the final model presented in Eqs 2.13, 2.14, and 2.15 is consistent with the 'Model H' universality class that describes conserved systems with flow, as outlined by Hohenberg and Halperin [41]. The final model can also be simplified to the 'Model B' universality class that describes conserved systems with diffusion-only dynamics by setting $\boldsymbol{v} = \mathbf{0}$. In fact, we take advantage of this simplifiying assumption in most of this dissertation, using the Model B formulation in Chapters 3 and 4. We also compare and contrast the phase separation dynamics due to Model B and due to Model H in Chapter 5.

2.3 Incorporation of glass transition dynamics

As will be discussed in Chapter 3, the glass transition is essential to the formation of asymmetric membranes. Incorporating elastic effects in the model would be ideal; however, doing so would require significant improvements to our numerical methods. Instead, we choose to model a solid as a highly viscous fluid with zero mobilities for all components. However, as shown in Eq 2.17, component mobilities in the current model are scaled by the inverse of the constant solvent viscosity, η_s, as their derivation follows

from the assumption of local Rouse-like friction coefficients,

$$\zeta_i = b^{-3}\zeta_0\phi_i \tag{2.18}$$

where b is the length of a monomer and ζ_0 is the Stokes friction coefficient in a dilute solution of viscosity, η_s:

$$\zeta_0 = \eta_s b. \tag{2.19}$$

Thus, local mobilities are independent of the mixture viscosity in the current model. To link high local mixture viscosity with low local mobilities, we use the concentration-dependent mixture viscosity for the Stokes friction in lieu of the constant solvent viscosity in Eq 2.19:

$$\zeta_0 = \eta(\phi_p)b, \tag{2.20}$$

which then leads to the concentration-dependent-viscosity-scaled mobility model:

$$M_{pp} = \frac{b^2}{\eta(\phi_p)}\phi_p(1-\phi_p) \tag{2.21a}$$

$$M_{pn} = M_{np} = -\frac{b^2}{\eta(\phi_p)}\phi_p\phi_n \tag{2.21b}$$

$$M_{nn} = \frac{b^2}{\eta(\phi_p)}\phi_n(1-\phi_n). \tag{2.21c}$$

With this modification to the component mobilities, we only need to select an appropriate model for the mixture viscosity, $\eta(\phi_p)$, to complete our model for the glass transition. We explored modeling η as an exponential function of the local polymer concentration, $\phi_p(\boldsymbol{r})$, diverging to infinity as $\phi_p(\boldsymbol{r})$ approaches the glass-transition concentration, ϕ_p^*, similar to the well-known Vogel-Fulcher-Tamman-Hesse (VFTH) and Williams-Landel-Ferry (WLF) equations[42]. Unfortunately, as discussed in Section B.6, we encountered numerical challenges in dealing with a function that grows exponentially to

infinity. Instead, we model η as a sigmoidal function of $\phi_p(\boldsymbol{r})$:

$$\eta = \eta_s + \frac{\eta_p - \eta_s}{1 + \exp\left(-\frac{1}{w}\left(\phi_p(\boldsymbol{r}) - \phi_p^*\right)\right)} \tag{2.22}$$

where η_p and η_s represent the pure-component viscosities of the polymer and the solvent, respectively (assuming $\eta_n = \eta_s$), and w controls the width of the sigmoid. A sigmoid mimics the exponential growth of viscosity from the VFTH and WLF models, while bounding its maximum value for computational stability. Selection of the parameters in Eq 2.22 is extensively discussed in Chapters 3, 4, and 5, in context of their respective studies.

2.4 Addition of thermal fluctuations and nondimensionalization

Thermal fluctuations are also essential to membrane formation as will be discussed in Section 3.4. We add mass and momentum fluctuations[41, 43] to the dimensional model:

$$\frac{\partial \phi_i}{\partial t} + \boldsymbol{v} \cdot \boldsymbol{\nabla} \phi_i = \boldsymbol{\nabla} \cdot \left[\sum_j^{p,n} M_{ij} \boldsymbol{\nabla} \mu_j \right] + \alpha_\theta \theta_i(\boldsymbol{r}, t) \tag{2.23}$$

$$-\boldsymbol{\nabla} p + \boldsymbol{\nabla} \cdot \left[\eta(\boldsymbol{\nabla} \boldsymbol{v} + \boldsymbol{\nabla} \boldsymbol{v}^T) \right] = \boldsymbol{\nabla} \cdot \boldsymbol{\Pi} + \alpha_\xi \boldsymbol{\xi}(\boldsymbol{r}, t), \tag{2.24}$$

where α_θ and α_ξ are noise-scaling factors for the mass and momentum fluctuations, θ_i and $\boldsymbol{\xi}$, respectively, that follow fluctuation-dissipation theorem statistics,

$$\langle \theta_i(\boldsymbol{r},t)\rangle = 0 \tag{2.25a}$$

$$\langle \xi_k(\boldsymbol{r},t)\rangle = 0 \tag{2.25b}$$

$$\langle \theta_i(\boldsymbol{r},t)\theta_j(\boldsymbol{r'},t')\rangle = -2k_BT\boldsymbol{\nabla}\cdot[M_{ij}(\boldsymbol{r})\boldsymbol{\nabla}\delta(\boldsymbol{r}-\boldsymbol{r'})]\delta(t-t') \tag{2.25c}$$

$$\langle \xi_k(\boldsymbol{r},t)\xi_l(\boldsymbol{r'},t')\rangle = -2k_BT\delta_{kl}\boldsymbol{\nabla}\cdot[\eta(\boldsymbol{r})\boldsymbol{\nabla}\delta(\boldsymbol{r}-\boldsymbol{r'})]\delta(t-t'), \tag{2.25d}$$

where the indices i and j refer to species components while k and l refer to dimensional components. To nondimensionalize our model, we use R_0, the root-mean-square (RMS) end-to-end distance of a reference polymer with degree of polymerization N_r as the characteristic length scale ($R_0 = bN_r^{1/2}$), τ, the Rouse time of the reference polymer in a solvent of viscosity, η_s, as the characteristic time scale ($\tau = N_r^2\eta_s b^3/k_BT$), b^2/η_s as the characteristic mobility scale, N_rk_BT/b^3 as the characteristic chemical potential scale, and η_s/τ as the characteristic pressure scale; we determined the characteristic scales for the mass and momentum fluctuations as $\theta_c = N_r^{-1/4}/\tau$ and $\xi_c = k_BT/R^{5/2}N_rb^{3/2}$, respectively, as shown in the next section. Following nondimensionalization, we end up with the following model where tildes mark scaled quantities:

$$\frac{\partial\phi_i}{\partial\widetilde{t}} + \widetilde{\boldsymbol{v}}\cdot\widetilde{\boldsymbol{\nabla}}\phi_i = \widetilde{\boldsymbol{\nabla}}\cdot\left[\sum_j^{p,n}\widetilde{M_{ij}}\widetilde{\boldsymbol{\nabla}}\widetilde{\mu}_j\right] + \alpha_\theta N_r^{-1/4}\widetilde{\theta}_i\big(\widetilde{\boldsymbol{r}},\widetilde{t}\big) \tag{2.26}$$

$$-\widetilde{\boldsymbol{\nabla}}\widetilde{p} + \widetilde{\boldsymbol{\nabla}}\cdot\left[\widetilde{\eta}(\widetilde{\boldsymbol{\nabla}}\widetilde{\boldsymbol{v}} + \widetilde{\boldsymbol{\nabla}}\widetilde{\boldsymbol{v}}^T)\right] = N_r\widetilde{\boldsymbol{\nabla}}\cdot\widetilde{\boldsymbol{\Pi}} + \alpha_\xi N_r^{1/4}\widetilde{\boldsymbol{\xi}}\big(\widetilde{\boldsymbol{r}},\widetilde{t}\big) \tag{2.27}$$

where $\widetilde{\theta}_i$ and $\widetilde{\boldsymbol{\xi}}$ are Gaussian-distributed noise that follow nondimensional fluctuation-dissipation theorem statistics,

$$\langle\widetilde{\theta}_i(\widetilde{\boldsymbol{r}},\widetilde{t})\rangle = 0 \tag{2.28a}$$

$$\langle\widetilde{\xi}_k(\widetilde{\boldsymbol{r}},\widetilde{t})\rangle = 0 \tag{2.28b}$$

$$\langle\widetilde{\theta}_i(\widetilde{\boldsymbol{r}},\widetilde{t})\widetilde{\theta}_j(\widetilde{\boldsymbol{r}}',\widetilde{t}')\rangle = -2\widetilde{\boldsymbol{\nabla}}\cdot\Big[\widetilde{M_{ij}}(\widetilde{\boldsymbol{r}})\widetilde{\boldsymbol{\nabla}}\delta(\widetilde{\boldsymbol{r}}-\widetilde{\boldsymbol{r}}')\Big]\delta(\widetilde{t}-\widetilde{t}') \tag{2.28c}$$

$$\langle\widetilde{\xi}_k(\widetilde{\boldsymbol{r}},\widetilde{t})\widetilde{\xi}_l(\widetilde{\boldsymbol{r}}',\widetilde{t}')\rangle = -2\delta_{kl}\widetilde{\boldsymbol{\nabla}}\cdot\Big[\widetilde{\eta}(\widetilde{\boldsymbol{r}})\widetilde{\boldsymbol{\nabla}}\delta(\widetilde{\boldsymbol{r}}-\widetilde{\boldsymbol{r}}')\Big]\delta(\widetilde{t}-\widetilde{t}'), \tag{2.28d}$$

where the indices i and j refer to species components while k and l refer to dimensional components. For computational efficiency in calculating thermal fluctuations, we allow for local dependence of $\widetilde{M_{ij}}$ and $\widetilde{\eta}$ but assume zero gradient:

$$\langle\widetilde{\theta}_i(\widetilde{\boldsymbol{r}},\widetilde{t})\widetilde{\theta}_j(\widetilde{\boldsymbol{r}}',\widetilde{t}')\rangle \approx -2\widetilde{M_{ij}}(\widetilde{\boldsymbol{r}})\widetilde{\nabla^2}\delta(\widetilde{\boldsymbol{r}}-\widetilde{\boldsymbol{r}}')\delta(\widetilde{t}-\widetilde{t}') \tag{2.29a}$$

$$\langle\widetilde{\xi}_k(\widetilde{\boldsymbol{r}},\widetilde{t})\widetilde{\xi}_l(\widetilde{\boldsymbol{r}}',\widetilde{t}')\rangle \approx -2\delta_{kl}\widetilde{\eta}(\widetilde{\boldsymbol{r}})\widetilde{\nabla^2}\delta(\widetilde{\boldsymbol{r}}-\widetilde{\boldsymbol{r}}')\delta(\widetilde{t}-\widetilde{t}'). \tag{2.29b}$$

In Chapters 3 and 4, we limit our scope to diffusion-only dynamics by setting all velocities to zero, simplifying our nondimensional model to

$$\frac{\partial\phi_i}{\partial\widetilde{t}} = \widetilde{\boldsymbol{\nabla}}\cdot\left[\sum_j^{p,n}\widetilde{M_{ij}}\widetilde{\boldsymbol{\nabla}}\widetilde{\mu}_j\right] + \alpha N_r^{-1/4}\widetilde{\theta}_i(\widetilde{\boldsymbol{r}},\widetilde{t}), \tag{2.30}$$

where the nondimensional mobility matrix is defined as

$$\widetilde{M_{pp}} = \phi_p(1-\phi_p)/\widetilde{\eta}(\phi_p) \tag{2.31a}$$

$$\widetilde{M_{pn}} = \widetilde{M_{np}} = -\phi_p\phi_n/\widetilde{\eta}(\phi_p) \tag{2.31b}$$

$$\widetilde{M_{nn}} = \phi_n(1-\phi_n)/\widetilde{\eta}(\phi_p), \tag{2.31c}$$

where $\widetilde{\eta}(\phi_p) = \eta(\phi_p)/\eta_s$. The noise-scaling factor is simplified to $\alpha = \alpha_\theta$ due to the absence of momentum fluctuations in Eq 2.30. While the Stokes equation (Eq 2.14) is not needed in this limit, the local viscosity, $\widetilde{\eta}$, remains as a factor scaling the mobilities in Eq 2.31. In Chapters 3,4, and 5, we report all equations in their nondimensional form, allowing us to drop the tildes for convenience.

2.5 Derivation of the fluctuations scales

We determined the characteristic scale for mass fluctuations, θ_c, by nondimensionalizing Eq 2.25c using the same characteristic quantities in the preceding section.

$$\langle \theta_i(\boldsymbol{r},t)\theta_j(\boldsymbol{r'},t')\rangle = -2k_BT\boldsymbol{\nabla}\cdot[M_{ij}(\boldsymbol{r})\boldsymbol{\nabla}\delta(\boldsymbol{r}-\boldsymbol{r'})]\delta(t-t') \tag{2.32}$$

$$= k_BT\frac{b^2}{\eta_s R_0^5\tau}\Big(-2\widetilde{\boldsymbol{\nabla}}\cdot\Big[\widetilde{M_{ij}}(\widetilde{\boldsymbol{r}})\widetilde{\boldsymbol{\nabla}}\delta(\widetilde{\boldsymbol{r}}-\widetilde{\boldsymbol{r}'})\Big]\delta\big(\widetilde{t}-\widetilde{t'}\big)\Big) \tag{2.33}$$

$$= \frac{k_BT}{N_r^2\eta_s b^3}\frac{N_r^{-1/2}}{\tau}\Big(-2\widetilde{\boldsymbol{\nabla}}\cdot\Big[\widetilde{M_{ij}}(\widetilde{\boldsymbol{r}})\widetilde{\boldsymbol{\nabla}}\delta(\widetilde{\boldsymbol{r}}-\widetilde{\boldsymbol{r}'})\Big]\delta\big(\widetilde{t}-\widetilde{t'}\big)\Big) \tag{2.34}$$

$$= \frac{N_r^{-1/2}}{\tau^2}\Big(-2\widetilde{\boldsymbol{\nabla}}\cdot\Big[\widetilde{M_{ij}}(\widetilde{\boldsymbol{r}})\widetilde{\boldsymbol{\nabla}}\delta(\widetilde{\boldsymbol{r}}-\widetilde{\boldsymbol{r}'})\Big]\delta\big(\widetilde{t}-\widetilde{t'}\big)\Big) \tag{2.35}$$

$$= \theta_c^2\langle\widetilde{\theta}_i\big(\widetilde{\boldsymbol{r}},\widetilde{t}\big)\widetilde{\theta}_j\big(\widetilde{\boldsymbol{r}'},\widetilde{t'}\big)\rangle. \tag{2.36}$$

Thus, we have shown that,

$$\theta_c = \frac{N_r^{-1/4}}{\tau} \tag{2.37}$$

Similarly, we determined the characteristic scale for momentum fluctuations, ξ_c, by nondimensionalizing Eq 2.25d using the same characteristic quantities in the preceding section.

$$\langle \xi_k(\boldsymbol{r},t)\xi_l(\boldsymbol{r'},t')\rangle = -2k_BT\delta_{kl}\boldsymbol{\nabla}\cdot[\eta(\boldsymbol{r})\boldsymbol{\nabla}\delta(\boldsymbol{r}-\boldsymbol{r'})]\delta(t-t') \tag{2.38}$$

$$= \frac{k_BT\eta_s}{R_0^5\tau}\Big(-2\delta_{kl}\widetilde{\boldsymbol{\nabla}}\cdot\Big[\widetilde{\eta}(\widetilde{\boldsymbol{r}})\widetilde{\boldsymbol{\nabla}}\delta(\widetilde{\boldsymbol{r}}-\widetilde{\boldsymbol{r}}')\Big]\delta\big(\widetilde{t}-\widetilde{t}'\big)\Big) \tag{2.39}$$

$$= \frac{(k_BT)^2}{R_0^5N_r^2b^3}\Big(-2\delta_{kl}\widetilde{\boldsymbol{\nabla}}\cdot\Big[\widetilde{\eta}(\widetilde{\boldsymbol{r}})\widetilde{\boldsymbol{\nabla}}\delta(\widetilde{\boldsymbol{r}}-\widetilde{\boldsymbol{r}}')\Big]\delta\big(\widetilde{t}-\widetilde{t}'\big)\Big) \tag{2.40}$$

$$= \xi_c^2\langle\widetilde{\xi}_k\big(\widetilde{\boldsymbol{r}},\widetilde{t}\big)\widetilde{\xi}_l\big(\widetilde{\boldsymbol{r}}',\widetilde{t}'\big)\rangle. \tag{2.41}$$

Thus, we have shown that,

$$\xi_c = \frac{k_BT}{R_0^{5/2}N_rb^{3/2}}. \tag{2.42}$$

2.6 Numerical solution

A semi-implicit time-stepping scheme[36] was implemented to balance computational costs and the need for a numerically stable solution. For spatial discretization, the pseudospectral method[44, 45] was selected for its unparalleled accuracy and ease of implementation using Fast Fourier Transforms (FFT). A full description of these methods and other requisite methods can be found in Tree et al.[33] Here, we briefly describe the solution scheme to give the reader an appreciation for the method.

We begin with our partial differential equation (PDE):

$$\frac{\partial\phi_i(\boldsymbol{r})}{\partial t} = y\big(\{\phi_i\},\{\boldsymbol{\nabla}\phi_i(\boldsymbol{r})\},\ldots,\big\{\boldsymbol{\nabla}^4\phi_i(\boldsymbol{r})\big\}\big), \tag{2.43}$$

where the braces, $\{\ldots\}$, refer to the collection of independent phase-fields. Note that our PDE is fourth-order with respect to spatial derivatives due to the two $\boldsymbol{\nabla}$ operators from diffusive transport (Equation 2.13) combined with the square-gradient terms in the free

energy functional (Equation 2.4). Taking the Fourier transform of both sides, we get,

$$\frac{\partial \widehat{\phi}_i(\boldsymbol{q})}{\partial t} = \widehat{y}\Big(\Big\{\widehat{\phi}_i(\boldsymbol{q})\Big\}\Big), \tag{2.44}$$

where we defined,

$$\widehat{\phi}_i(\boldsymbol{q}) = \int \mathrm{d}\mathbf{r}\, \phi_i(\boldsymbol{r}) \exp\left(-j\boldsymbol{q}\cdot\boldsymbol{r}\right). \tag{2.45}$$

Note that j in this context represents the unit imaginary number. We then split $\widehat{y}$ into its linear and nonlinear parts, L and N:

$$\frac{\partial \widehat{\phi}_i(\boldsymbol{q})}{\partial t} = L\Big(\Big\{\widehat{\phi}_i(\boldsymbol{q})\Big\}\Big) + N\Big(\Big\{\widehat{\phi}_i(\boldsymbol{q})\Big\}\Big). \tag{2.46}$$

and discretize it in time according to,

$$\frac{\widehat{\phi}_i^{(n+1)} - \widehat{\phi}_i^{(n)}}{\Delta t} = L\Big(\Big\{\widehat{\phi}_i^{(n+1)}(\boldsymbol{q})\Big\}\Big) + N\Big(\Big\{\widehat{\phi}_i^{(n)}(\boldsymbol{q})\Big\}\Big), \tag{2.47}$$

taking the linear terms implicitly and the nonlinear terms explicitly. We explored the use of other time-stepping schemes and included our findings in Section B.7.

Chapter 3

Mechanisms of Asymmetric Membrane Formation

3.1 Background

Polymer membranes are essential to water security: they purify our drinking water, desalinate sea water into potable water, and treat wastewater before its release to the environment[46, 47]. The separation performance of these membranes is largely determined by their microstructure. An asymmetric microstructure is advantageous for many applications[6]: the smaller pores on the feed-side of the membrane enable separation, while larger pores deeper into the membrane provide mechanical support with minimal resistance to permeate flow. Nonsolvent-induced phase separation (NIPS)[12, 13]—also known as "wet-phase inversion" or the "Loeb-Sourirajan process"[7]—is a typical way to make asymmetric membranes. In NIPS, a homogeneous polymer solution is cast into a film and then immersed in a nonsolvent bath. The exchange of nonsolvent and solvent between the bath and the film enriches the film in nonsolvent, inducing phase separation of the film to a polymer-rich phase that becomes the membrane matrix and a polymer-poor

phase that becomes the membrane pores.

Selecting process parameters to target specific membrane microstructures is challenging due to our limited understanding of NIPS; membrane manufacturers rely on heuristics, but this approach limits the development of more effective membranes. To understand NIPS, several research groups have modeled the NIPS system with Flory-Huggins thermodynamics coupled to multicomponent transport equations. Numerical techniques used to simulate NIPS include lattice Boltzmann, [30] smoothed particle hydrodynamics, [31] and phase-field simulations [32, 33, 48, 34]. While these studies have shown mass-transfer-induced phase separation, they predicted either the unrealistic formation of alternating polymer-rich and polymer-poor layers aligned with the film-bath interface, or the formation of microstructures with homogeneous pore size distributions. To our knowledge, no existing numerical study of NIPS has shown the formation of graded asymmetric pore size distributions, suggesting that physics essential to NIPS membrane formation is missing in the existing models. In their numerical study of membrane formation by thermally-induced phase separation (TIPS), Millett and co-workers[49] demonstrated the formation of graded asymmetric microstructures by anisotropic cooling of a homogeneous film into a phase-separated membrane. Based on their TIPS model and the NIPS studies mentioned above, we hypothesize that in addition to mass-transfer-induced phase separation, two more mechanisms are essential to the formation of asymmetric microstructures: thermal fluctuations and structural arrest due to solidification of the polymer-rich phase. Solidification mechanisms[50] in NIPS include crystallization, gelation, and vitrification; we select glassy dynamics for the solidification mechanism in this study.

3.2 Phase-field model

We have modified our phase-field model from previous NIPS studies[33, 48, 34] to incorporate thermal fluctuations and a glass transition. Details of these modifications are included in Chapter 2. To focus on these two features, we exclude hydrodynamics in this chapter and use a system of diffusion equations to model NIPS. Phase separation with hydrodynamics is discussed further in Chapter 5. Using R_0, the root-mean-square (RMS) end-to-end distance of a reference polymer with degree of polymerization N_r as the characteristic length scale, τ, the Rouse time of the reference polymer in a solvent of viscosity, η_s, as the characteristic time scale, and $N_r k_B T/b^3$ as the characteristic chemical potential scale, we present our model in dimensionless form:

$$\frac{\partial \phi_i(\boldsymbol{r},t)}{\partial t} = \boldsymbol{\nabla}\cdot\left[\sum_j^{p,n} M_{ij}(\{\phi_i\})\boldsymbol{\nabla}\mu_j(\{\phi_i\})\right] + \alpha N_r^{-1/4}\theta_i(\boldsymbol{r},t) \tag{3.1}$$

where $\phi_p(\boldsymbol{r},t)$ and $\phi_n(\boldsymbol{r},t)$ are the polymer and nonsolvent volume fractions, M_{ij} is the mobility matrix, μ_j is the chemical potential of species j, and $\theta_i(\boldsymbol{r},t)$ are noise terms that follow fluctuation-dissipation theorem (FDT) statistics[41],

$$\langle \theta_i(\boldsymbol{r},t)\rangle = 0 \tag{3.2a}$$

$$\langle \theta_i(\boldsymbol{r},t)\theta_j(\boldsymbol{r'},t')\rangle = -2\boldsymbol{\nabla}\cdot[M_{ij}(\{\phi_i\})\boldsymbol{\nabla}\delta(\boldsymbol{r}-\boldsymbol{r'})]\delta(t-t'). \tag{3.2b}$$

The incompressibility assumption implicitly gives the solvent volume fraction, $\phi_s = 1 - \phi_p - \phi_n$. The noise-scaling factor, $\alpha \in [0,1]$, reduces the strength of the fluctuations in Eq 3.1 for numerical stability, where $\alpha = 0$ makes the dynamics purely deterministic while $\alpha = 1$ sets noise strengths consistent with FDT. For all stochastic simulations in this work, we set $\alpha = 0.04$; although this value breaks consistency with FDT, we show that $\alpha = 0.04$ is large enough to eliminate nonphysical membrane features observed in

purely deterministic simulations. A glass transition is introduced in the model through the use of concentration-dependent mobilities,

$$M_{pp} = \phi_p(1-\phi_p)/\eta \tag{3.3a}$$

$$M_{pn} = M_{np} = -\phi_p\phi_n/\eta \tag{3.3b}$$

$$M_{nn} = \phi_n(1-\phi_n)/\eta, \tag{3.3c}$$

where η is the concentration-dependent local viscosity. We confer glassy dynamics by modeling η as a sigmoidal function of the local polymer volume fraction, $\phi_p(\boldsymbol{r})$:

$$\eta = 1 + \frac{\eta_p/\eta_s - 1}{1 + \exp\left(-\frac{1}{w}\left(\phi_p(\boldsymbol{r}) - \phi_p^*\right)\right)} \tag{3.4}$$

where η_p/η_s represents the pure-component viscosity ratio of the polymer and the solvent (implicitly assuming $\eta_n = \eta_s$), w controls the width of the sigmoid, and ϕ_p^* represents the glass-transition concentration. A sigmoid mimics the Vogel-Fulcher-Tamman-Hesse (VFTH) and Williams-Landel-Ferry (WLF) equations[42] with the exponential growth of viscosity, while bounding its maximum value for computational stability. Setting $w = 5 \times 10^{-3}$ approximates η as a step function, narrow enough such that $\eta = 1$ at $\phi_p = 0$, but wide enough to avoid computational issues associated with a mathematical discontinuity. This choice implies that for ϕ_p values far enough from ϕ_p^*, $\eta = 1$ for $\phi_p(\boldsymbol{r}) < \phi_p^*$, while $\eta = \eta_p/\eta_s$ for $\phi_p(\boldsymbol{r}) > \phi_p^*$. Thus, local mobilities are unscaled in non-glassy regions but they are scaled by η_p/η_s in glassy regions. Setting $\eta_p/\eta_s = 1$ disables the glass transition while $\eta_p/\eta_s = 1 \times 10^4$ enables it. The latter value serves as a balance between faithfully representing a physical glass transition and accessing practical simulation times; we further justify this choice in Chapter 5 and in Section B.4.

Finally, the chemical potential terms in Eq. 2.23 are calculated as the functional

derivatives of the system free energy, $\mu_i = \delta F/\delta\phi_i$, where Flory-Huggins-de Gennes thermodynamics describe the free energy:

$$F\left[\{\phi_i\}\right] = \int \mathrm{d}\mathbf{r}\left[f(\{\phi_i\}) + g(\{\phi_i\})\right] \tag{3.5a}$$

$$f(\{\phi_i\}) = \sum_i^{p,n,s} \frac{\phi_i}{N_i}\ln\phi_i + \frac{1}{2}\sum_{i\neq j}^{p,n,s}\chi_{ij}\phi_i\phi_j \tag{3.5b}$$

$$g(\{\phi_i\}) = \frac{1}{2}\begin{bmatrix}\boldsymbol{\nabla}\phi_p & \boldsymbol{\nabla}\phi_n\end{bmatrix}\begin{bmatrix}\kappa_p+\kappa_s & \kappa_s \\ \kappa_s & \kappa_n+\kappa_s\end{bmatrix}\begin{bmatrix}\boldsymbol{\nabla}\phi_p \\ \boldsymbol{\nabla}\phi_n\end{bmatrix}. \tag{3.5c}$$

Eqs. 3.5b and 3.5c represent the bulk and interfacial free energy contributions, respectively. We set the degree of polymerization of each component as, $N_p = 20, N_n = N_s = 1$, with the reference, $N_r = 20$, the interaction parameters as, $\chi_{pn} = 1.048$, $\chi_{ps} = \chi_{ns} = 0$, and the square-gradient coefficients as, $\kappa_p = \kappa_n = \kappa_s = 1.5$. Details of our model and numerical methods are included in Chapter 2.

3.3 Thermodynamic setup

Figure 3.1 shows the ternary phase diagram for the NIPS system in this work. We set initial film compositions near the critical point based on our findings that such compositions are necessary for mass-transfer-induced phase separation[34]. The nonsolvent bath composition was set to nearly pure nonsolvent, leaving only small amounts of polymer and solvent to avoid the singular composition bounds of the Flory-Huggins functional. We initialized the top-half of the simulation box as the bath and the bottom-half as the homogeneous film. No-flux boundary conditions were implemented at the bottom of the film and at the top of the bath, while periodic boundary conditions were imposed on the lateral sides of the simulation box. To visualize results, only domains corresponding to

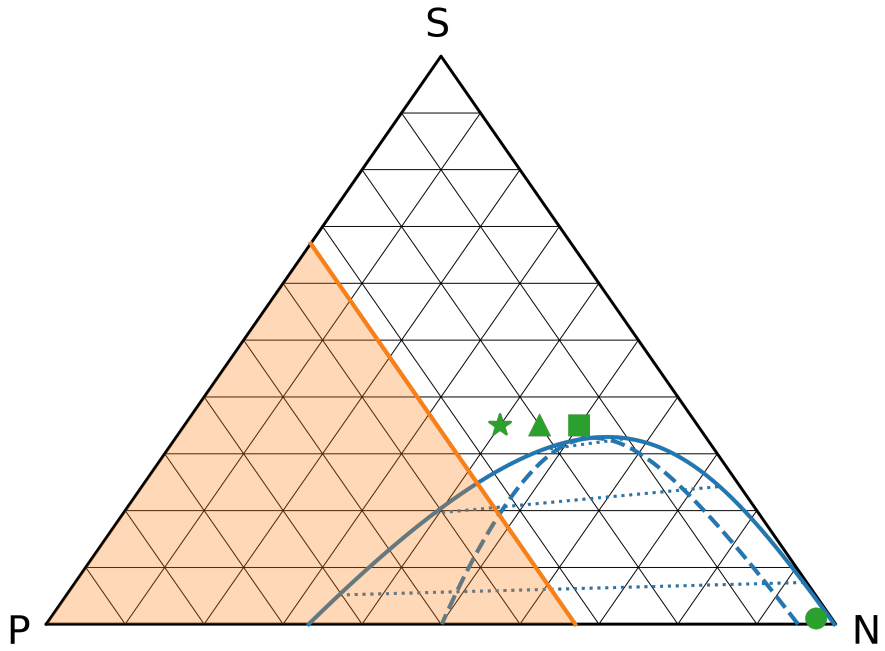

Figure 3.1: Ternary phase diagram for our NIPS system. Each vertex corresponds to pure polymer (P), pure solvent (S), and pure nonsolvent (N) compositions. The solid blue line marks the binodal while the dashed blue line marks the spinodal, as calculated with Flory-Huggins thermodynamics where $\chi_{pn} = 1.048$, $\chi_{ps} = \chi_{ns} = 0$, $N_p = 20$, $N_n = N_s = 1$. The dotted blue lines are examples of tie lines. The solid orange line marks the glass transition concentration, $\phi_p^* = 0.33$. Any composition within the shaded orange area is considered "glassy." The green circle marks the bath composition, which is almost pure nonsolvent ($\phi_p = 0.02, \phi_n = 0.97$). The green star ($\phi_p = 0.25, \phi_n = 0.40$), green triangle ($\phi_p = 0.20, \phi_n = 0.45$), and green square ($\phi_p = 0.15, \phi_n = 0.50$) mark the initial homogeneous film compositions used in this study.

the initial homogeneous film were shown, omitting the nonsolvent bath for clarity. The glass-transition concentration was set to $\phi_p^* = 0.33$, a value close enough to the initial film compositions so that mobility contrast effects manifest soon after phase separation. In reality, ϕ_p^* is not arbitrary as it changes with dope formulation and temperature[51, 52]. We study the effects of varying ϕ_p^* in Chapter 4.

3.4 Role of thermal fluctuations

Figure 3.2 illustrates the effects of thermal fluctuations on mass-transfer-driven microstructure evolution. In the absence of fluctuations (Figure 3.2a), a pattern of alternating polymer-rich and polymer-poor layers forms parallel to the film-bath interface, consistent with other numerical studies of NIPS[31, 34]. We attribute the propagation of the ordered pattern to surface-directed spinodal decomposition (SDSD)[53]. In contrast, enabling fluctuations (Figure 3.2b) introduces disorder to the dynamics, disrupting the propagation of this ordered pattern with more isotropic bulk spinodal decomposition. The two rows of polymer-poor circles at $t = 1 \times 10^3$, manifest the competition between the order imposed by SDSD and the disorder due to thermal fluctuations. Morphologies at later times show that deeper into the film, the influence of SDSD wanes and bulk spinodal decomposition dominates. As shown, setting $\alpha = 0.04$ is enough to break the ordered pattern, but the effects of stronger fluctuations, including phase separation by nucleation, remain unexplored; we leave this complexity to future work.

3.5 Role of the glass transition

Figure 3.3 shows the effects of the glass transition on the 2D microstructure. In the absence of a glass transition (Figure 3.3a), the progress of microstructure formation varies with film depth at early times (first three frames). A phase-separation front due to SDSD follows nonsolvent diffusion into the film. Just above the phase-separation front, domain sizes increase towards the film-bath interface; but far enough from the front, domain sizes become more homogeneous, a profile that eventually manifests through the whole film at late times (last two frames). We attribute these observations to domain coarsening. In a bulk quench of a system that coarsens only by diffusion, the characteristic domain size,

L, follows the Lifshitz-Slyozov-Wagner[54, 55] scaling law, $L \sim t^{1/3}$. Assuming that a similar power law applies to mass-transfer-induced phase separation, *i.e.,* the coarsening mechanisms involved do not change the exponent, we posit that for phase-separated domains,

$$L(t, y) \sim (t - t_p(y))^{1/3}, \tag{3.6}$$

where $t_p(y)$ is the time when the phase-separation front arrived at film depth, y. Eq 3.6 offers a crude rationalization for our simulations since phase-separated domains in 2D span several values of y; nevertheless, it proves useful for the discussion. For domains just above the phase-separation front, the quantity $(t - t_p(y))$ increases away from the front, consistent with the observed domain-size profile. However, for domains far enough from the phase-separation front, we can approximate $(t - t_p(y)) \approx t$, implying L is no longer a function of film depth for these mature domains. The same approximation applies to all values of y, long after the phase separation front has reached the bottom of the film, explaining the symmetric pore-size distribution at late times. We discuss the computation of the average domain size for each y-slice in Section B.2.

In contrast, the glass transition dramatically changes the microstructure (Figure 3.3b). To begin, a polymer-rich skin forms at the film-bath interface. Thermal fluctuations introduce perforations on the polymer-rich skin before it turns glassy. Due to the imposed mobility contrast, the glassy skin then acts as a barrier to nonsolvent entry, only allowing the nonsolvent to penetrate the film through the perforations, consistent with the proposed mechanism by Smolders and co-workers[56, 57, 58]. The perforations grow deeper into the film, forming finger-like structures that eventually become a network of pores—a stark contrast from the closed-pore morphology formed without the glass transition. Though similar in appearance, these "finger-like structures" are distinct from macrovoids[14, 59] that span the thickness of a membrane; we make no claims about

macrovoid formation in this work.

In addition to the qualitative change in morphology, the glass transition also leads to a positive pore-size gradient from the film-bath interface to the glass-transition front, evidenced by the positive slope of the film-depth vs. domain-size curve from $y = 0$ to the orange glass-transition line. *The mechanism responsible for this pore-size gradient is the increasing lead of the phase-separation front over the glass-transition front.* Phase separation is induced by the diffusion of enough nonsolvent into the film such that the film concentration enters the spinodal. Vitrification occurs when the polymer-rich concentration crosses the glass-transition concentration. The latter happens deeper into the spinodal, requiring more nonsolvent than the former. For locations close to the film-bath interface, the phase-separation and glass-transition fronts would be on top of each other, as the nonsolvent source is close. Deeper into the film, the time-difference between having enough nonsolvent for phase separation and having enough for vitrification becomes magnified since formed domains of the membrane above act as hindrance to further nonsolvent transport. We plot the propagation dynamics of these two fronts in Figures 3.7 and 3.8. Domain features above the glass-transition front are frozen while those below it are free to evolve. Following the same assumptions made for Eq 3.6, we posit that for domains above the glass-transition front:

$$L(y) \sim (t_g(y) - t_p(y))^{1/3}, \tag{3.7}$$

where $t_g(y)$ and $t_p(y)$ are the times when the glass-transition and phase-separation fronts arrived at film depth, y, respectively. Again, Eq 3.7 offers a crude rationalization for our simulations, but it proves useful for the discussion. Since the phase-separation front moves faster than the glass-transition front, the quantity $(t_g(y) - t_p(y))$ increases with film depth, leading to the asymmetric pore-size distribution. This proposed mechanism

is not unfounded; using in-situ experiments, McHugh and co-workers[60] correlated the transition from a macrovoid morphology to a sponge microstructure with changes to the propagation dynamics of these two fronts, demonstrating their importance to shaping membrane morphology.

While Figure 3.3 shows microstructures with a continuous polymer-rich phase, Figure 3.4 demonstrates that less polymer content in the initial film can lead to an inversion of the continuous phase to polymer-poor. In the absence of a glass transition (Figure 3.3a vs. Figure 3.4a), the inversion itself does not change the propagation kinetics of the phase-separation front; the front in Figure 3.4a has a slight lead in penetrating the film only because its initial film composition is closer to the binodal, allowing nonsolvent entry to induce phase separation earlier. On the other hand, the inversion alters front-propagation dynamics in the presence of a glass transition (Figure 3.3b vs. Figure 3.4b). Since the polymer-poor phase is continuous in Figure 3.4b, nonsolvent can penetrate the film without having to form finger-like structures, allowing both the phase-separation and glass-transition fronts to propagate more quickly. However, this speed-up unevenly favors the glass-transition front, effectively reducing $(t_g(y) - t_p(y))$ for frozen domains. As a consequence, the domain-size gradient from the film-bath interface to the glass-transition front becomes less pronounced in Figure 3.4b than it was for Figure 3.3b.

The dynamics of membrane formation also change in 3D, owing to the greater tendency of domains to stay continuous after phase separation. Figure 3.5 shows the 3D equivalent of Figure 3.3b. The finger-like structures in 2D translate to a 3D pore network that allows the nonsolvent to penetrate the film faster in 3D. The bicontinuous microstructure in 3D leads to speed-ups for both the phase-separation and glass-transition fronts. Again, the speed-up unevenly favors the latter—especially for deeper points in the film—leading to a less-pronounced gradient in domain size for the 3D microstructure.

Similar effects of bicontinuity are shown in Figure 3.6, the 3D equivalent of Fig-

ure 3.4b. The discrete polymer-rich phase in the 2D morphology translates to a mostly continuous structure in 3D. Despite the continuous polymer-rich phase, the higher dimensionality still leads to speed-ups for both the phase-separation and glass-transition fronts. The domain-size gradient in 3D is again less-pronounced due to the larger speed-up of the glass-transition front.

Despite the bicontinuity of both 3D morphologies (Figure 3.5 vs. Figure 3.6), initial film composition remains important to the propagation of the phase-separation and glass-transition fronts. Less polymer content in the initial film leads to less resistance to mass-transfer, evidenced by faster propagation of both fronts in Figure 3.6. However, the faster advance of both fronts also leads to less pronounced domain-size asymmetry, as demonstrated by the decreased slope in the film-depth vs. domain-size curve in Figure 3.6.

While the asymmetric structures observed here in both 2D and 3D are in qualitative agreement with experiments[15, 27], we do not attempt quantitative comparisons. Instead, our focus was on gaining a mechanistic understanding of NIPS by building a model step-by-step, adding complexity in each step and considering its role in membrane formation. We demonstrated that mass-transfer-induced phase separation, thermal fluctuations, and a structural arrest mechanism are necessary and sufficient to form graded asymmetric pore-size distributions. However, other complexities in experiments remain unexplored, notably hydrodynamics. As velocities are scaled by the inverse of mixture viscosity, we assume that flows in any continuous polymer-rich phase are negligible, due to the high viscosity ratio in our glassy dynamics model. Evidence for this assumption is provided in Chapter 5. Of course, hydrodynamics can prove to be more significant in NIPS operating regimes where the continuous polymer-rich phase is not subject to early vitrification; such complexities, including the physical mechanisms behind the formation of macrovoids[14, 59] and other membrane morphologies[61, 62], are left to future study.

3.6 Propagation dynamics of the phase-separation and glass-transition fronts

Figures 3.7 and 3.8 illustrate the advance of the phase-separation and glass-transition fronts for the NIPS simulations in this chapter. The location of the phase-separation front was determined as the deepest point in the film where the difference between the maximum and minimum polymer concentrations crosses a heuristic threshold. In this analysis, we set this threshold at $\phi_p^{max} - \phi_p^{min} = 0.1$. The glass-transition front was recorded as the deepest point in the film where at least one pixel (or voxel) has crossed the glass transition concentration, ϕ_p^*. In all figures included, the lead of the phase-separation front on the glass-transition front increases with time, allowing for the formation of the graded asymmetric pore size distributions. In 2D, the phase-separation and glass-transition fronts travel slower for the dope composition that leads to a polymer-rich matrix, evident in comparing Figure 3.7a and Figure 3.7b. Due to the greater tendency of forming bicontinuous structures, the composition dependence of the front speeds is reduced in 3D as shown by comparing Figure 3.8a and Figure 3.8b. Overall, both fronts travel faster in 3D than in 2D.

3.7 Conclusions

In this chapter, we showed that in addition to mass-transfer-driven phase separation, both thermal fluctuations and structural arrest are necessary and sufficient for the formation of asymmetric microstructures in NIPS. Specifically, the degree of asymmetry is determined by the increasing lead of the phase-separation front over the glass-transition front. In the next chapter, we explore the effects of changing the NIPS formulation to the mechanisms of membrane formation and the resulting membrane morphologies.

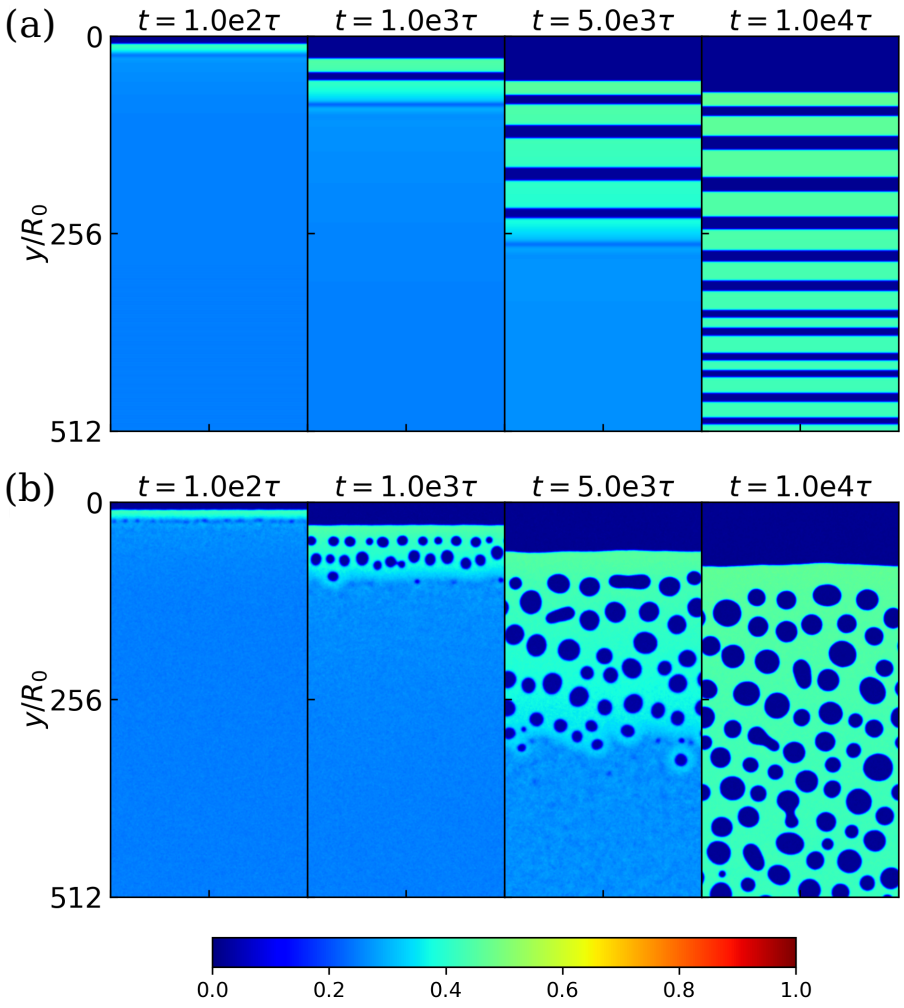

Figure 3.2: NIPS simulations (a) without ($\alpha = 0$) and (b) with ($\alpha = 0.04$) thermal fluctuations. Each box shown is $256R_0 \times 512R_0$. The y-coordinate corresponds to film depth, where $y = 0$ is the film-bath interface and $y = 512$ is the bottom of the film. The bath is not visualized for clarity. Polymer-rich regions are light green and polymer-poor regions are dark blue, color bar included for ϕ_p. Initial film composition is ($\phi_p = 0.25, \phi_n = 0.40$), corresponding to the green star in Figure 3.1. No glass transition effects are introduced, *i.e.*, $\eta_p/\eta_s = 1$ for both (a) and (b).

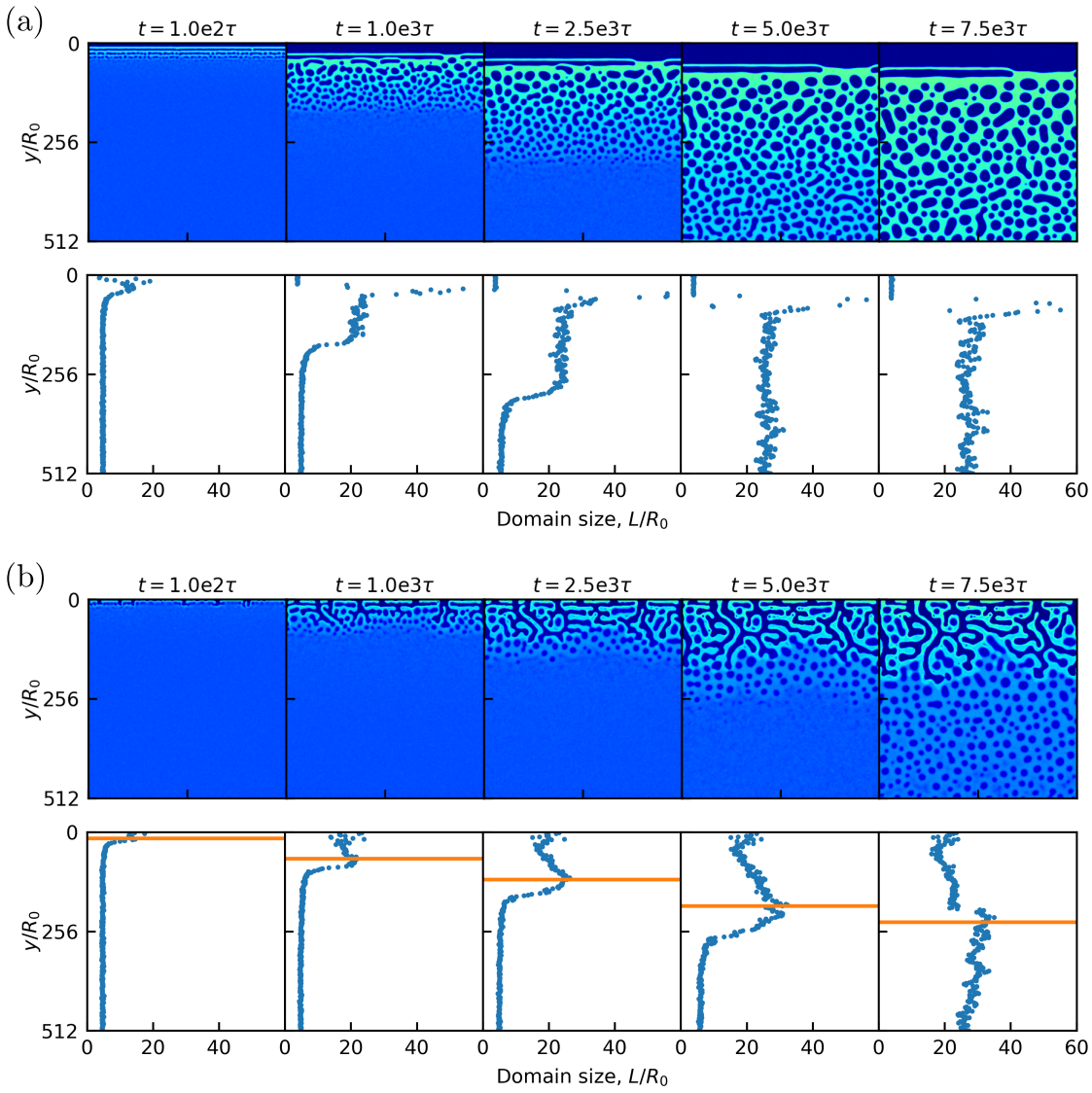

Figure 3.3: NIPS simulations in 2D and their domain size profiles (a) without and (b) with glass transition effects for the initial film composition of $(\phi_p = 0.20, \phi_n = 0.45)$, corresponding to the green triangle in Figure 3.1. Mobility contrasts set at (a) $\eta_p/\eta_s = 1$, (b) $\eta_p/\eta_s = 10^4$. Each density plot shown is $512R_0 \times 512R_0$. The y-coordinate corresponds to film depth, where $y = 0$ is the film-bath interface and $y = 512$ is the bottom of the film. The bath is not visualized for clarity. Polymer-rich regions are light green and polymer-poor regions are dark blue, ϕ_p color bar included in Figure 3.2. The orange line (glass-transition front) in the domain size profile for (b) corresponds to the deepest point in the film where at least one grid point has crossed the glass transition concentration, ϕ_p^*.

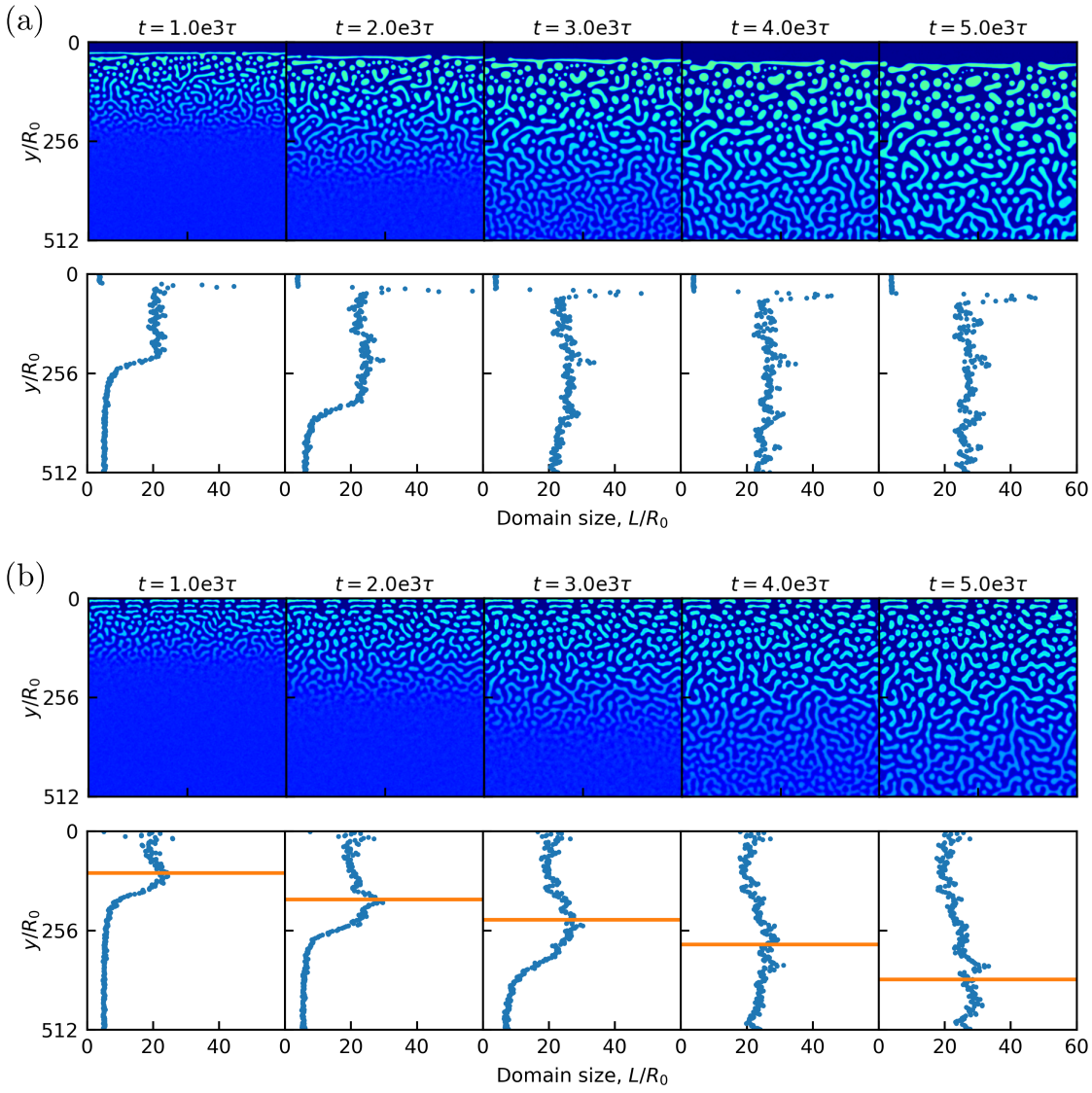

Figure 3.4: NIPS simulations in 2D and their domain size profiles (a) without and (b) with glass transition effects for the initial film composition of ($\phi_p = 0.15, \phi_n = 0.50$), corresponding to the green square in Figure 3.1. Mobility contrasts set at (a) $\eta_p/\eta_s = 1$, (b) $\eta_p/\eta_s = 10^4$. Each density plot shown is $512R_0 \times 512R_0$. The y-coordinate corresponds to film depth, where $y = 0$ is the film-bath interface and $y = 512$ is the bottom of the film. The bath is not visualized for clarity. Polymer-rich regions are light green and polymer-poor regions are dark blue, ϕ_p color bar included in Figure 3.2. The orange line (glass-transition front) in the domain size profile for (b) corresponds to the deepest point in the film where at least one grid point has crossed the glass transition concentration, ϕ_p^*.

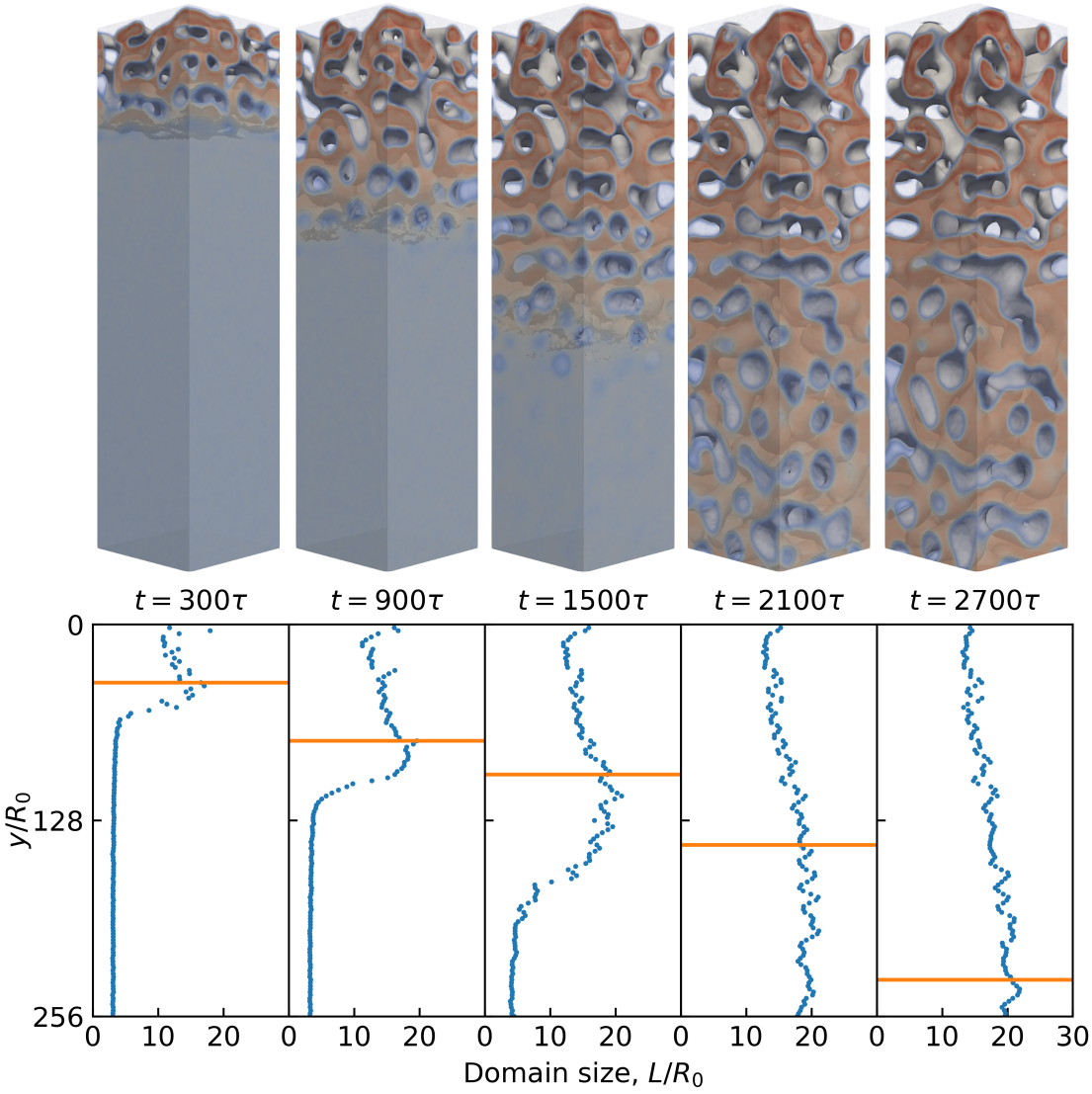

Figure 3.5: NIPS simulation in 3D and its domain size profile for the initial film composition of $(\phi_p = 0.20, \phi_n = 0.45)$, corresponding to the green triangle in Figure 3.1. Mobility contrast set at $\eta_p/\eta_s = 10^4$. Each density plot shown is $64R_0 \times 256R_0 \times 64R_0$. The y-coordinate corresponds to film depth, where $y = 0$ is the film-bath interface and $y = 256$ is the bottom of the film. The bath is not visualized for clarity. Polymer-rich regions are opaque red, polymer-poor regions are translucent blue, and the isosurface is opaque beige. The orange line (glass-transition front) in the domain size profile corresponds to the deepest point in the film where at least one grid point has crossed the glass transition concentration, ϕ_p^*.

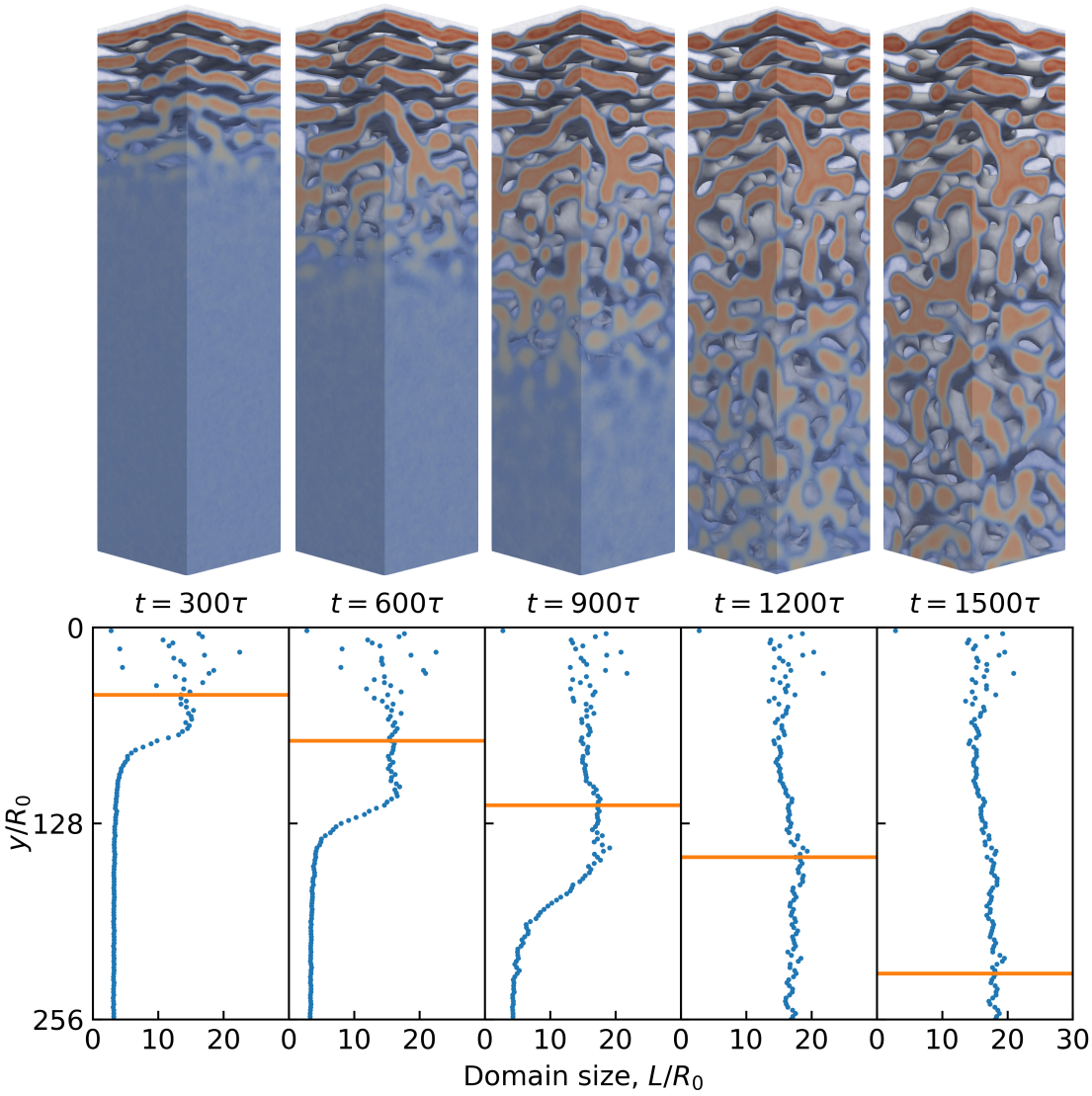

Figure 3.6: NIPS simulation in 3D and its domain size profile for the initial film composition of $(\phi_p = 0.15, \phi_n = 0.50)$, corresponding to the green square in Figure 3.1. Mobility contrast set at $\eta_p/\eta_s = 10^4$. Each density plot shown is $64R_0 \times 256R_0 \times 64R_0$. The y-coordinate corresponds to film depth, where $y = 0$ is the film-bath interface and $y = 256$ is the bottom of the film. The bath is not visualized for clarity. Polymer-rich regions are opaque red, polymer-poor regions are translucent blue, and the isosurface is opaque beige. The orange line (glass-transition front) in the domain size profile corresponds to the deepest point in the film where at least one grid point has crossed the glass transition concentration, ϕ_p^*.

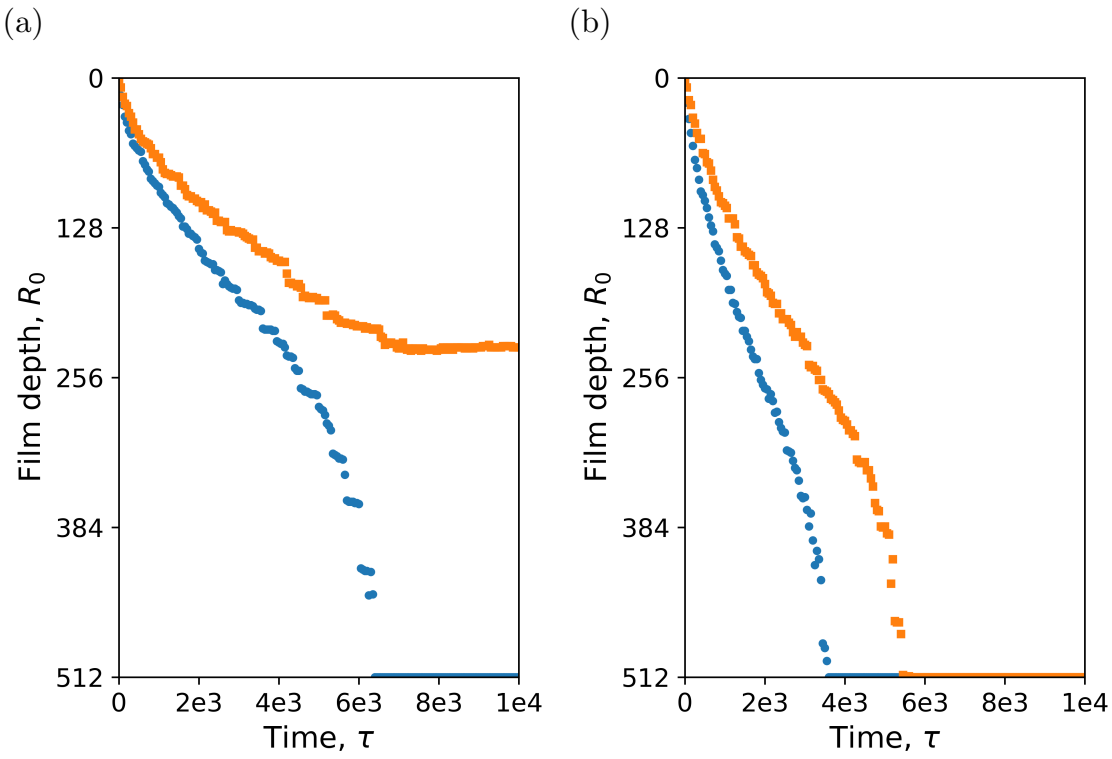

Figure 3.7: Propagation dynamics of the phase-separation (blue circles) and glass–transition (orange squares) fronts into the film for the 2D NIPS simulations shown in (a) Figure 3.3b and (b) Figure 3.4b.

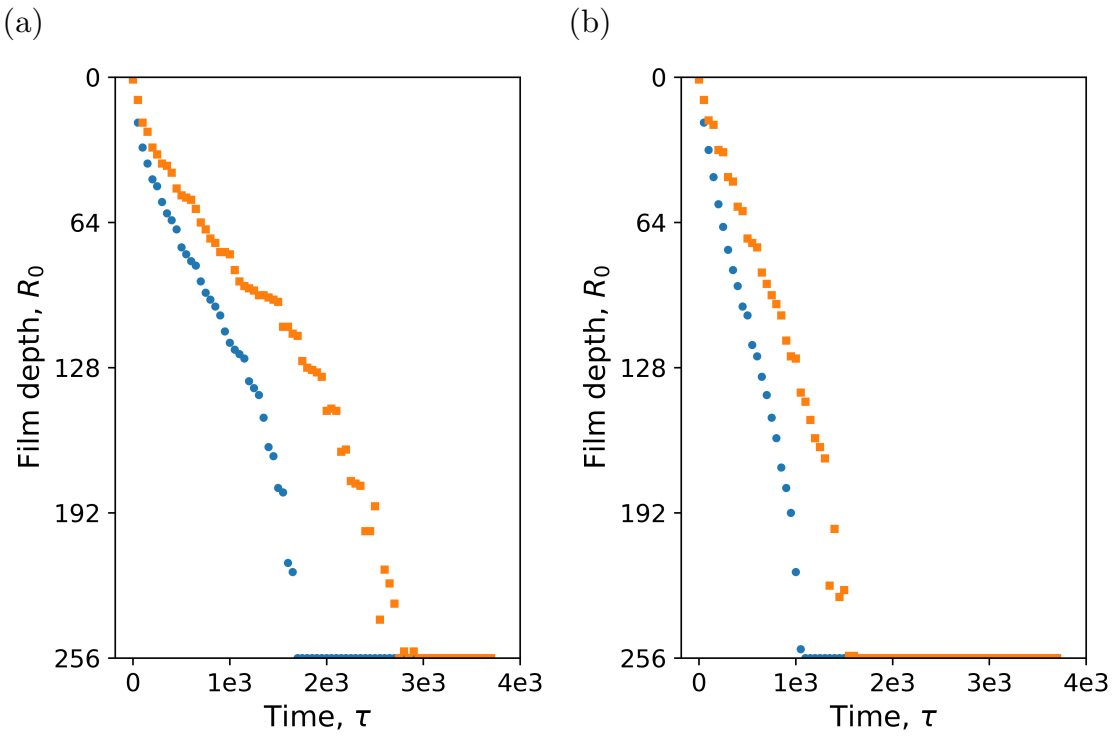

Figure 3.8: Propagation dynamics of the phase-separation (blue circles) and glass–transition (orange squares) fronts into the film for the 3D NIPS simulations shown in (a) Figure 3.5 and (b) Figure 3.6.

Chapter 4

The Role of Formulation in NIPS

4.1 Background

The relationship between NIPS formulation and membrane morphology is of the utmost importance to membrane manufacturers as understanding this relationship enables them to quickly respond to the demands of an ever-changing market. Moreover, such understanding would facilitate targeted design of membranes for optimal separations. Thus, we extend our study of membrane formation mechanisms in Chapter 3 to different NIPS formulations in this chapter. We will examine how changing the glass-transition concentration, ϕ_p^*, and the dope (initial film) composition affect the competition between the phase-separation and glass-transition fronts, and their consequences to the membrane morphology.

4.2 Phase-field model

Since this chapter focuses on the effects of formulation on the membrane formation mechanisms discussed in Chapther 3, we use the same phase-field model described in

Section 3.2. The same thermodynamic setup is also used for this chapter, *i.e.,* the spinodal and binodal remain the same as before. In Section 4.3, we vary the glass-transition concentration, ϕ_p^*, while we change the dope composition in Section 4.4.

4.3 Moving the glass-transition concentration, ϕ_p^*

Figure 4.1 shows the locations of the dope and the glass-transition concentrations, ϕ_p^*, explored in this section. We consider different ϕ_p^* values (0.25, 0.30, 0.33, 0.40, and 0.50) in two sets: first with the dope composition A_0 (ϕ_p=0.20, ϕ_n=0.45) and then with B_0 (ϕ_p=0.15, ϕ_n=0.50). These were the same dope compositions explored in Chapter 3.

In Chapter 3, we explained how the competition between the phase-separation and glass-transition fronts determines the pore-size distribution of the membrane. Figure 4.2 plots the phase-separation and glass-transition fronts for dope composition A_0 ($\phi_p = 0.20$, $\phi_n = 0.45$) with different values of the glass transition concentration, ϕ_p^*= 0.30, 0.33, 0.40, and 0.50. Meanwhile, Figure 4.3 shows the corresponding morpholgies and pore-size distributions at the timepoint when the phase-separation front has reached the bottom of the film. Since our simulation boxes are not large enough to represent the length of a real membrane, we restrict microstructural analysis to this timepoint to avoid finite-size effects. In the limiting case where the dope and the glass-transition compositions are so close to each other (blue circles), the glass-transition front follows the phase-separation front with little delay. The gap between them slowly widens farther down the film. Eventually, the phase-separation front leaves the glass-transition front behind due to the hindered growth of the finger-like structures (Figure 4.3a). These dynamics result in some limited degree of asymmetry. Moving the glass-transition concentration farther from the dope composition (orange triangles) gives the phase-separation front a larger initial lead which results in a higher degree of asymmetry (Figure 4.3b). However, increasing the

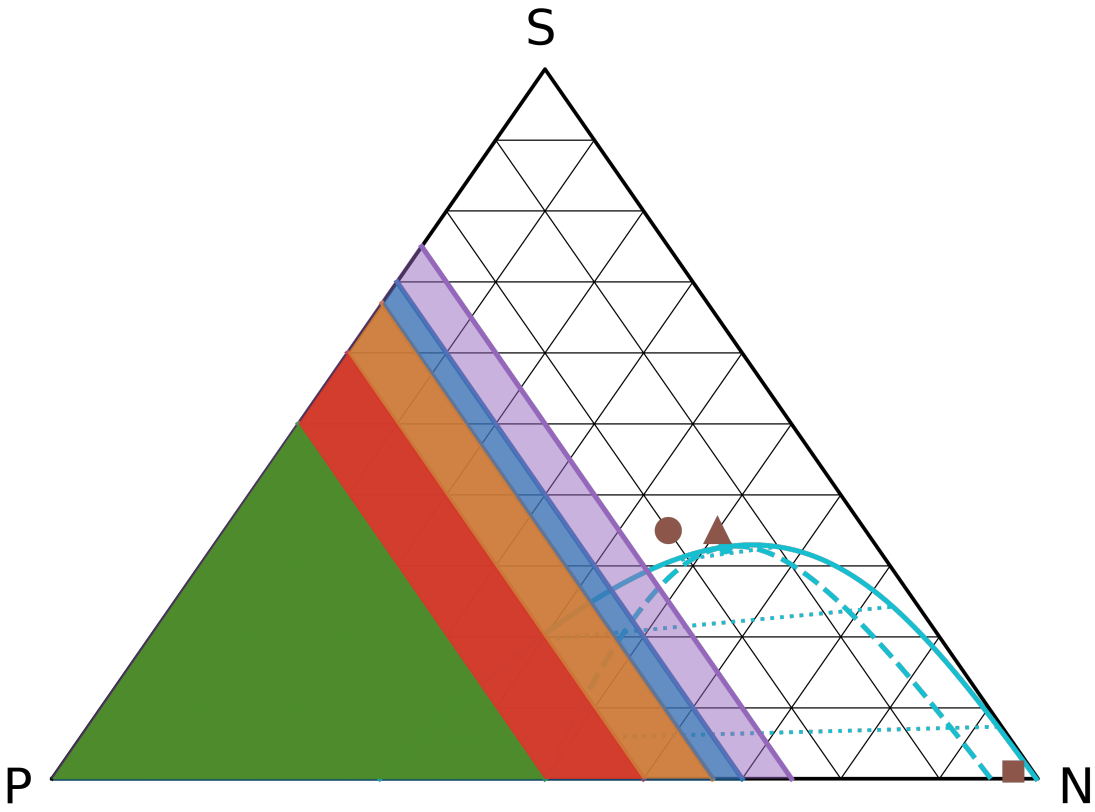

Figure 4.1: Ternary phase diagram for Section 4.3. The solid cyan line marks the binodal while the dashed blue line marks the spinodal, as calculated with Flory-Huggins thermodynamics where $\chi_{pn} = 1.048$,$\chi_{ps} = \chi_{ns} = 0$, $N_p = 20$, $N_n = N_s = 1$. The brown circle marks dope composition A_0 ($\phi_p = 0.20$, $\phi_n = 0.45$) and the brown triangle marks dope composition B_0 ($\phi_p = 0.15$, $\phi_n = 0.50$). The brown square marks the nonsolvent bath ($\phi_p = 0.02$, $\phi_n = 0.97$). The dotted cyan lines are examples of tie lines. The overlapping colored triangles represent the glassy areas for different simulations, where the right edge of a colored triangle marks the glass-transition concentration: $\phi_p^* = 0.25$ (purple), 0.30 (blue), 0.33 (orange), 0.40 (red), and 0.50 (green).

lead further (red squares) begins to reduce the degree of asymmetry (Figure 4.3c). In fact, in the limiting case where the dope and the glass-transition compositions are too far apart (green diamonds), the phase-separation front reaches the bottom of the film before any part of the film crosses the glass transition. This prolonged delay in arresting the coarsening of the phase-separated domains leads to an inverted asymmetric pore-size distribution (Figure 4.3d), as domains near the film–bath interface had more time to coarsen than those towards the bottom of the film.

Figure 4.4 shows the phase-separation and glass-transition fronts for dope composition B_0 ($\phi_p = 0.15$, $\phi_n = 0.50$) with different values of the glass transition concentration, ϕ_p^*= 0.25, 0.30, 0.33, 0.40, and 0.50. Meanwhile, Figure 4.5 shows corresponding morpholgies and pore-size distributions at the timepoint when the phase-separation front has reached the bottom of the film. Compared to the dynamics shown in Figure 4.4, both the phase-separation and glass-transition fronts propagate faster. We attributte this speedup to the qualitative change from a continuous polymer-rich structure (Figure 4.3) to a continuous polymer-poor morphology (Figure 4.5). Inspite of the morphology change, the same trend between the degree of asmmetry and the distance between the dope and glass-transition compositions still applies. In the limiting case where the dope and the glass-transition compositions are so close to each other (purple pluses), the dynamics of the glass-transition and phase-separation fronts are almost identical. Since there is no gap between the two fronts, a homogeneous pore-size distibution results above the glass-transition front (Figure 4.5a). Moving the glass-transition concentration farther from the dope composition (blue circles and orange triangles) widens the gap between the two fronts, especially towards the bottom of the film, which results in an asymmetric pore-size distribution (Figure 4.5b). As before, increasing the lead of the phase separation front further (red squares) begins to reduce the degree of asymmetry observed (Figure 4.5c). In fact, in the limiting case where the dope and the glass-transition compositions are too

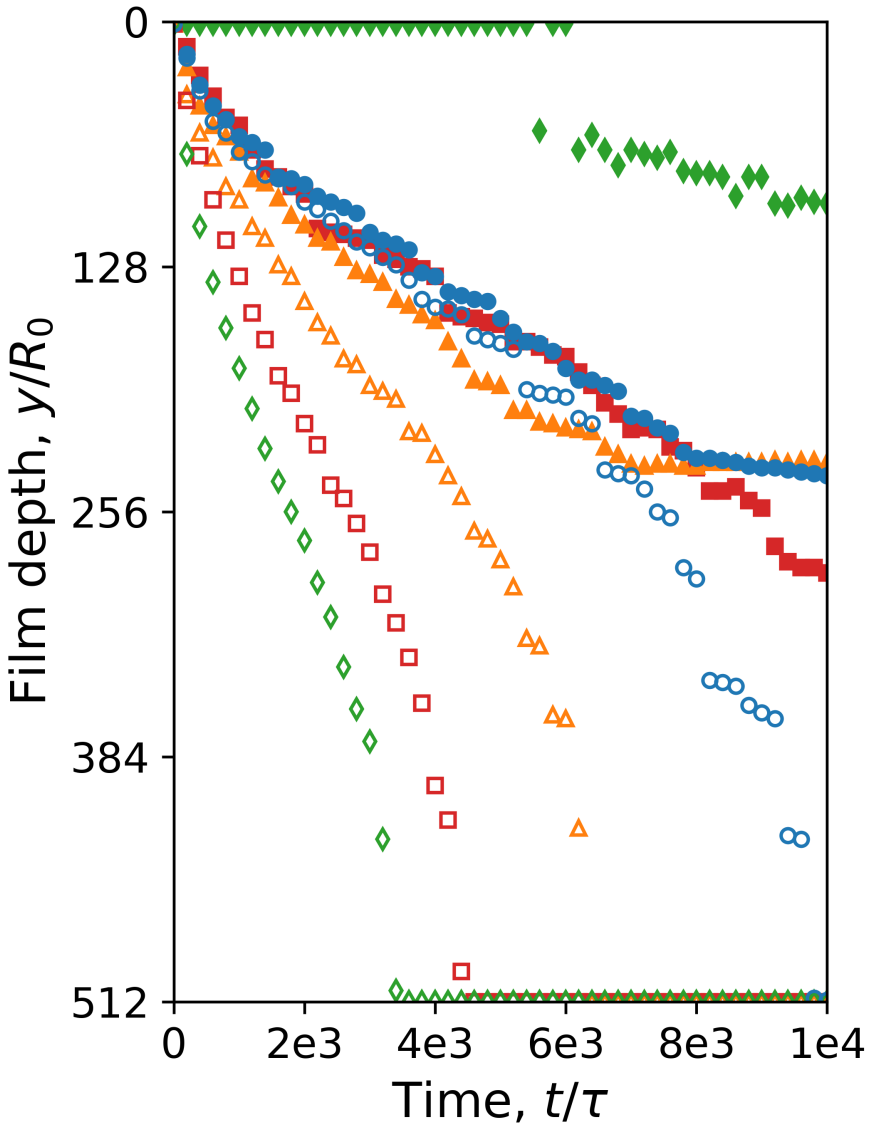

Figure 4.2: Propagation dynamics of the phase-separation (unfilled markers) and glass-transition (filled markers) fronts for dope composition A_0 (ϕ_p=0.20, ϕ_n=0.45), where the glass-transition concentrations are: $\phi_p^* = 0.30$ (blue circles), 0.33 (orange triangles), 0.40 (red squares), and 0.50 (green diamonds).

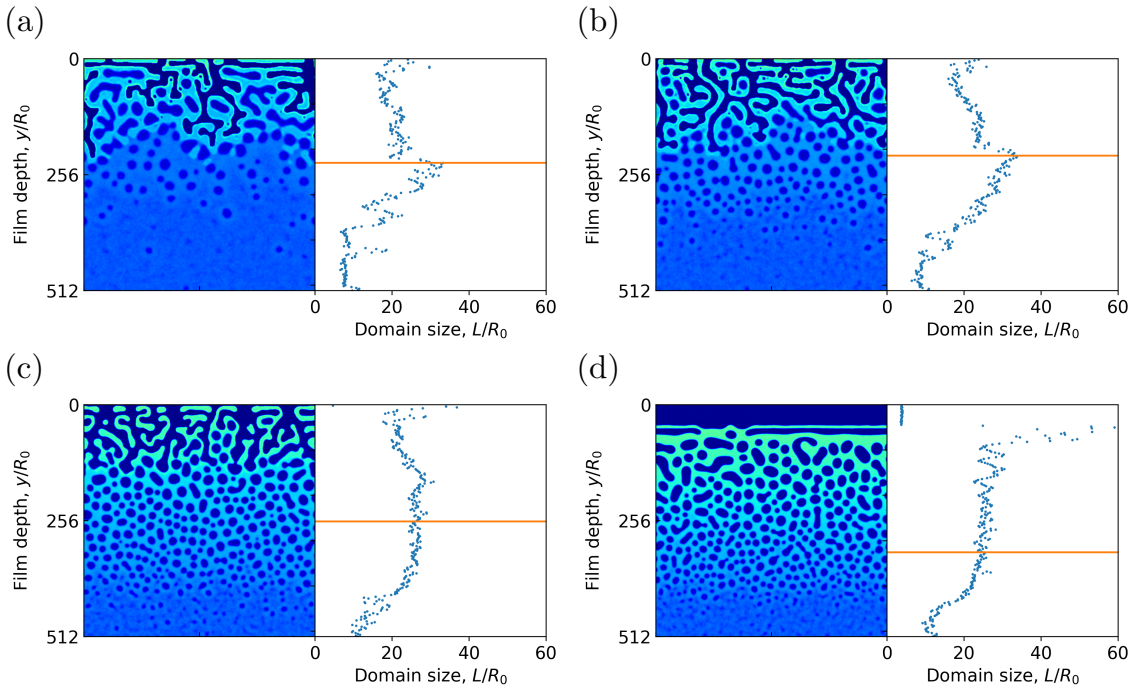

Figure 4.3: Microstructures and domain size profiles for dope composition A_0 (ϕ_p=0.20, ϕ_n=0.45) with glass-transition concentrations, $\phi_p^* =$ (a) 0.30, (b) 0.33, (c) 0.40, and (d) 0.50. Each density plot shown is $512R_0 \times 512R_0$. The y-coordinate corresponds to film depth, where $y = 0$ is the initial film–bath interface and $y = 512$ is the bottom of the film. Polymer-rich regions are light green and polymer-poor regions are dark blue, ϕ_p color bar included in Figure 3.2. The orange line (glass-transition front) in the domain size profile corresponds to the deepest point in the film where at least one grid point has crossed the glass transition concentration, ϕ_p^*. The timepoints shown for each simulation corresponds to the moment the phase-separation front has reached the bottom of the film.

far apart (green diamonds), the phase-separation front reaches the bottom of the film before any part of the film crosses the glass transition. Again, this prolonged delay in structural arrest leads to a more homogeneous pore-size distribution (Figure 4.5d).

4.4 Changing the dope composition

In the previous section, we showed the effects of changing the glass-transition concentration. In practical membrane applications, controlling the glass-transition concentration is not a straightforward endeavor. For example, substituting a more glassy polymer in the dope not only changes ϕ_p^*, but also changes the location of the binodal. On the other hand, the manufacturer has complete control of the dope composition, without changing other aspects of the model. Figure 4.6 shows the locations of the dope compositions we explore in this section. We explore them in two sets. The first is series A, where we sample dope comositions on the $\phi_p = 0.20$ axis: A_0 ($\phi_n = 0.45$), A_1 ($\phi_n = 0.40$), A_2 ($\phi_n = 0.35$), A_3 ($\phi_n = 0.30$), A_4 ($\phi_n = 0.25$). The second is series B, where we sample dope composition on the $\phi_p = 0.15$ axis: B_0 ($\phi_n = 0.50$), B_1 ($\phi_n = 0.45$), B_2 ($\phi_n = 0.40$), B_3 ($\phi_n = 0.35$), B_4 ($\phi_n = 0.30$). The glass-transition concentration for all these simulations are set to $\phi_p^* = 0.33$.

Figure 4.7 plots the phase-separation and glass-transition fronts for series A dope compositions. The propagation of a phase-separation front becomes slower as the dope composition is moved farther from the binodal. In fact, the phase-separation front only reached the bottom of the film for A_0 and A_1, the two dope compositions closest to the binodal. Other than delaying phase separation, the gap between the phase-separation and glass-transition fronts also shrink for dope compositions far from the binodal. In the limiting cases (A_3 and A_4), the phase-separation and glass-transition fronts are almost indistinguishable. Thus, we expect the degree of asymmetry to diminish as dope

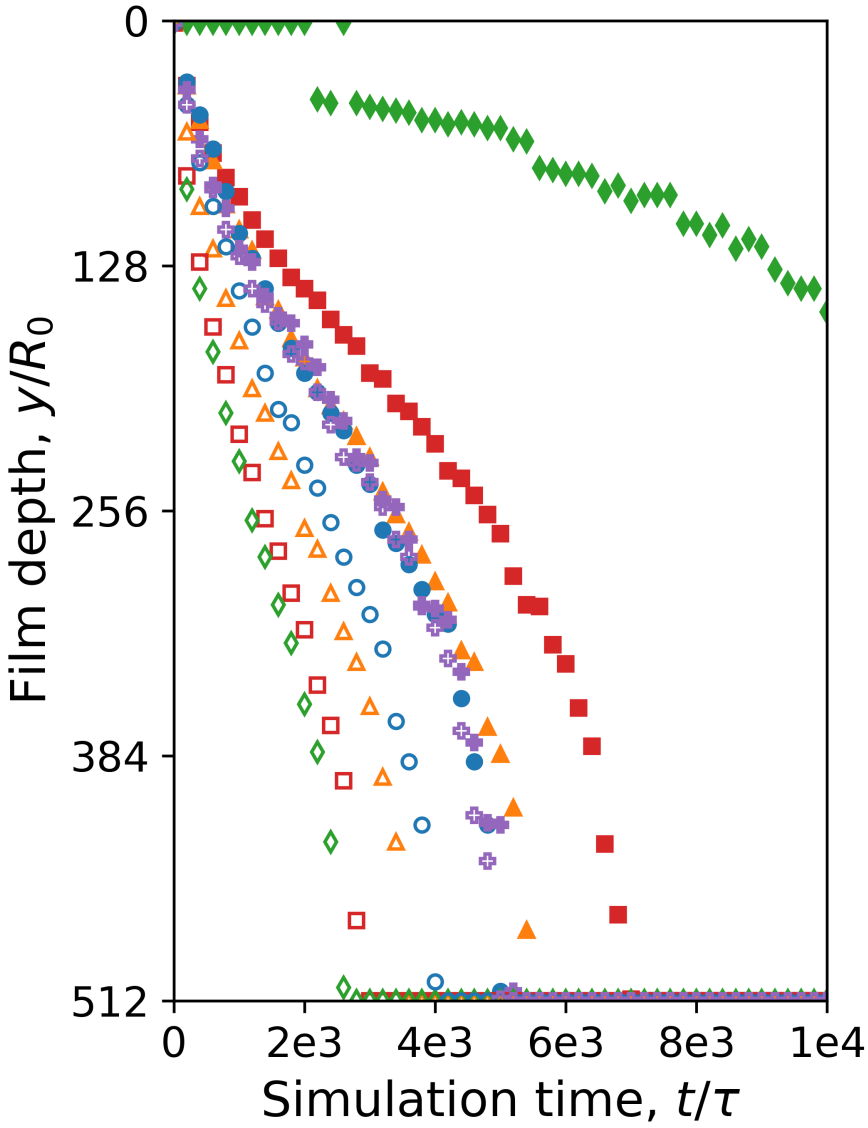

Figure 4.4: Propagation dynamics of the phase-separation (unfilled markers) and glass-transition (filled markers) fronts for the dope composition B_0 (ϕ_p=0.15, ϕ_n=0.50), where the glass-transition concentrations are: $\phi_p^* = 0.25$ (purple pluses), 0.30 (blue circles), 0.33 (orange triangles), 0.40 (red squares), and 0.50 (green diamonds).

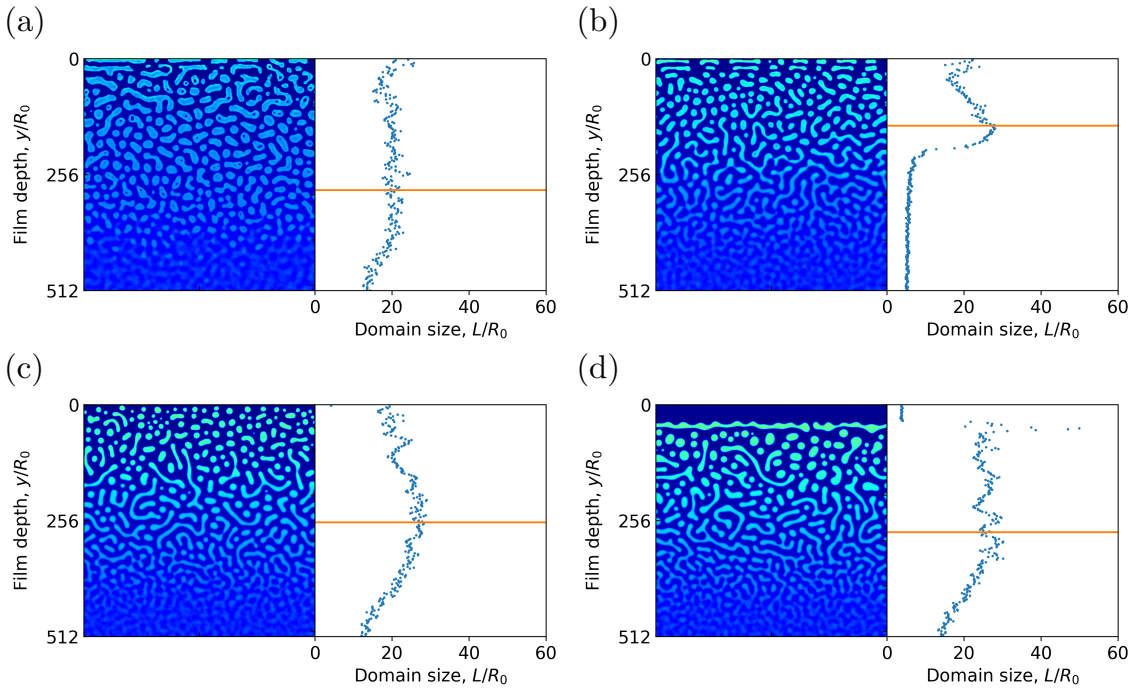

Figure 4.5: Microstructures and domain size profiles for dope composition B_0 (ϕ_p=0.15, ϕ_n=0.50) with glass-transition concentrations, $\phi_p^* =$ (a) 0.25, (b) 0.33, (c) 0.40, and (d) 0.50. Each density plot shown is $512R_0 \times 512R_0$. The y-coordinate corresponds to film depth, where $y = 0$ is the initial film–bath interface and $y = 512$ is the bottom of the film. Polymer-rich regions are light green and polymer-poor regions are dark blue, ϕ_p color bar included in Figure 3.2. The orange line (glass-transition front) in the domain size profile corresponds to the deepest point in the film where at least one grid point has crossed the glass transition concentration, ϕ_p^*. The timepoints shown for each simulation corresponds to the moment the phase-separation front has reached the bottom of the film.

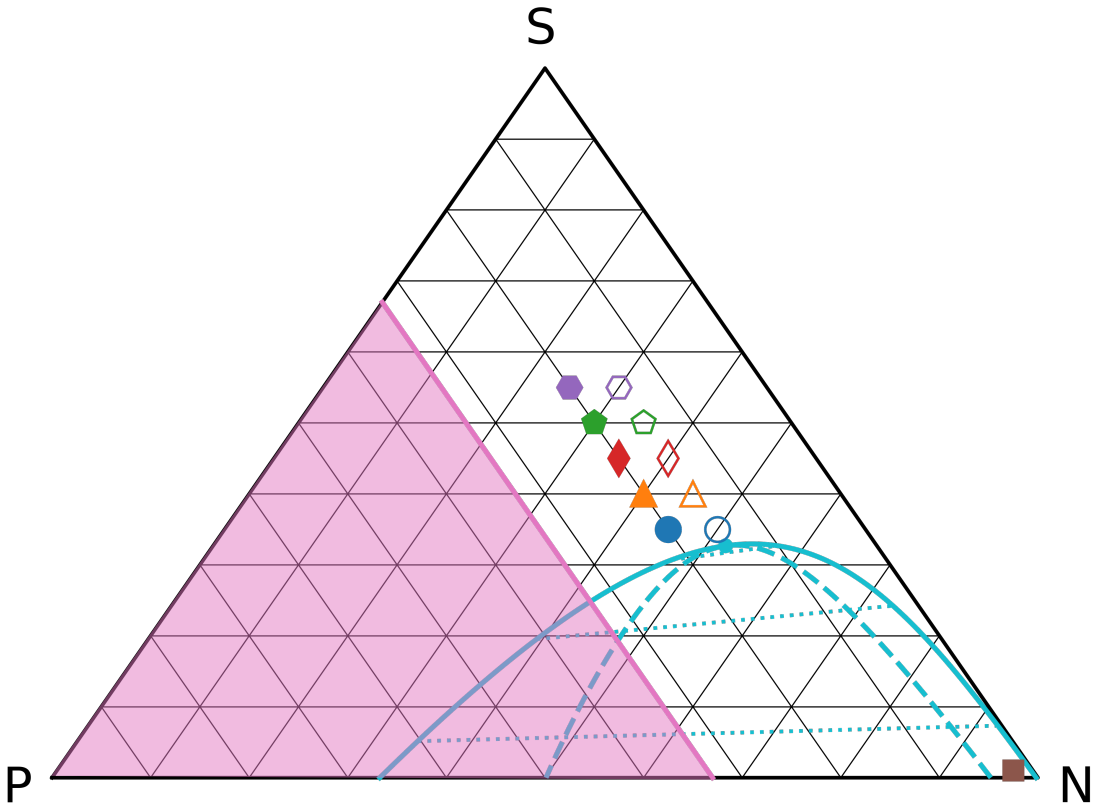

Figure 4.6: Ternary phase diagram for Section 4.4. The solid cyan line marks the binodal while the dashed blue line marks the spinodal, as calculated with Flory-Huggins thermodynamics where $\chi_{pn} = 1.048$, $\chi_{ps} = \chi_{ns} = 0$, $N_p = 20$, $N_n = N_s = 1$. The dotted cyan lines are examples of tie lines. The brown square marks the nonsolvent bath ($\phi_p = 0.02$, $\phi_n = 0.97$). The solid pink line marks the glass transition concentration, $\phi_p^* = 0.33$. Any composition within the shaded pink area is considered "glassy." Different dope compositions are explored. Filled series A compositions ($\phi_p = 0.20$): blue circle A_0 ($\phi_n = 0.45$), orange triangle A_1 ($\phi_n = 0.40$), red diamond A_2 ($\phi_n = 0.35$), green pentagon A_3 ($\phi_n = 0.30$), and purple hexagon A_4 ($\phi_n = 0.25$). Unfilled series B compositions ($\phi_p = 0.15$): blue circle B_0 ($\phi_n = 0.50$), orange triangle B_1 ($\phi_n = 0.45$), red diamond B_2 ($\phi_n = 0.40$), green pentagon B_3 ($\phi_n = 0.35$), and purple hexagon B_4 ($\phi_n = 0.30$).

compositions are moved farther from the binodal.

The corresponding morphologies in Figure 4.8 confirm the expected trend. Figure 4.8a shows the corresponding morpholgy and pore-size distribution for A_1 at the timepoint when the phase-separation front has reached the bottom of the film. Since the phase-separation fronts never reached the bottom of the film for the following simulations, Figures 4.8b, c, and d show corresponding morphologies and pore-size profiles at the maximum simulation time, $t/\tau = 10^4$ for A_2, A_3, and A_4, respectively. Note that the morphology and pore-size profile for A_0 has been shown earlier in Figure 4.3b. Comparing the morphologies reveals that as the dope composition is moved farther from the binodal, the degree of asymmetry weakens. We also observe that the film experiences more shrinkage due to the delayed phase separation. Finally, we note that compositions closer to the binodal (A_0 and A_1) exhibit tortuous finger-like structures while those dope compositions farther from the binodal (A_2 and A_3) lead to more vertically oriented pores.

Figure 4.9 plots the phase-separation and glass-transition fronts for series B dope compositions. Compared to series A dope compositions, both the phase-separation and glass-transition fronts move faster due to the inversion of the continuous phase from polymer-rich to polymer-poor. Nevertheless, the propagation of a phase-separation front becomes slower as the dope composition is moved farther from the binodal. However, we observe an unexpected trend: the gap between the phase-separation and glass-transition fronts widen for dope compositions farther away from the binodal; the trend holds from B_0 to B_3. Thus, we expect the degree of asymmetry to increase from B_0 to B_3.

The corresponding morphologies in Figure 4.10 confirm the expected trend. Figure 4.10 shows the corresponding morpholgies and pore-size distributions for B_1, B_2, B_3, and B_4. Note that the morphology and pore-size profile for B_0 has been shown earlier in Figure 4.5b. Comparing morphologies reveals that as the dope composition is moved farther from the binodal, the degree of asymmetry increases. We cannot make

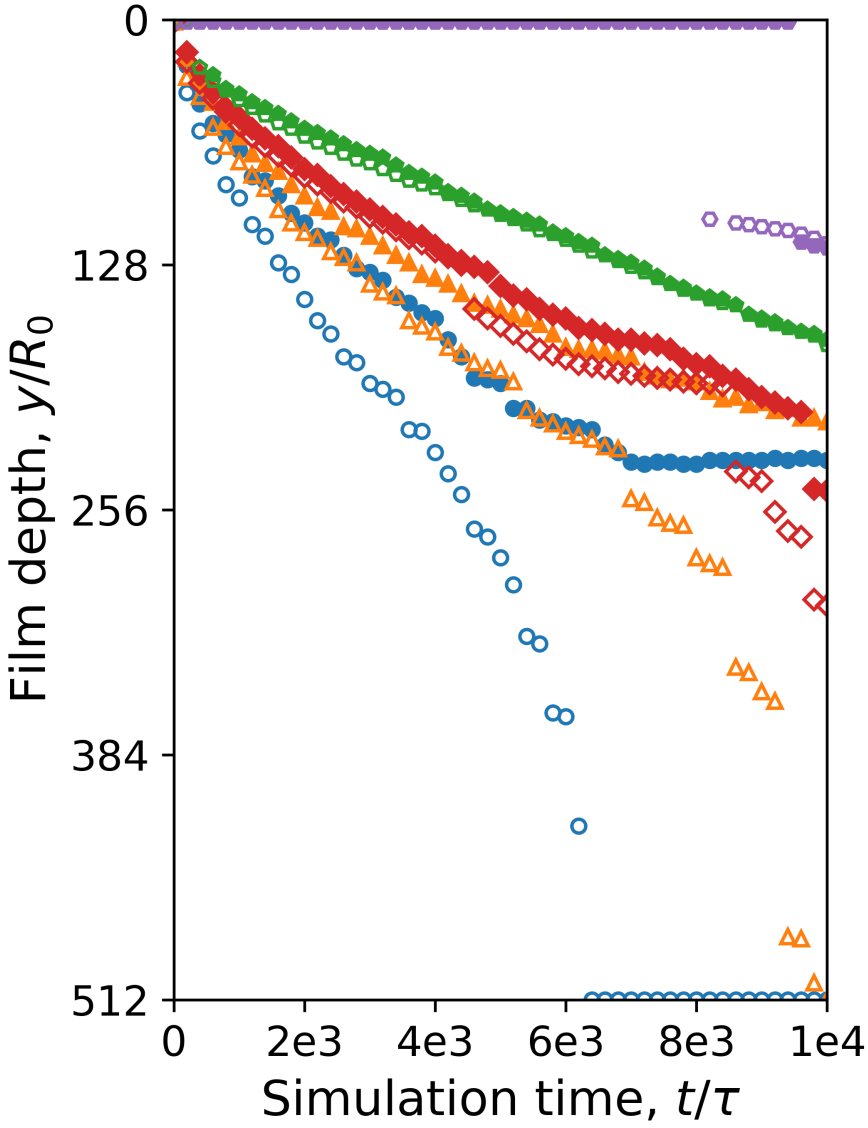

Figure 4.7: Propagation dynamics of the phase-separation (unfilled markers) and glass-transition (filled markers) fronts for the series A dope compositions ($\phi_p = 0.20$): blue circles A_0 ($\phi_n = 0.45$), orange triangles A_1 ($\phi_n = 0.40$), red diamonds A_2 ($\phi_n = 0.35$), green pentagons A_3 ($\phi_n = 0.30$), and purple hexagons A_4 ($\phi_n = 0.25$). Relative locations of these compositions to the binodal and the glass-transition concentration, $\phi_p^* = 0.33$, are shown in Figure 4.6

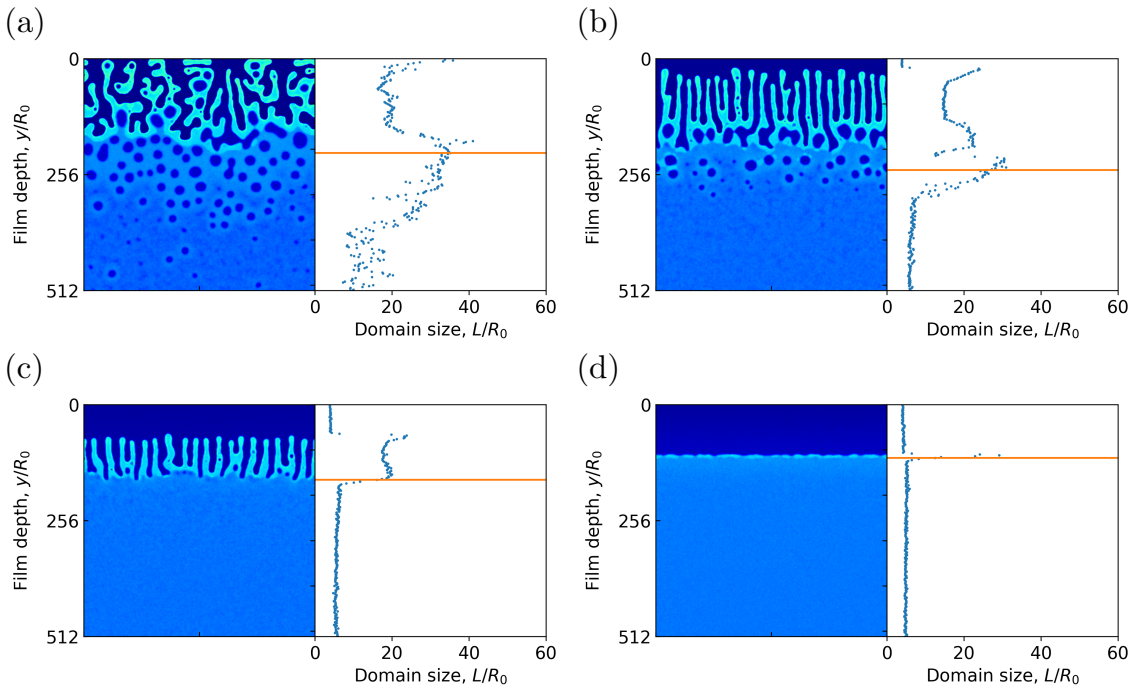

Figure 4.8: Microstructures and domain size profiles for the series A dope compositions ($\phi_p = 0.20$): (a) A_1 ($\phi_n = 0.40$), (b) A_2 ($\phi_n = 0.35$), (c) A_3 ($\phi_n = 0.30$), (d) A_4 ($\phi_n = 0.25$). The y-coordinate corresponds to film depth, where $y = 0$ is the initial film–bath interface and $y = 512$ is the bottom of the film. Polymer-rich regions are light green and polymer-poor regions are dark blue, ϕ_p color bar included in Figure 3.2. The orange line (glass-transition front) in the domain size profile corresponds to the deepest point in the film where at least one grid point has crossed the glass transition concentration, ϕ_p^*. The timepoint shown for (a) corresponds to the moment the phase-separation front has reached the bottom of the film. The timepoint shown for (b), (c), and (d) correspond to the maximum simulation time, $t/\tau = 10^4$, *i.e.,* the phase-separation front never made it to the bottom within practical simulation times. Relative locations of these compositions to the binodal and the glass-transition concentration, $\phi_p^* = 0.33$, are shown in Figure 4.6.

a well-informed conclusion on the degree of asymmetry in dope composition B_4 due to the limited extent of its phase separation. We do still observe increased film-shrinkage with more delay in the phase separation, from B_0 to B_4, as we did for series A dope compositions.

4.5 Conclusions

In this chapter, we showed the effect of moving the glass-transition concentration, ϕ_p^*, and the dope composition, on membrane formation. To form the asymmetric structure, the glass-transition concentration can neither be too close nor too far from the dope composition. For 2D microstructures with a continuous polymer-rich phase, moving the dope composition away from the binodal leads to a weaker degree of asymmetry. However, the opposite trend is observed for 2D microstructures with a continuous polymer-poor phase. In both cases, however, more film shrinkage is observed for dope compositions farther away from the binodal, and we attribute this observation to the increase delay in the phase separation.

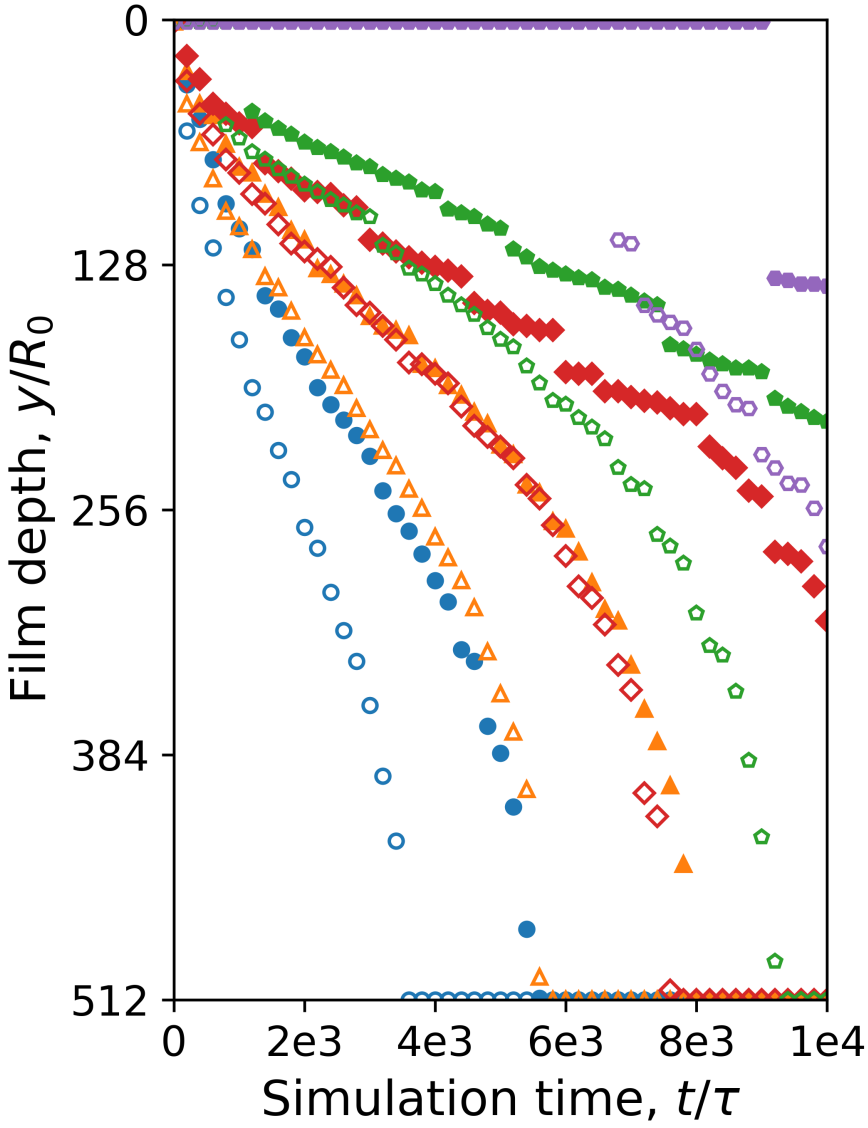

Figure 4.9: Propagation dynamics of the phase-separation (unfilled markers) and glass-transition (filled markers) fronts for the series B compositions ($\phi_p = 0.15$): blue circles B_0 ($\phi_n = 0.50$), orange triangles B_1 ($\phi_n = 0.45$), red diamonds B_2 ($\phi_n = 0.40$), green pentagons B_3 ($\phi_n = 0.35$), and purple hexagons B_4 ($\phi_n = 0.30$). Relative locations of these compositions to the binodal and the glass-transition concentrations, $\phi_p^* = 0.33$, are shown in Figure 4.6.

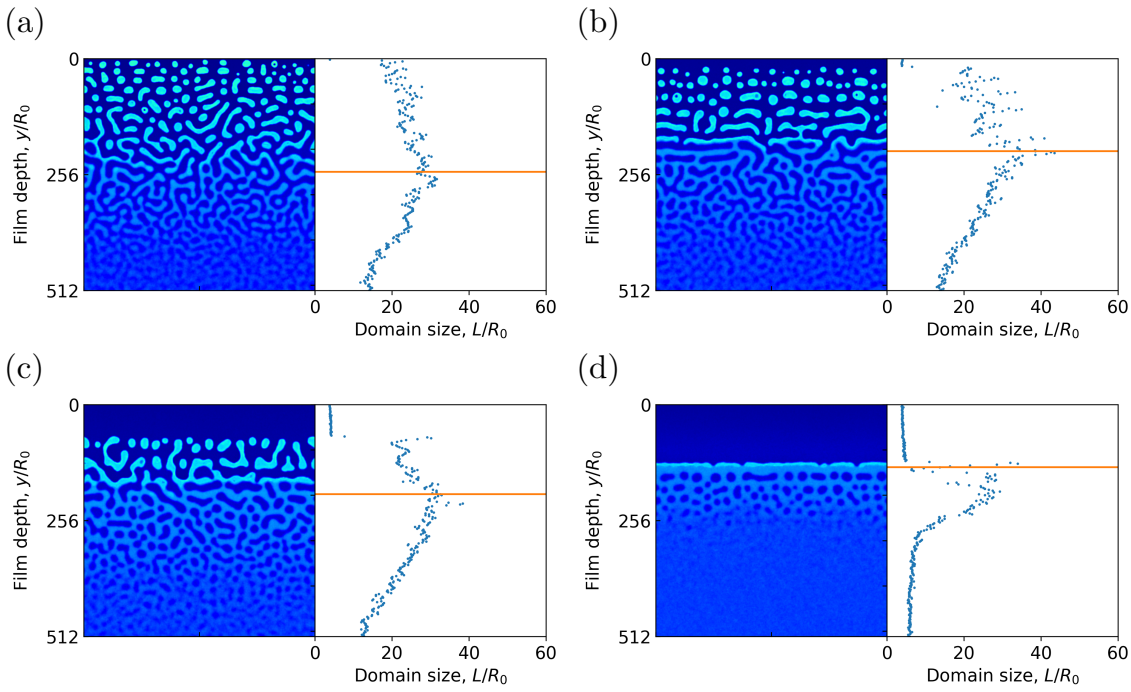

Figure 4.10: Microstructures and domain size profiles for the series B dope compositions ($\phi_p = 0.15$): (a) B_1 ($\phi_n = 0.45$), (b) B_2 ($\phi_n = 0.40$), (c) B_3 ($\phi_n = 0.35$), (d) B_4 ($\phi_n = 0.30$). The y-coordinate corresponds to film depth, where $y = 0$ is the initial film–bath interface and $y = 512$ is the bottom of the film. Polymer-rich regions are light green and polymer-poor regions are dark blue, ϕ_p color bar included in Figure 3.2. The orange line (glass-transition front) in the domain size profile corresponds to the deepest point in the film where at least one grid point has crossed the glass transition concentration, ϕ_p^*. The timepoints shown for (a), (b), and (c) correspond to the moment the phase-separation front has reached the bottom of the film. The timepoint shown for (d) corresponds to the maximum simulation time, $t/\tau = 10^4$, *i.e.,* the phase-separation front never made it to the bottom within practical simulation times. Relative locations of these compositions to the binodal and the glass-transition concentrations, $\phi_p^* = 0.33$, are shown in Figure 4.6.

Chapter 5

Coarsening Dynamics with Mobility and Viscosity Contrasts

5.1 Background

In Chapter 3, we showed that together with mass-transfer-driven spinodal decomposition and thermal fluctuations, a structural arrest mechanism is necessary for asymmetric membrane formation. We implmented the glass transition as the structural arrest mechanism by applying a mobility contrast between the polymer-rich and polymer-poor phases. Using the same glass-transition model, we extended the study of membrane formation to different NIPS formulations in Chapter 4. In both chapters, NIPS simulations were restricted to diffusion-only dynamics, neglecting any potential effects from hydrodynamics. In this chapter, we will address how hydrodynamics alter phase separation. We will also examine how imposing a glass transition changes microstructure evolution in both cases of diffusion-only coarsening and coarsening with hydrodynamics.

5.2 Phase-field model and simulations setup

We use the ternary phase-field model presented in Eqs 2.26 and 2.27. Since the nondimensional and deterministic form of the model is used throughout this chapter, we drop the tildes and remove the fluctuation terms for convenience:

$$\frac{\partial \phi_i(\boldsymbol{r},t)}{\partial t} + \boldsymbol{v}\cdot\boldsymbol{\nabla}\phi_i = \boldsymbol{\nabla}\cdot\left[\sum_j^{p,n} M_{ij}(\{\phi_i\})\boldsymbol{\nabla}\mu_j(\{\phi_i\})\right] \tag{5.1}$$

$$-\boldsymbol{\nabla}p + \boldsymbol{\nabla}\cdot\left[\eta(\{\phi_i\})(\boldsymbol{\nabla}\boldsymbol{v} + \boldsymbol{\nabla}\boldsymbol{v}^T)\right] = N_r\boldsymbol{\nabla}\cdot\boldsymbol{\Pi} \tag{5.2}$$

$$\boldsymbol{\nabla}\cdot\boldsymbol{v} = 0 \tag{5.3}$$

where $\phi_p(\boldsymbol{r},t)$ and $\phi_n(\boldsymbol{r},t)$ are the polymer and nonsolvent volume fractions, M_{ij} is the mobility matrix, μ_j is the chemical potential of species j, p is the pressure, η is the concentration-dependent viscosity, N_r is the reference polymer degree of polymerization, $\boldsymbol{v}$ is the total mixture velocity,

$$\boldsymbol{v} = \sum_i^{p,n,s} \phi_i \boldsymbol{v}_i, \tag{5.4}$$

and $\boldsymbol{\nabla}\cdot\boldsymbol{\Pi}$ is the divergence of the osmotic stress tensor calculated as,

$$\boldsymbol{\nabla}\cdot\boldsymbol{\Pi} = \sum_i^{p,n} \phi_i \boldsymbol{\nabla}\mu_i. \tag{5.5}$$

As outlined in Section 2.4, we nondimensionalized our model using R_0, the root-mean-square (RMS) end-to-end distance of a reference polymer with degree of polymerization N_r as the characteristic length scale ($R_0 = bN_r^{1/2}$), τ, the Rouse time of the reference polymer in a solvent of viscosity, η_s, as the characteristic time scale ($\tau = N_r^2\eta_s b^3/k_BT$), b^2/η_s as the characteristic mobility scale, $N_r k_BT/b^3$ as the characteristic chemical potential scale, and η_s/τ as the characteristic pressure scale. The solvent volume fraction is implicitly determined from the incompressibility constraint, $\phi_s = 1 - \phi_p - \phi_n$. The

chemical potential, μ_j, is calculated as the functional derivative of the free energy of the system, $\mu_j = \delta F/\delta\phi_i$, where the free energy functional is given by [40],

$$F\left[\{\phi_i\}\right] = \int \mathrm{d}\mathbf{r}\left[f(\{\phi_i\}) + g(\{\phi_i\})\right] \tag{5.6a}$$

$$f(\{\phi_i\}) = \sum_i^{p,n,s} \frac{\phi_i}{N_i}\ln\phi_i + \frac{1}{2}\sum_{i\neq j}^{p,n,s}\chi_{ij}\phi_i\phi_j \tag{5.6b}$$

$$g(\{\phi_i\}) = \frac{1}{2}\begin{bmatrix}\boldsymbol{\nabla}\phi_p & \boldsymbol{\nabla}\phi_n\end{bmatrix}\begin{bmatrix}\kappa_p+\kappa_s & \kappa_s \\ \kappa_s & \kappa_n+\kappa_s\end{bmatrix}\begin{bmatrix}\boldsymbol{\nabla}\phi_p \\ \boldsymbol{\nabla}\phi_n\end{bmatrix}. \tag{5.6c}$$

Eqs. 5.6b and 5.6c are the bulk and interfacial free energy contributions, respectively. The degree of polymerization for each component is set to, $N_p = 20, N_n = N_s = 1$, with the reference, $N_r = 20$. The Flory-Huggins interaction parameters are fixed at, $\chi_{pn} = 1.1$, $\chi_{ps} = \chi_{ns} = 0$, and the square-gradient coefficients are set to, $\kappa_p = \kappa_n = \kappa_s = 2.5$. Details of our model and numerical methods are included in Chapter 2.

The mobility and viscosity models are especially important for the motivation of this chapter. The concentration-dependent local mobilities are defined by

$$M_{pp} = \phi_p(1-\phi_p)/\eta \tag{5.7a}$$

$$M_{pn} = M_{np} = -\phi_p\phi_n/\eta \tag{5.7b}$$

$$M_{nn} = \phi_n(1-\phi_n)/\eta. \tag{5.7c}$$

Note that the local mobilities of all components are scaled by the inverse of the concentration-dependent viscosity, η. Mobility and viscosity contrasts between the polymer-rich and polymer-poor phases can then be imposed by modeling η as a sigmoidal function of the

local polymer volume fraction, $\phi_p(\boldsymbol{r})$:

$$\eta = 1 + \frac{\eta_p/\eta_s - 1}{1 + \exp\left(-\frac{1}{w}\left(\phi_p(\boldsymbol{r}) - \phi_p^*\right)\right)} \tag{5.8}$$

where η_p/η_s is the pure-component viscosity ratio of the polymer and the solvent (implicitly assuming $\eta_n = \eta_s$), w sets the width of the sigmoid, and ϕ_p^* is the glass-transition concentration. A sigmoid mimics the exponential growth in viscosity predicted by the Vogel-Fulcher-Tamman-Hesse (VFTH) and Williams-Landel-Ferry (WLF) relations[42] while bounding the maximum value of η for computational stability. Setting $w = 1 \times 10^{-3}$ approximates η as a step function, narrow enough such that $\eta = 1$ at $\phi_p = 0$, but wide enough to avoid computational issues associated with a mathematical discontinuity. This choice implies that for ϕ_p values far enough from ϕ_p^*, $\eta = 1$ for $\phi_p(\boldsymbol{r}) < \phi_p^*$, while $\eta = \eta_p/\eta_s$ for $\phi_p(\boldsymbol{r}) > \phi_p^*$.

The model presented in this chapter so far is consistent with the 'Model H' universality class outlined by Hohenberg and Halperin [41], describing the dynamics of a conserved incompressible system that evolves with diffusion and hydrodynamics. In this chapter, we are particularly interested in understanding the contribution of hydrodynamics to the coarsening of phase-separated microstructures. Thus, we also consider 'Model B' simulations where the conserved incompressible system evolves only by diffusion. In our formulation, Model B can be achieved by setting all velocities in Model H to zero:

$$\frac{\partial \phi_i(\boldsymbol{r}, t)}{\partial t} = \boldsymbol{\nabla} \cdot \left[\sum_j^{p,n} M_{ij}(\{\phi_i\}) \boldsymbol{\nabla} \mu_j(\{\phi_i\}) \right] \tag{5.9}$$

where the mobility matrix, M_{ij}, and the chemical potentials, μ_j are determined in the same manner as they were in Model H. Although the momentum equation loses significance in Model B, the local viscosity, η, remains as a sigmoidal function that scales the

component mobilities in the same fashion as they were for Model H.

As we focus on the effects of the mobility and viscosity contrasts in both Model B and Model H, the scope of the current chapter is limited to bulk simulations of phase separation. Simulations in this chapter are set in a $512R_0 \times 512R_0$ box, discretized by a 1024×1024 grid. Periodic boundary conditions are imposed on all sides of the box to simulate bulk phase separation. Compositions are initialized homogeneously within the spinodal region and seeded with random noise of zero mean to kick off phase separation. In the case of Model H, velocity fields are homogeneously initialized to zero without any added noise. The phase-field models were solved using the pseudo-spectral method due to its unparalleled accuracy and ease of implementation[44], combined with a semi-implicit time-stepping scheme[45, 36] to balance computational costs with the need for a numerically stable solution. We leave further details of the numerical methods to our original methods paper.[33]

5.3 Domain characterization

5.3.1 Characterisitic domain size

The characteristic domain size of a 2D microstructure is calculated using

$$L = \frac{2\pi}{\langle q \rangle} \tag{5.10}$$

where the first moment of the structure factor modes is given by

$$\langle q \rangle = \frac{\sum\limits_{q} q\, s_p(q,t)}{\sum\limits_{q} s_p(q,t)}. \tag{5.11}$$

The normalized structure factor of the polymer is calculated using

$$s_p(q,t) = \frac{S_p(q,t)}{\sum\limits_q S_p(q,t)} \tag{5.12}$$

where $S_p(q,t)$ is isotropically averaged from the Fourier transform of the pair-correlation function,

$$S_p(\boldsymbol{q},t) = \frac{1}{V}\sum_{\boldsymbol{r}}\sum_{\boldsymbol{r'}} e^{-i\boldsymbol{q}\cdot\boldsymbol{r}}\left[\phi_p(\boldsymbol{r}+\boldsymbol{r'},t)\phi_p(\boldsymbol{r'},t) - \langle\phi_p\rangle^2\right] \tag{5.13}$$

and V is the number of lattice points.

5.3.2 Characteristic shape and phase continuity

In addition to size, we can also measure the characteristic shape of a 2D microstructure by examining the shape of its discrete domains. We quantify the 'circularity' of an individual 2D domain using

$$c = \frac{P^2}{4\pi A} \tag{5.14}$$

where P is the perimeter of the domain and A is its area. The value of c becomes large for a thin and elongated—'stringy'—domain, while c becomes small, approaching unity as the domain becomes circular. The perimeter of a domain is calculated using the Freeman chain code[63] and the area is estimated by the number of pixels within the domain. The shape factor for the microstructure is then taken as the weighted average of c for all discrete domains:

$$C = \frac{\sum\limits_i c_i A_i}{\sum\limits_i A_i}. \tag{5.15}$$

We heuristically determined that the threshold for circularity, *i.e.,* the shape factor value below which all minority domains in a given morphology are qualitatively circular, is $C_{circle} = 1.20$. We also characterized phase continuity numerically using the burning

algorithm.[64] A phase is designated continuous if it traverses two opposing sides of a periodic simulation box.

5.3.3 Characterizing phase composition and phase fraction

We measured the compositions of the polymer-rich (α) and polymer-poor (β) phases by building a histogram of the independent volume fraction fields (ϕ_p and ϕ_n) where each bin has a width of 0.04. The polymer concentrations in the α and β phases, ϕ_p^α and ϕ_p^β, were calculated as the averages of the highest-occupied bin and the lowest-occupied bin, respectively. Calculation of the nonsolvent phase compositions, ϕ_n^β and ϕ_n^α were done similarly. We observed that using a histogram is a more robust approach than simply taking the extrema of ϕ_i as a measure of ϕ_i^α and ϕ_i^β.

The fraction of the polymer-rich phase, f^α, was computed by thresholding the polymer-concentration field into a binary field, where the threshold value is determined as the average of ϕ_p^α and ϕ_p^β.

5.3.4 The fastest-growing mode and the rate of spinodal decomposition

In an earlier work [33], we showed that the difference in coarsening dynamics of two systems with qualitatively similar microstructures (discrete polymer-poor clusters in a polymer-rich matrix) but with different quench depths are due to the differences in their fastest-growing modes, q_m, and the rate of spinodal decomposition, λ_m. In the present work, we explore the coarsening dynamics for qualitatively different microstructures. Thus, we find it convenient to normalize the domain growth-simulation time curves to take out the effects introduced by differences in quench depth. We scaled the characteristic domain size by the characteristic domain size that corresponds to the fastest growing

mode, $2\pi/q_m$, and scale time by the timescale that corresponds to the rate of spinodal decomposition, $1/\lambda_m$. Expressions for q_m and λ_m were derived through a linear stability analysis of Model B, and details of these calculations are discussed by Tree et al.[33]

5.4 Ternary phase diagrams

NIPS is often rationalized using ternary phase diagrams as shown in Figure 5.1. Polymer solution films are cast in the homogeneous region, H, and then immersed in the nonsolvent bath. Mass transfer of the nonsolvent into the film induces phase separation as local compositions enter the binodal region—the union of Regions A and B. We distinguish between these two regions due to their equilibrium morphologies: Region A microstructures are discrete polymer-poor clusters in a polymer-rich matrix, and vice-versa for Region B. These phase-separated domains then coarsen, and the polymer-rich region eventually solidifies, entering the glassy region, G. We discuss the dynamics of mass transfer-induced phase separation in a separate publication[34] and focus on coarsening kinetics and solidification in this present study.

We explore the coarsening of ternary polymer solution in two parts. Figure 5.1a represents Sections 5.5 and 5.6 where the mixture viscosity is set constant, *i.e.,* the viscosity contrast in Eq 5.8 is set to unity, $\eta_p/\eta_s = 1$. For Model H, this part translates to a Newtonian fluid. Figure 5.1b represents Sections 5.7 and 5.8 where mobility and viscosity contrasts of different magnitudes are applied by setting η_p/η_s accordingly in Eq. 5.8. The glassy region, G, corresponds to local compositions where $\phi_p > \phi_p^*$, *i.e.,* the compositions where the local mobilities are scaled by η_p/η_s. Thus, the solid glassy phase is modeled as a highly viscous fluid. For most simulations in this chapter, $\phi_p^* = 0.4$; any deviation from this value will be explicitly stated.

The simulation boxes are initialized with uniform compositions within the spinodal

region. Though we did not consider phase-separated morphologies formed by nucleation, coarsening kinetics of such microstructures are similar to those produced by spinodal decomposition for dilute concentrations. We introduced random noise to the initial compositions to kick off spinodal decomposition. Due to mass conservation and incompressibility, the average composition of a simulation box does not change from its initial value,$(\phi_p^0,\ \phi_n^0,\ \phi_s^0)$; note that we use the same notation for the average composition in this chapter. The location of this average composition within the binodal determines the equilibrium morphology of the simulation box, as shown in Figure 5.1. Thus, we study the dynamics of microstructural evolution for different average compositions, by diffusion and with hydrodynamics, for the case without (Sections 5.5 and 5.6) and with (Sections 5.7 and 5.8) mobility and viscosity contrasts between the polymer-rich and polymer-poor domains.

5.5 Coarsening by diffusion (Model B), without mobility contrasts

Figure 5.2 illustrates microstructure evolution by diffusion for a near-symmetric mixture without mobility contrasts. Immediately after spinodal decomposition, the morphology stays bicontinuous. Coarsening proceeds mostly by the reshaping of domains through interfacial diffusion as the system minimizes interfacial energy. Except for perfectly symmetric mixtures, bicontinuity is eventually broken, leading to discrete minority domains, as shown in the second frame. At this point, coarsening by domain coalescence (the fusion of adjacent domains as they grow) and bulk diffusion (evaporation-condensation, *i.e.,* Ostwald ripening) also come into play. Domain coalescence becomes less significant as domains grow larger and become fewer in number as there are no external forces—

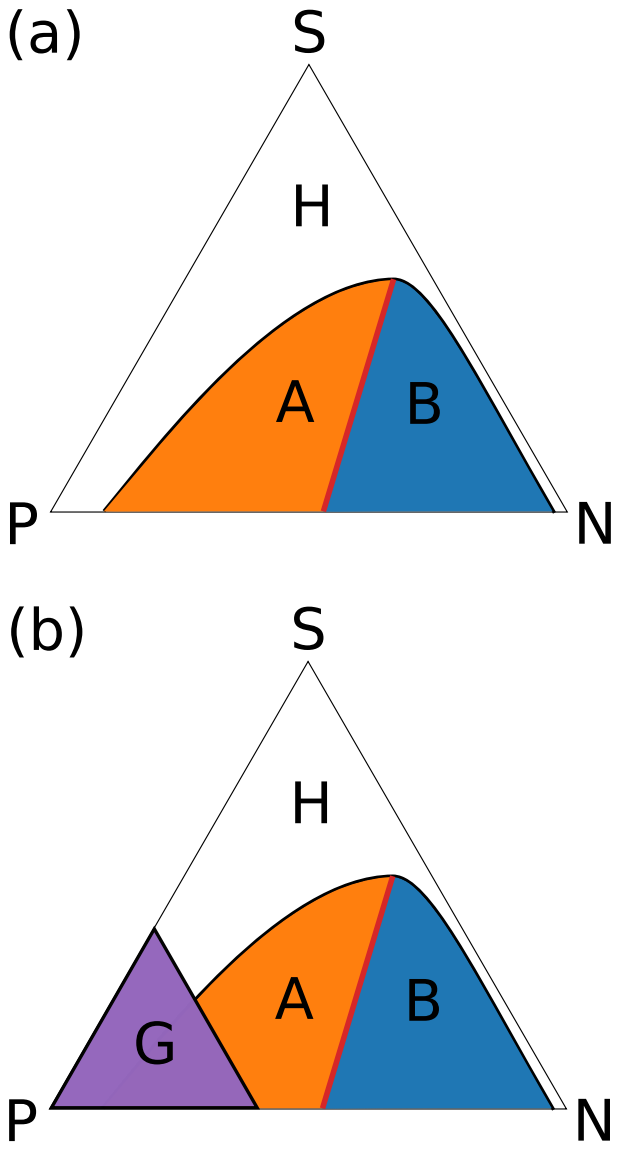

Figure 5.1: Representative ternary (polymer-solvent-nonsolvent) phase diagrams (a) without and (b) with mobility and viscosity contrasts. Region H is the homogeneous region where polymer solution films are cast. Regions A and B are under the binodal. Equilibrium morphologies in Region A are polymer-rich matrix surrounding polymer-poor clusters and vice-versa for Region B. The red line between A and B marks symmetry between polymer-rich and polymer-poor phases. Region G is the glassy region, where $\phi_p > \phi_p^*$. For most simulations in this chapter, $\phi_p^* = 0.4$; any deviation from this value will be explicitly stated. Note that the spinodal boundary between the unstable and metastable areas of the binodal region is not shown.

such as thermal fluctuations or externally imposed flows—to push the discrete domains closer to each other. Interfacial diffusion also becomes less important as domains finish reshaping from stringy to circular, as shown by the third frame when the shape metric transitions to $C < C_{circle}$. In the end, the microstructure becomes a collection of discrete circular domains that continue to coarsen only by bulk diffusion.

Coarsening dynamics change with average composition, (ϕ_p^0, ϕ_n^0, ϕ_s^0). Figure 5.3a shows domain size growth for different average compositions along a constant ϕ_s^0–axis within the spinodal. To remove the effects of quench depth from the dynamics, domain size and simulation time were scaled accordingly as discussed in Section 5.3.4. Curves are colored consistently with Figure 5.1, where the orange and blue curves correspond to average compositions in Regions A and B, respectively. The long–time coarsening trend for each curve corresponds to their equilibrium microstructure: orange curves collapse while the blue curves eventually follow the trend set by the blue circles, the average composition with the least polymer content. We can understand the difference between the two long–time coarsening trends (the orange trend and the blue circles trend) by examining the diffusivities that arise from our phase-field model. As outlined by Tree et al.[33], the polymer diffusivities in the dilute–polymer limit are given by,

$$\lim_{\phi_p \to 0} D_{pp} = \frac{k_B T}{\zeta_0 N_p} \tag{5.16}$$

$$\lim_{\phi_p \to 0} D_{pn} = 0, \tag{5.17}$$

and the nonsolvent diffusivities in the dilute–nonsolvent limit are given by,

$$\lim_{\phi_n \to 0} D_{nn} = \frac{k_B T}{\zeta_0 N_n} \tag{5.18}$$

$$\lim_{\phi_n \to 0} D_{np} = 0. \tag{5.19}$$

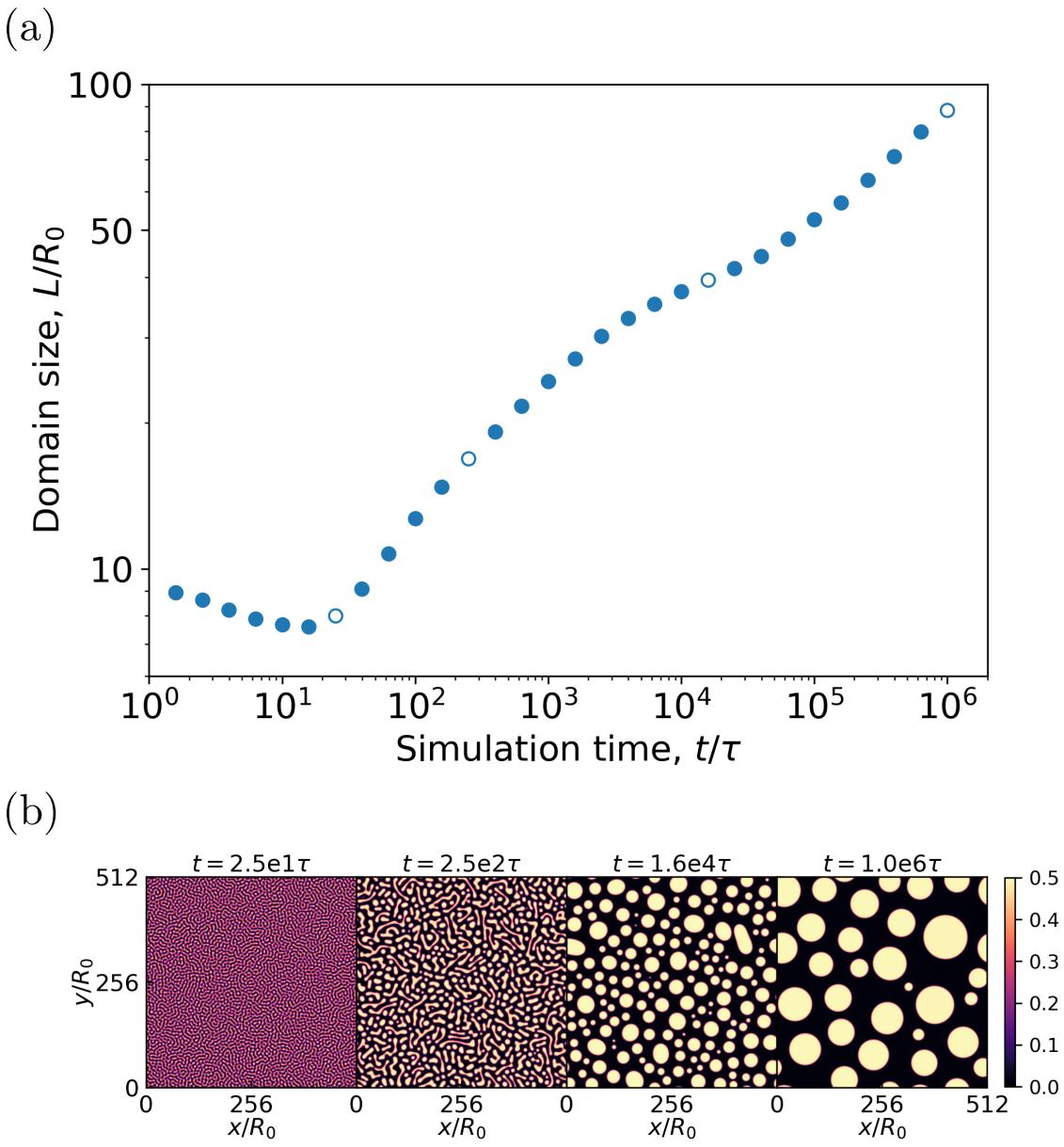

Figure 5.2: (a) Domain size growth for an average composition of (ϕ_p^0=0.20, ϕ_n^0=0.60, ϕ_s^0=0.20). The unfilled markers in (a) correspond to the morphologies shown in (b), where the color bar represents ϕ_p. From left to right, C=10.6, 3.0, 1.1, 1.1.

As shown in Figure 5.2, long–time microstructures constitute circular clusters that coarsen only by bulk diffusion of material from the smaller clusters to the larger clusters, *i.e.,* Ostwald ripening. For the orange curves in Region A, the long–time microstructures are discrete polymer-poor clusters in a polymer-rich matrix, and vice-versa for the blue curves in Region B. In the former, the long–time coarsening mechanism is the diffusion of nonsolvent between clusters across a polymer-rich matrix, and vice-versa for the latter. Comparing Eqs. 5.16 and 5.18 reveals that bulk diffusion of nonsolvent and solvent across a polymer-rich matrix should be faster than the diffusion of polymer material across a polymer-poor matrix by a factor of N_p/N_n. Figure 5.3b demonstrates this inference with the long-time collapse of all curves by shifting the time axis for the blue curves by a factor of N_p/N_n earlier than the orange curves. Also, note that the long-time coarsening rate follows $t^{1/3}$ growth, consistent with the Lifshitz-Slyozov-Wagner (LSW) scaling law for bulk diffusion [54, 55].

In addition to long–time coarsening behavior, Figure 5.3a also illustrates transient differences among average compositions. We do not observe significant differences in the transient behavior of the orange curves, suggesting equivalent dynamics among the orange curves after accounting for quench-depth effects. This observation is not true for the blue curves; they temporarily follow the orange curves, before eventually collapsing on the long–time trend set by the blue circles. The blue circles represent the limiting case where the average composition is dilute enough in polymer such that its microstructure immediately becomes circular polymer-rich clusters after spinodal decomposition, *i.e.,* its average composition is so dilute in polymer that its phase-separated morphology resembles microstructures engendered from nucleation. As shown in Figure 5.1, equilibrium compositions in Region B become more symmetric with more polymer content. In fact, the transition of the blue curves from the orange trend to the blue-circle trend correlates with the transition of the morphology from discrete curvy domains to discrete

circular domains. The unfilled markers in Figure 5.3 show the shape metric transition, $C < C_{circle}$. Before the shape transition, domains are stringy and mostly coarsen by reshaping through interfacial diffusion; however, after the shape transition, the discrete domains become circular and coarsen only by bulk diffusion, slowing down their growth towards the limiting case set by the blue circles.

5.6 Coarsening with hydrodynamics (Model H), without mobility and viscosity contrasts

Figure 5.4 illustrates microstructure evolution with hydrodynamics for a near-symmetric mixture without mobility and viscosity contrasts. Domains start bicontinuous but quickly break up into discrete stringy domains, as shown in the first and second frames. Unlike diffusion-only coarsening, capillary flows engendered from the non-planar and non-circular interfaces of the bicontinuous morphology accelerate domain growth, which in itself leads to a faster breakup of bicontinuity. Capillary flows continue to get stronger until the discrete domains transition from stringy to circular, as shown by the third frame. As circular domains do not generate capillary flows, coarsening from this point only proceeds by diffusion, and non-zero velocities are only observed for the occasional domain coalescence.

Figure 5.5a shows domain size growth, with hydrodynamics, for different average compositions along a constant ϕ_s^0–axis within the spinodal. Similar to Figure 5.3, differences in the dynamics due to quench depth were removed by scaling the domain-size and simulation-time axes as described in Section 5.3.4. Curves are colored consistently with Figure 5.1, where the orange and blue curves mark average compositions in Regions A and B, respectively. We observe two long–time trends, one set by the orange squares, and

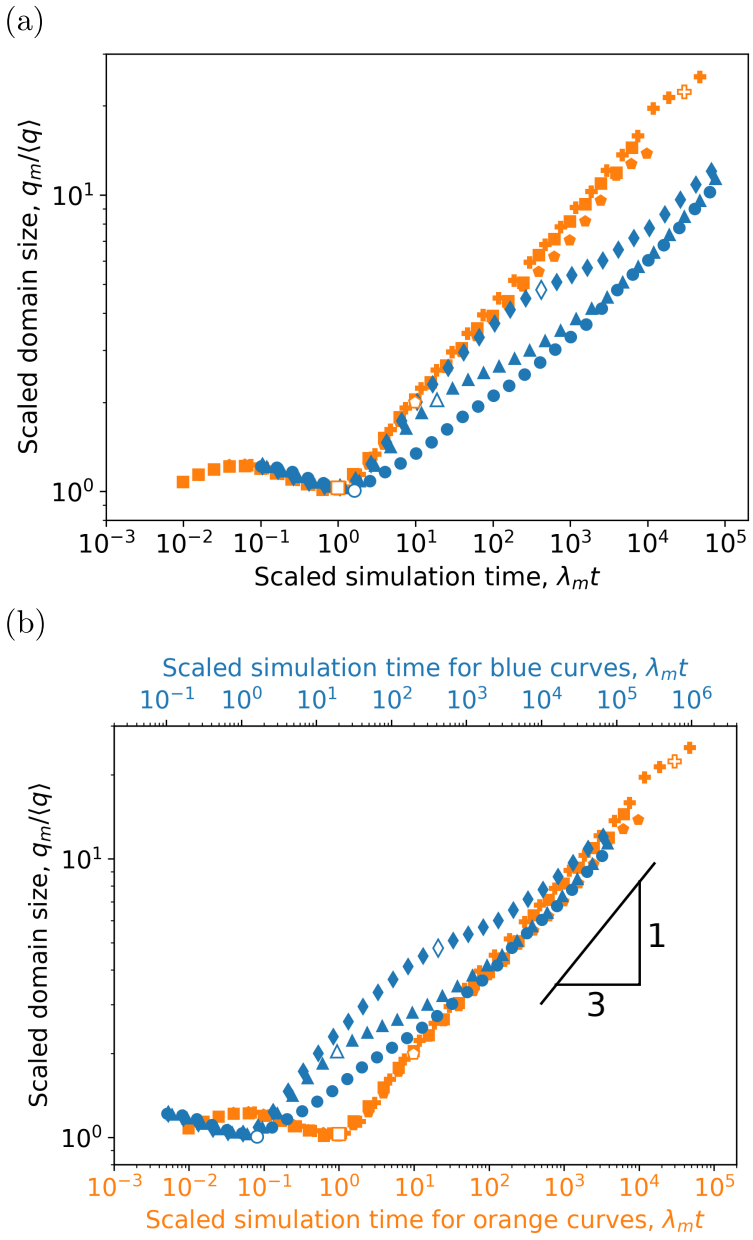

Figure 5.3: (a) Domain size growth by diffusion for different average compositions with the same solvent content ($\phi_s^0 = 0.20$): $\phi_p^0 = 0.12$ (blue circles), 0.16 (blue triangles), 0.20 (blue diamonds), 0.24 (orange pluses), 0.28 (orange pentagons), and 0.32 (orange squares). Orange and blue curves correspond to compositions in Regions A and B, respectively, as shown in Figure 5.1. To remove the effects of quench depth from the dynamics, domain size was scaled with the reciprocal of the fastest growing mode ($2\pi/q_m$), while simulation time was scaled with the reciprocal of the rate of spinodal decomposition ($1/\lambda_m$). Unfilled markers indicate when the discrete phase turns circular, *i.e.,* transition to $C < C_{circle}$. The same data is shown in (b) but simulation time is shifted by a factor of N_p/N_n earlier for the blue curves than the orange curves. Black line is guide for $t^{1/3}$ growth.

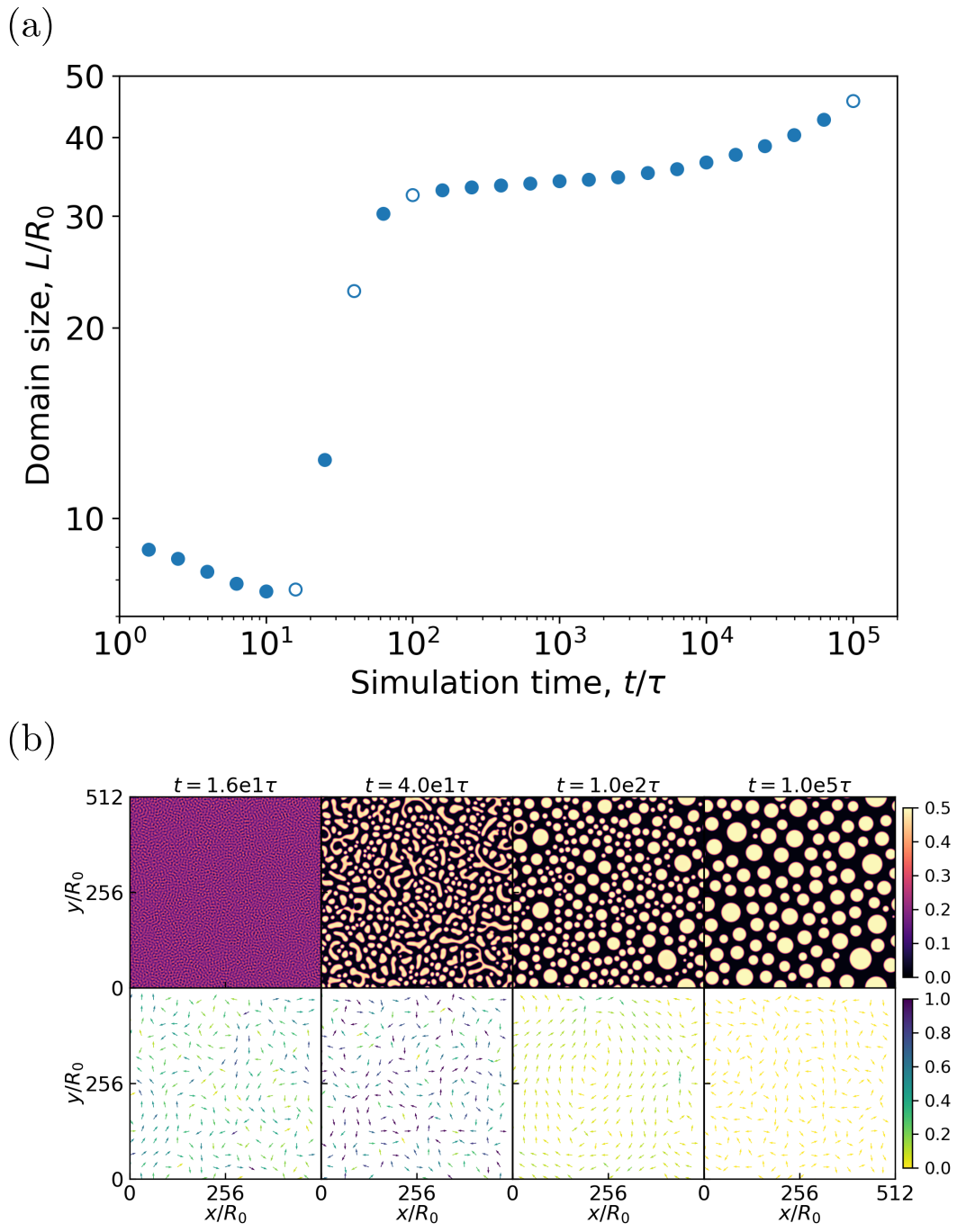

Figure 5.4: (a) Domain size growth for an average composition of (ϕ_p^0=0.20, ϕ_n^0=0.60, ϕ_s^0=0.20). The unfilled markers in (a) correspond to the morphologies shown in the top row of (b), where the color bar represents ϕ_p. From left to right, C=26.7, 2.3, 1.1, 1.1. The bottom row of (b) shows the corresponding velocity fields where the unit vectors show direction and vector colors show velocity magnitudes, as indicated by the corresponding color bar. Stringy domains lead to capillary flows as shown by higher speeds in the first two frames.

another by the blue circles. The orange squares represent the limiting case in Region A, where the average composition has enough polymer such that the morphology immediately after spinodal decomposition is composed of circular polymer-poor clusters. The blue circles represent the limiting case in Region B, where the morphology immediately after spinodal decomposition consists of circular polymer-rich clusters in a polymer-poor matrix. Akin to Figure 5.3a, the difference between the orange-square and blue-circle trends can be explained by comparing Eqs 5.16 and 5.18: nonsolvent diffuses by a factor of N_p/N_n faster than polymer. Figure 5.3b supports this claim by presenting the same set of data with the simulation-time axis for the blue curves shifted earlier by a factor of N_p/N_n, leading to the collapse of both long–time trends that follow $t^{1/3}$ growth, as predicted for the dynamics of bulk diffusion [54, 55].

Figure 5.5 also reveals transient differences in coarsening behavior due to average composition. As shown by Figure 5.4, capillary flows generated from non-planar and non-circular interfaces accelerate coarsening to follow t^1 growth, consistent with the Siggia coarsening mechanism [65]. However, coarsening slows down to diffusion-only growth when minority domains become circular (marked by unfilled symbols) as capillary flows disappear. Since more symmetric mixtures tend to preserve non-circular interfaces longer, we observe that average compositions closer to the symmetry line (orange pluses and blue diamonds) can coarsen with t^1 growth longer than those closer to either side of the binodal. However, this accelerated growth is not a permanent advantage for near-symmetric mixtures. Since capillary flows have driven the morphologies to circular clusters, the only coarsening mechanism left during the transition towards their respective long–time trends is bulk diffusion, and its effects are muted for morphologies with larger, but fewer domains. In the end, bulk diffusion effects catch up, resulting in the eventual collapse of all curves for long times, as shown in Figure 5.5b.

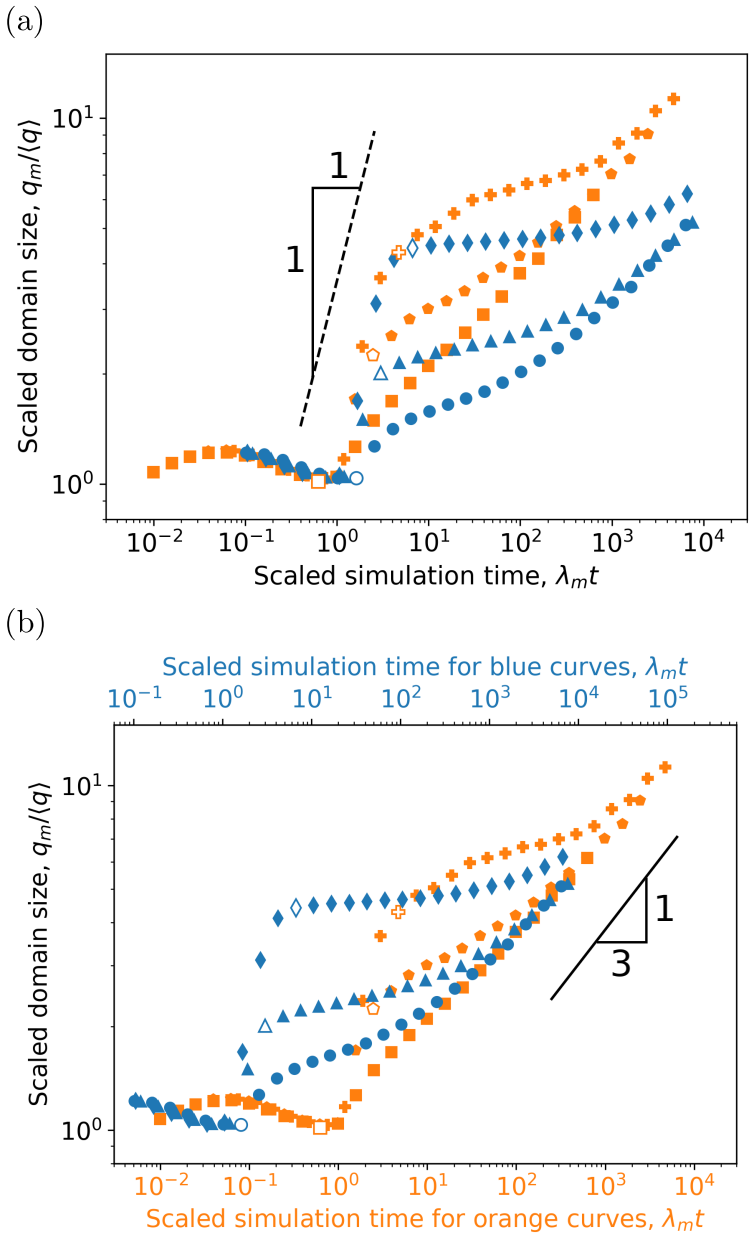

Figure 5.5: (a) Domain size growth with hydrodynamics for different average compositions with the same solvent content ($\phi_s^0 = 0.20$): $\phi_p^0 = 0.12$ (blue circles), 0.16 (blue triangles), 0.20 (blue diamonds), 0.24 (orange pluses), 0.28 (orange pentagons), and 0.32 (orange squares). Orange and blue curves correspond to compositions in Regions A and B, respectively, as shown in Figure 5.1. To remove the effects of quench depth from the dynamics, domain size was scaled with the reciprocal of the fastest growing mode ($2\pi/q_m$), while simulation time was scaled with the reciprocal of the rate of spinodal decomposition ($1/\lambda_m$). Unfilled markers indicate when the discrete phase turns circular, *i.e.*, transition to $C < C_{circle}$. The same data is shown in (b) but simulation time is shifted by a factor of N_p/N_n earlier for the blue curves than the orange curves. Dashed and solid black lines are guides for t^1 and $t^{1/3}$ growth, respectively.

5.7 Coarsening by diffusion (Model B), with mobility contrast

In this section, we study the effects of mobility contrast (η_p/η_s) on microstructure evolution by diffusion. We examine three different average compositions along a constant ϕ_s^0–axis: an average composition in Region A (polymer-poor clusters in a polymer-rich matrix), an average composition in Region B (polymer-rich clusters in a polymer-poor matrix), and a near-symmetric average composition. Simulation times in this section are limited to $t/\tau = 10^4$ due to practical restrictions of our computational tools. We also examine the phenomenon of "phase inversion," that is, the switching of the polymer-rich and polymer-poor phases as the majority and minority domains.

Figure 5.6 shows domain size growth in Region A for different levels of mobility contrasts. The circles ($\eta_p/\eta_s = 1$) in Figure 5.6 represent the same data shown by the orange pentagons in Figure 5.3, illustrating coarsening behavior for this average composition without mobility contrasts. From this base case, we observe that increasing the mobility contrast (η_p/η_s) slows down the coarsening of domains. This observation is intuitive for Region A morphologies: discrete polymer-poor domains rely on bulk diffusion to coarsen, but diffusion of nonsolvent across the polymer-rich matrix is reduced by a factor of η_p/η_s, thus mimicking a structural arrest mechanism. We also observe that within the limits of $t/\tau = 10^4$, there is not much difference in the coarsening dynamics of $\eta_p/\eta_s = 10^4$ (squares), 10^6 (diamonds), and 10^8 (crosses). We do expect that differences in their growth rates would be magnified for longer simulation times; coarsening dynamics for lower values of η_p/η_s begin to relax to the base case of $\eta_p/\eta_s = 1$ sooner than for higher values of η_p/η_s.

Figure 5.7 shows coarsening dynamics in Region B for different levels of mobility contrasts. The circles ($\eta_p/\eta_s = 1$) in Figure 5.7a represent the same data shown by the

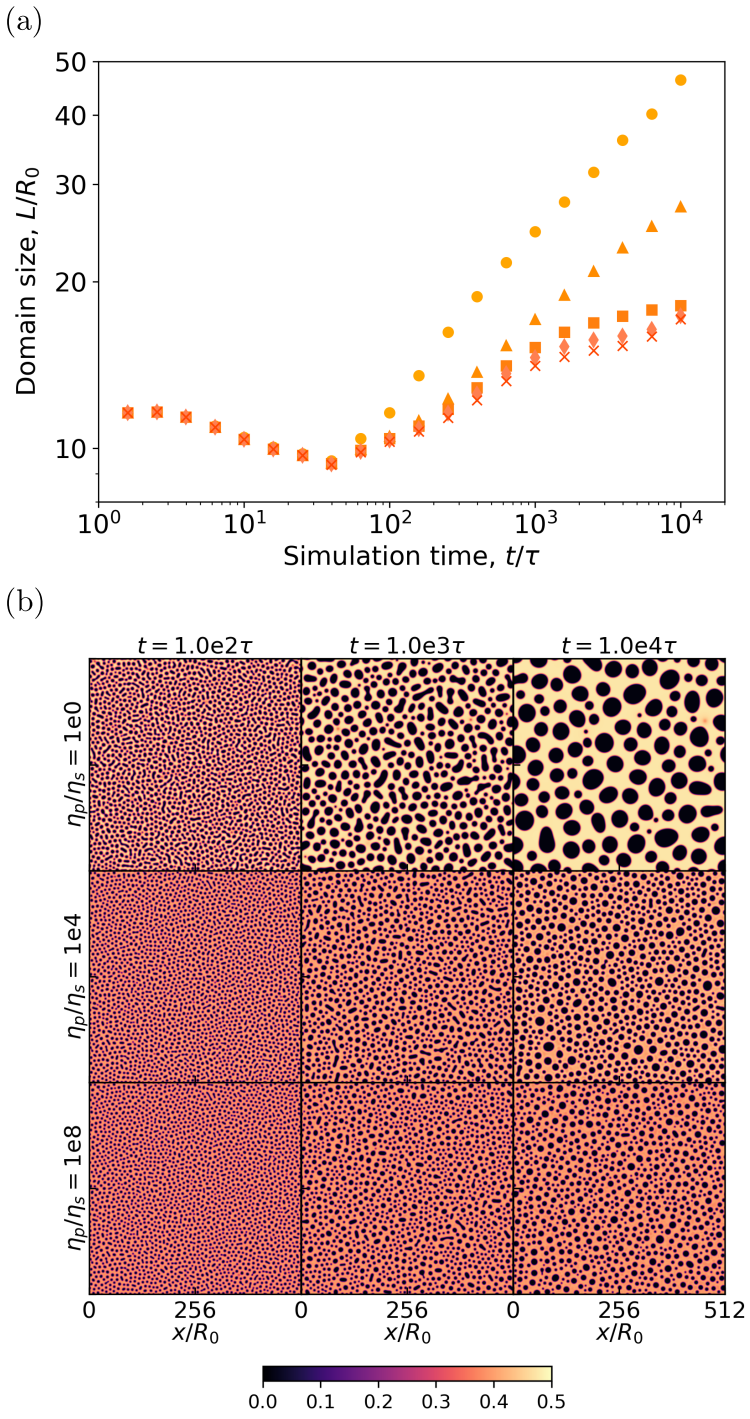

Figure 5.6: (a) Domain size growth by diffusion in Region A (ϕ_p^0=0.28, ϕ_n^0=0.52, ϕ_s^0=0.20) for different mobility contrasts: $\eta_p/\eta_s = 10^0$ (circles), 10^2 (triangles), 10^4 (squares), 10^6 (diamonds), and 10^8 (crosses). Darker symbols correspond to higher η_p/η_s. Corresponding microstructures for η_p/η_s= 10^0 (top row), 10^4 (middle row), and 10^8 (bottom row) are shown in (b), where the color bar represents ϕ_p.

blue triangles in Figure 5.3, illustrating coarsening behavior for this average composition without mobility contrasts. Compared to this base case, we observe that increasing the mobility contrast, even to $\eta_p/\eta_s = 10^8$, does not slow down the coarsening of phase-separated domains. For Region B morphologies, discrete polymer-rich domains rely on bulk diffusion of the polymer across the polymer-poor matrix. Unlike Region A, mobilities in Region B are reduced by a factor of η_p/η_s in the discrete phase, not the continuous phase. As polymer diffusion across the polymer-poor matrix is unhindered, any level of mobility contrast applied would not slow down the coarsening of Region B morphologies.

Closer inspection of domain size and morphologies at $t/\tau = 10^4$ in Figure 5.7 reveals that higher levels of mobility contrast lead to slightly larger domains. This counterintuitive observation is a consequence of composition change in the polymer-rich phase. Figures 5.8a and 5.8b illustrate how mobility contrasts change the local polymer concentrations in the polymer-rich and polymer-poor phases, respectively. For convenience, we designate the polymer-rich phase as the α–phase and its polymer concentration as ϕ_p^α. Similarly, we denote the polymer-poor phase as the β–phase, and its polymer concentration as ϕ_p^β. For $\eta_p/\eta_s = 1$, ϕ_p^α reaches its equilibrium value almost immediately after phase separation, as demonstrated by the circles in Figure 5.8a. The enrichment of the α–phase slows down with increasing levels of mobility contrast. As ϕ_p^α crosses the glass-transition concentration, ϕ_p^*, mobilities in the α–phase are reduced by a factor of η_p/η_s. In fact, raising the mobility contrast to $\eta_p/\eta_s \geq 10^6$ practically freezes enrichment of the α–phase to just above ϕ_p^* within the accessible simulation time, $t/\tau = 10^4$. Similar to the enrichment dynamics of the squares ($\eta_p/\eta_s = 10^4$), we expect that the dynamics of the diamonds ($\eta_p/\eta_s = 10^6$) and crosses ($\eta_p/\eta_s = 10^8$) will relax for longer simulation times and ϕ_p^α for these curves will eventually reach equilibrium. On the other hand, Figure 5.8b shows that ϕ_p^β reaches its equilibrium value with the same dynamics regardless of the level of mobility contrast applied. Due to the conservation of mass, the decrease

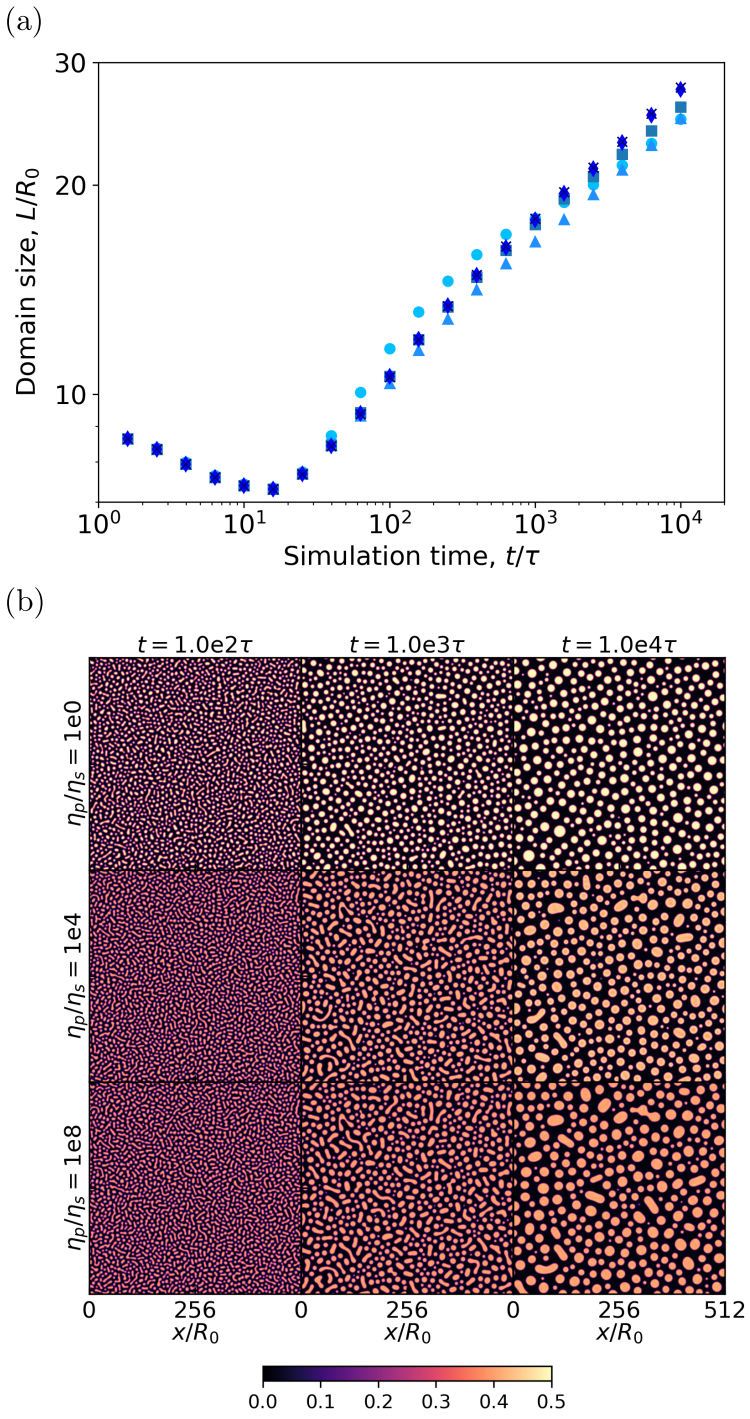

Figure 5.7: (a) Domain size growth by diffusion in Region B (ϕ_p^0=0.16, ϕ_n^0=0.64, ϕ_s^0=0.20) for different mobility contrasts: $\eta_p/\eta_s = 10^0$ (circles), 10^2 (triangles), 10^4 (squares), 10^6 (diamonds), and 10^8 (crosses). Darker symbols correspond to higher η_p/η_s. Corresponding microstructures for η_p/η_s= 10^0 (top row), 10^4 (middle row), and 10^8 (bottom row) are shown in (b), where the color bar represents ϕ_p.

in ϕ_p^α combined with the unchanged ϕ_p^β increases the fraction of the polymer-rich phase, f^α, as shown in Figure 5.8c. This increase in f^α due to the redistribution of polymer content is demonstated by a mass-balance equation often referred to as the "lever rule":

$$f^\alpha = \frac{\phi_p^0 - \phi_p^\beta}{\phi_p^\alpha - \phi_p^\beta}. \tag{5.20}$$

Holding all other variables the same, a decrease in ϕ_p^α leads to an increase in f^α. We refer to this result as the "lever effect" for the rest of this chapter. The increase in f^α results in stringier discrete domains which have an advantage in coarsening as shown in Figure 5.3. At $t/\tau = 10^3$, the shape metric for the morphologies in Figure 5.7 are $C = 1.05$, 1.31, and 1.34 for $\eta_p/\eta_s = 10^0$, 10^4, 10^8, respectively; the stringier domains for higher mobility contrasts in $t/\tau = 10^3$ lead to slightly larger domains in $t/\tau = 10^4$.

Mobility contrasts only introduced slight differences in the dynamics and morphology of an average composition in Region B as shown in Figure 5.7. However, this limited effect is not true for all average compositions in Region B. Figure 5.9 shows coarsening dynamics by diffusion for a near-symmetric average composition in Region B. When $\eta_p/\eta_s = 1$ (circles), morphology development follows diffusion-only coarsening as described for the blue curves in Figure 5.3. Although this average composition still lies inside Region B (polymer-rich clusters at equilibrium), applying a mobility contrast does slow down its coarsening. We attribute this effect to the inversion of the polymer-rich and polymer-poor domains as the continuous and discrete phases. This 'phase inversion' is easiest to see by comparing the microstructures at $t/\tau = 10^4$ in Figure 5.9b. Since the polymer-rich phase becomes continuous with mobility contrasts, bulk diffusion becomes reduced by a factor of η_p/η_s, similar to the structural arrest mechanism in Region A. However, since this average composition is near-symmetric, interfacial diffusion remains active in reshaping the stringy domains, explaining why domain coarsening at $\eta_p/\eta_s = 10^4$ still proceeds at

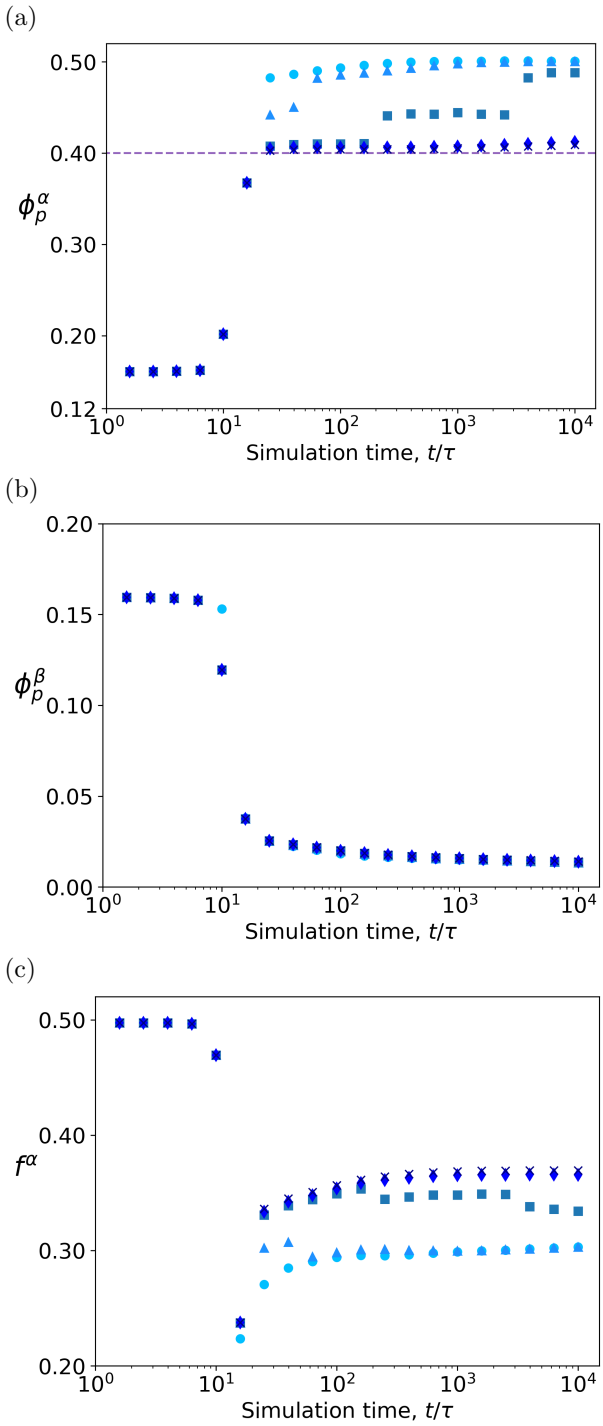

Figure 5.8: Polymer concentrations in (a) the polymer-rich α–phase, ϕ_p^α, and (b) the polymer-poor β–phase, ϕ_p^β and (c) the fraction of the polymer-rich α–phase, f^α, for (ϕ_p^0=0.16, ϕ_n^0=0.64, ϕ_s^0=0.20) with mobility contrasts: $\eta_p/\eta_s = 10^0$ (circles), 10^2 (triangles), 10^4 (squares), 10^6 (diamonds), and 10^8 (crosses). Darker symbols correspond to higher η_p/η_s. The dashed line in (a) marks the glass-transition concentration, ϕ_p^*.

the same rate as coarsening at $\eta_p/\eta_s = 10^8$. We expect that at longer simulation times, effects of higher mobility contrasts will manifest as discrete domains eventually become circular and interfacial diffusion becomes inactive as a coarsening mechanism.

The phase inversion shown in Figure 5.9 is simply another consequence of the lever effect. Figure 5.10 shows the dynamics of ϕ_p^α, ϕ_p^β, and f^α for the same data presented in Figure 5.9. Akin to the dynamics in Figure 5.8, a larger mobility contrast decreases ϕ_p^α which in turn increases f^α. In this case, however, the average composition is near-symmetric, allowing the lever effect to increase f^α from $f^\alpha < 0.5$ to $f^\alpha > 0.5$, leading to the inversion of the continuous majority phase from polymer-poor to polymer-rich.

As demonstrated by morphologies in Figures 5.6, 5.7 and 5.9, the significance of the lever effect is composition-dependent. In Region A (polymer-poor clusters in polymer-rich matrix), the lever effect pushes f^α farther away from symmetry, leading to smaller and more circular domains. In Region B (polymer-rich clusters in polymer-poor matrix), the lever effect pushes f^α closer to symmetry. For polymer-dilute average compositions, the lever effect makes discrete domains stringier, thus slightly increasing coarsening rates. On the other hand, near-symmetric average compositions experience a phase inversion that hinders coarsening. Average compositions that experience phase inversion is introduced as "Region C" in the ternary phase diagram shown in Figure 5.11. In this region, equilibrium morphologies belong to Region B, but transient morphologies belong to Region A. The boundaries of Region C are determined by both thermodynamics and the glass transition model. The top vertex of Region C corresponds with the tie-line of the shallowest quench whose polymer-rich concentration hits Region G. The schematic assumes near-horizontal tie-lines to conveniently demonstrate the point. The boundary between Regions A and C is the original equilibrium symmetry line between Regions A and B. The location of this line can be determined using Eq 5.20 by settting $f^\alpha = 0.5$. The boundary between Regions B and C is the dynamic symmetry line. For large enough

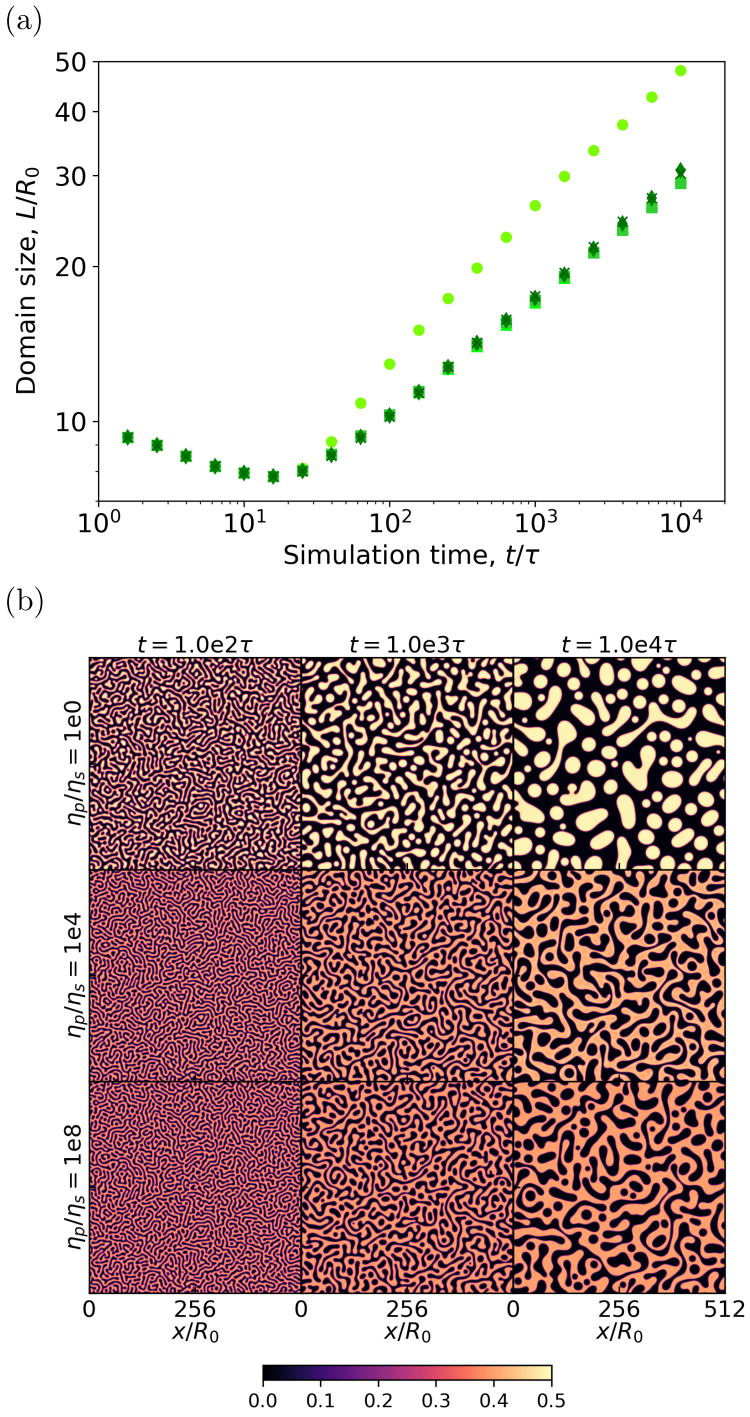

Figure 5.9: (a) Domain size growth by diffusion for a near-symmetric mixture in Region B (ϕ_p^0=0.22, ϕ_n^0=0.58, ϕ_s^0=0.20) for different mobility contrasts: $\eta_p/\eta_s = 10^0$ (circles), 10^2 (triangles), 10^4 (squares), 10^6 (diamonds), and 10^8 (crosses). Corresponding microstructures for $\eta_p/\eta_s = 10^0$ (top row), 10^4 (middle row), and 10^8 (bottom row) are shown in (b), where the color bar represents ϕ_p.

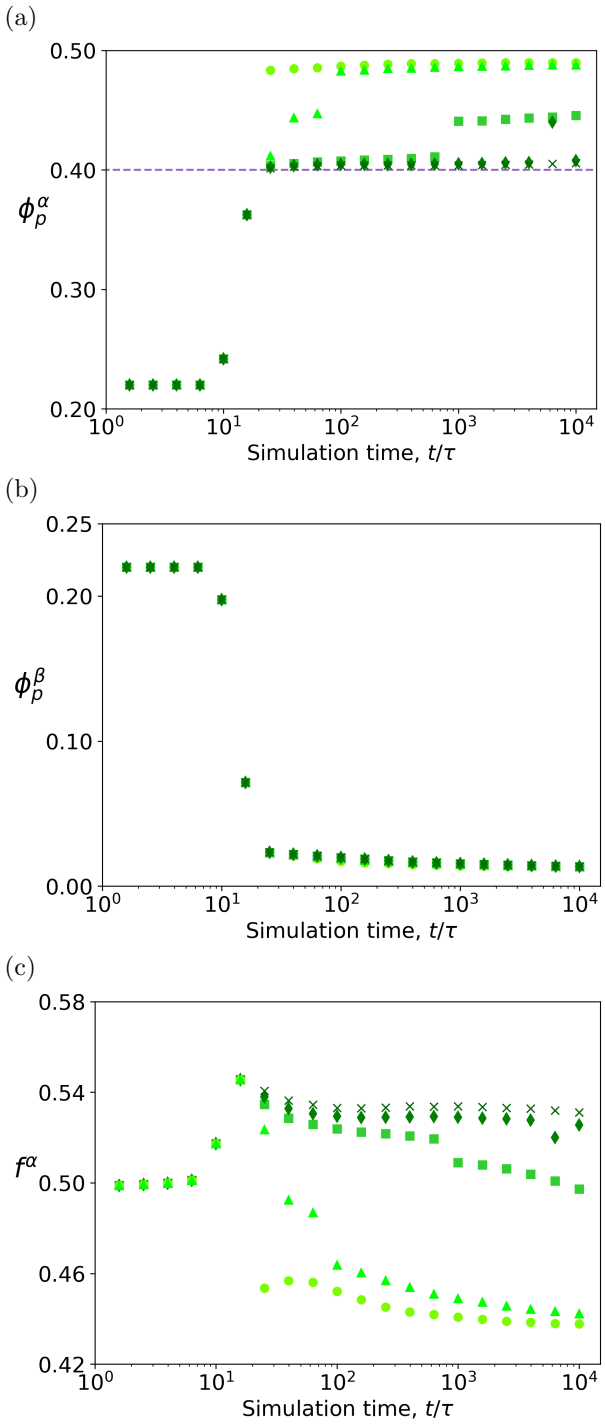

Figure 5.10: Polymer concentrations in (a) the polymer-rich α–phase and (b) the polymer-poor β–phase, and (c) the fraction of the polymer-rich α–phase for (ϕ_p^0=0.22, ϕ_n^0=0.58, ϕ_s^0=0.20) with mobility contrasts: $\eta_p/\eta_s = 10^0$ (circles), 10^2 (triangles), 10^4 (squares), 10^6 (diamonds), and 10^8 (crosses). Darker symbols correspond to higher η_p/η_s. The dashed line in (a) marks the glass-transition concentration, ϕ_p^*.

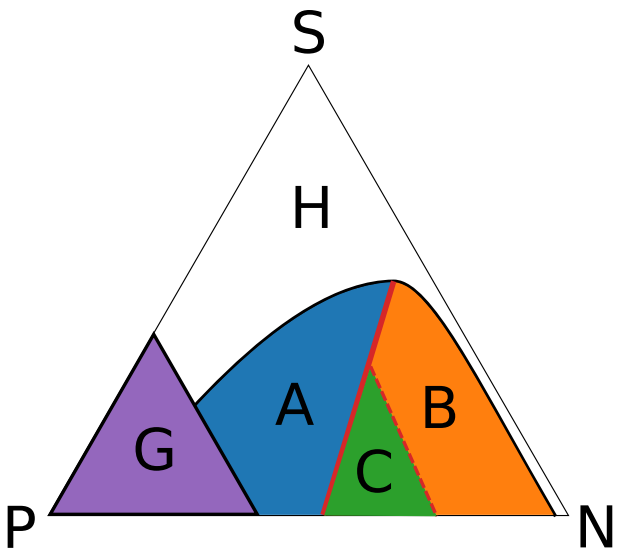

Figure 5.11: Representative ternary (polymer-solvent-nonsolvent) phase diagram with mobility contrast and the dynamic Region C, where morphologies immediately after phase separation belong in Region A (polymer-poor clusters in a polymer-rich matrix) while equilibrium morphologies belong in Region B (polymer-rich clusters in a polymer-poor matrix). The solid red line represents the static symmetry line while the dashed red line marks the dynamic symmetry line. Regions G and H are the glassy and homogeneous areas.

mobility contrasts, the location of this line can also be determined using Eq 5.20 by setting $f^{\alpha} = 0.5$, but at the same time subsituting ϕ_p^* for ϕ_p^{α}.

Our description of phase inversion due to the lever effect reflects Tanaka's description of the same phenomenon due to viscoelastic phase separation [66]. However, unlike simulations and experiments of viscoelastic phase separation, we have only shown phase inversion by comparing simulations from different levels of mobility contrast. Figure 5.12 shows that it is indeed possible to demonstrate dynamic phase inversion within one simulation by careful selection of parameters. As we can only practically simulate up to $t/\tau = 10^4$ due to computational limitations, we need to select a modest mobility contrast of $\eta_p/\eta_s = 10^2$ to enable the microstructure to relax back to its equilibrium morphology by the end of the simulation. We also set the average polymer composition, ϕ_p^0, and the glass transition concentration, ϕ_p^*, close to each other to allow phase inversion to manifest

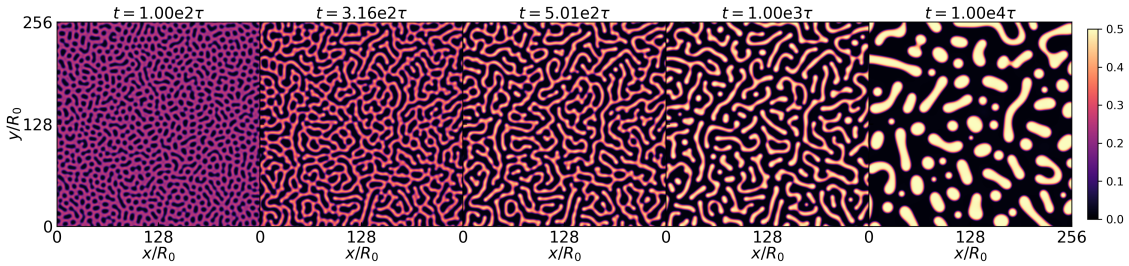

Figure 5.12: Dynamic phase inversion by diffusion in Region C due to the lever effect, where ($\phi_p^0 = 16$, $\phi_n^0 = 0.64$, $\phi_s^0 = 0.20$) and $\phi_p^* = 0.20$. The mobility contrast was set to $\eta_p/\eta_s = 10^2$. Point of inversion happens between the second and third frames. Note that the data shown here is only a quarter of a full periodic box. Color bar represents ϕ_p.

as clearly as possible. Although we have shown that phase inversion is achievable by the simple application of a mobility contrast in diffusion-only dynamics, we do not claim that other idiosyncrasies of viscoelastic phase separation can be reproduced by our simpler model.

5.8 Coarsening with hydrodynamics (Model H), with mobility and viscosity contrasts

In this section, we study the effects of mobility and viscosity contrasts (η_p/η_s) on microstructure evolution with hydrodynamics. For the rest of this section, we will refer to the combined effects of mobility and viscosity contrasts simply as a "viscosity contrast" for convenience. Akin to Section 5.7, we examine three different average compositions along a constant ϕ_s^0–axis: an average composition in Region A (polymer-poor clusters in a polymer-rich matrix), an average composition in Region B (polymer-rich clusters in a polymer-poor matrix), and an average composition in Region C, (transient morphologies in Region A but equilibrium morphologies in Region B). Simulation times in this section are limited to $t/\tau = 10^4$ due to practical restrictions of our computational tools. Viscosity

contrasts are also limited to $\eta_p/\eta_s = 10^4$, as solving the Stokes equation at higher levels of viscosity contrasts become computationally limiting.

Figure 5.13 shows domain size growth in Region A for different levels of viscosity contrasts. The circles ($\eta_p/\eta_s = 1$) in Figure 5.13 represent the same data shown by the orange pentagons in Figure 5.5, illustrating coarsening behavior for this average composition without viscosity contrasts. From this base case, we observe that increasing the viscosity contrast slows down coarsening; not only do the mobilities in the polymer-rich matrix get reduced by a factor of η_p/η_s as they were in Figure 5.6, capillary flows generated from stringy domains also get shut down quickly, as evidenced by comparing the velocity fields of $\eta_p/\eta_s = 1$ and $\eta_p/\eta_s = 10^4$ at $t/\tau = 10^2$. Thus, imposing a viscosity contrast of $\eta_p/\eta_s = 10^4$ leads to structural arrest in Region A within $t/\tau = 10^4$.

Figure 5.14 shows coarsening dynamics in Region B for different levels of viscosity contrasts. The circles ($\eta_p/\eta_s = 1$) in Figure 5.14 represent the same data shown by the blue triangles in Figure 5.5, illustrating coarsening behavior for this average composition without viscosity contrasts. Compared to this base case, we observe that increasing the viscosity contrast acccelerates coarsening. This counterintuitive result is again caused by the lever effect. In the absence of hydrodynamics for the same average composition, Figure 5.7 showed that domain sizes are slightly larger by $t/\tau = 10^4$ due to the stringer domains at earlier times. This same effect is magnified by hydrodynamics as shown in Figure 5.14c. Stronger capillary flows after phase separation ($t/\tau = 10^2$) lead to larger, stringier domains. Capillary flows eventually attenuate ($t/\tau = 10^3$) due to the applied viscosity contrast, but not before glass-like stringy domains have already been formed. These domains then continue to coarsen by bulk diffusion, interfacial diffusion, and domain coalescence. We expect that at some time beyond $t/\tau = 10^4$, the growth rate of the squares ($\eta_p/\eta_s = 10^4$) will slow down to the rate of the circles ($\eta_p/\eta_s = 1$) as domains become circular and bulk diffusion remains as the only active coarsening

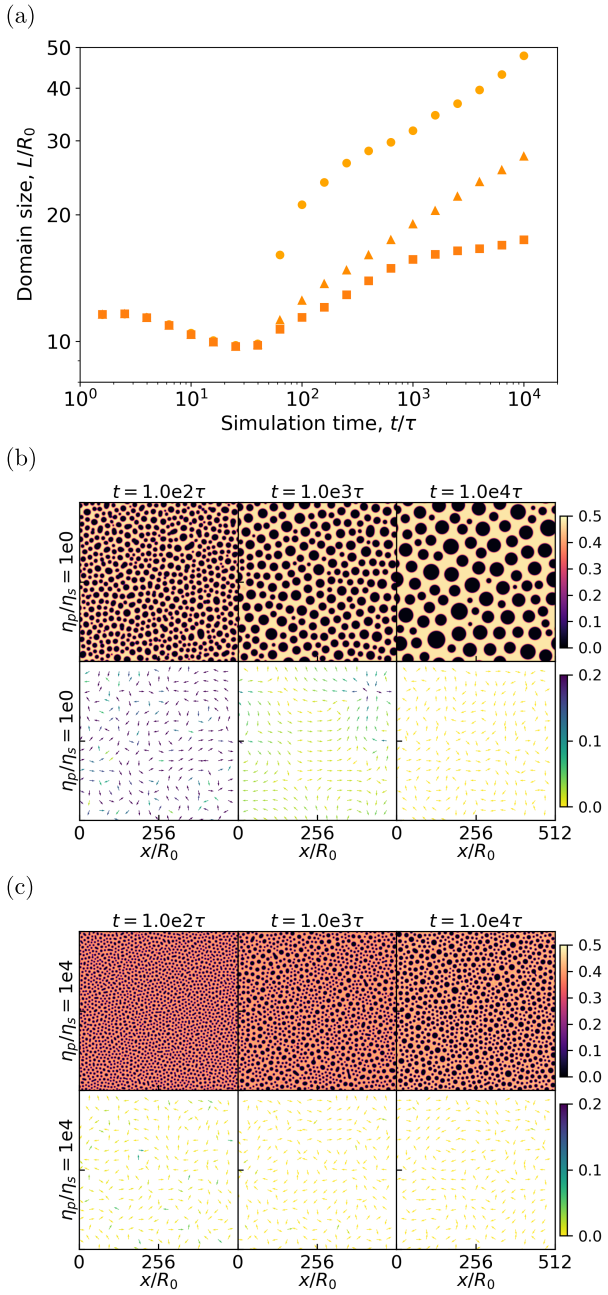

Figure 5.13: (a) Domain size growth by diffusion in Region A (ϕ_p^0=0.28, ϕ_n^0=0.52, ϕ_s^0=0.20) for different viscosity contrasts: $\eta_p/\eta_s = 10^0$ (circles), 10^2 (triangles), 10^4 (squares). Corresponding microstructures (top-row) and velocity fields (bottom-row) for (b) $\eta_p/\eta_s = 10^0$ and (c) $\eta_p/\eta_s = 10^4$. Density color bar represents ϕ_p. Unit vectors in the velocity fields show direction while their colors reflect their magnitude.

mechanism.

Figure 5.15 shows coarsening dynamics in Region C for different levels of viscosity contrasts. When $\eta_p/\eta_s = 1$, capillary flows accelerate domain growth and reshaping right after phase separation. When domains become circular, capillary flows shut down and coarsening proceeds only by bulk diffusion. Meanwhile, setting $\eta_p/\eta_s = 10^4$ induces phase inversion of the continuous phase to polymer-rich, thus slowing down diffusion and attenuating capillary flows. At some time beyond $t/\tau = 10^4$, we expect the enrichment of the polymer-rich phase to reach the equilibrium concentration, the discrete polymer-poor clusters to coarsen further, coalesce, and eventually become the continuous phase, the same qualitative morphology at $t/\tau = 10^4$ for the case without viscosity contrasts.

In the case of diffusion-only dynamics, we demonstrated dynamic phase inversion in Region C by imposing a modest mobility contrast ($\eta_p/\eta_s = 10^2$) relative to the maximum simulation time ($t/\tau = 10^4$). We applied a similar strategy in Figure 5.16 to illustrate dynamic phase inversion in Model H. However, the polymer-rich domains tend to stay continuous longer in the presence of hydrodynamics. The polymer-rich phase remains continuous even at $t/\tau = 10^4$, when ϕ_p^α has already relaxed to its equilibrium value; in fact, the fraction of the polymer-rich phase at this point is $f^\alpha = 0.19$, relatively far from symmetry. Of course, we expect the polymer-rich phase to eventually become discrete at some simulation time beyond $t/\tau = 10^4$. This simulation demonstrates that flow is an essential ingredient to the physics of phase-separating systems as it can introduce unforeseen complexities.

5.9 Conclusions

In this chapter, we explored the coarsening dynamics of Model B and Model H, and the corresponding effects of mobility and viscosity contrasts. In the absence of

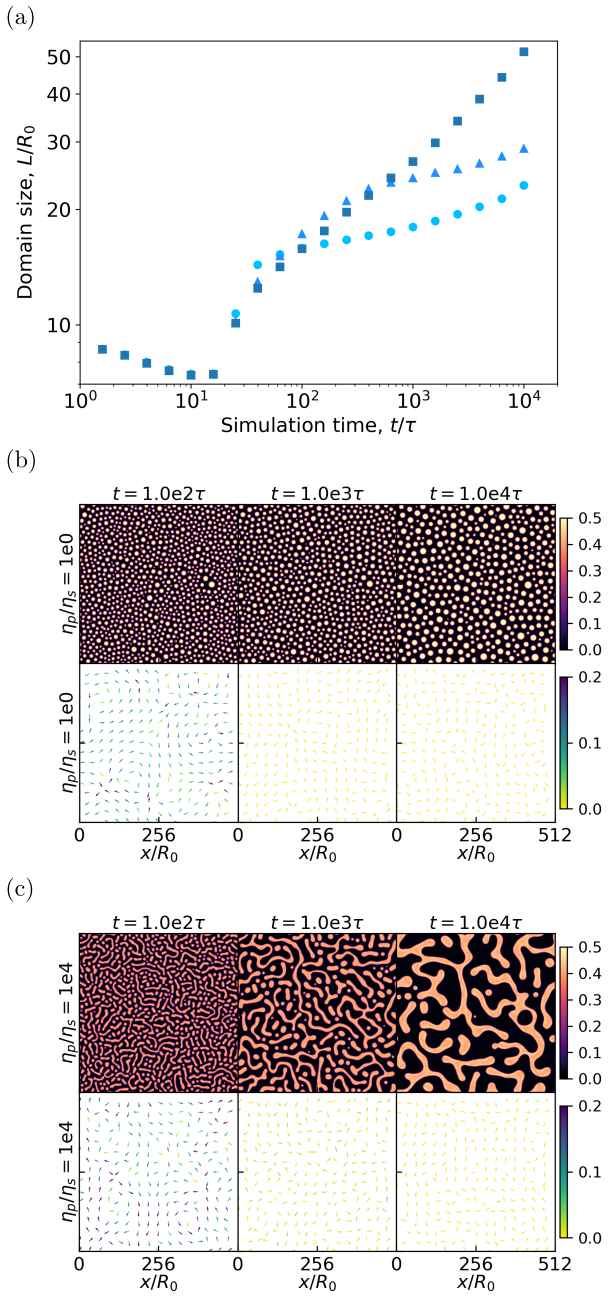

Figure 5.14: (a) Domain size growth by diffusion in Region B (ϕ_p^0=0.16, ϕ_n^0=0.64, ϕ_s^0=0.20) for different viscosity contrasts: $\eta_p/\eta_s = 10^0$ (circles), 10^2 (triangles), 10^4 (squares). Corresponding microstructures (top-row) and velocity fields (bottom-row) for (b) $\eta_p/\eta_s = 10^0$ and (c) $\eta_p/\eta_s = 10^4$. Density color bar represents ϕ_p. Unit vectors in the velocity fields show direction while their colors reflect their magnitudes.

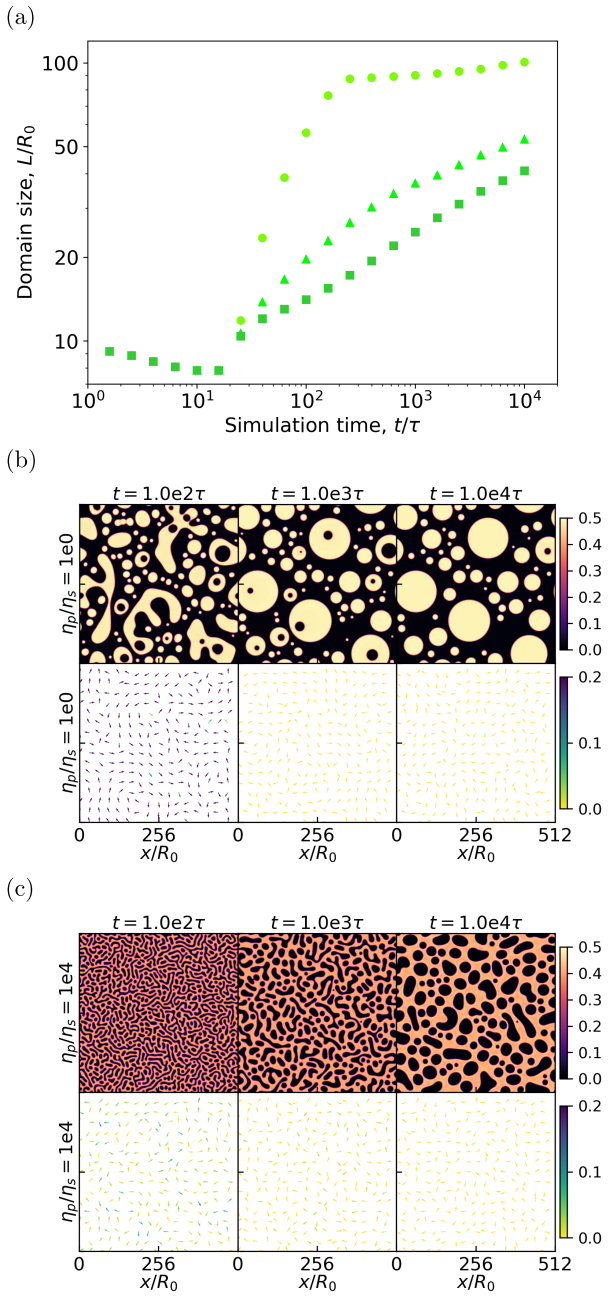

Figure 5.15: (a) Domain size growth by diffusion in Region C (ϕ_p^0=0.22, ϕ_n^0=0.58, ϕ_s^0=0.20) for different viscosity contrasts: $\eta_p/\eta_s = 10^0$ (circles), 10^2 (triangles), 10^4 (squares). Corresponding microstructures (top-row) and velocity fields (bottom-row) for (b) $\eta_p/\eta_s = 10^0$ and (c) $\eta_p/\eta_s = 10^4$. Density color bar represents ϕ_p. Unit vectors in the velocity fields show direction while their colors reflect their magnitudes.

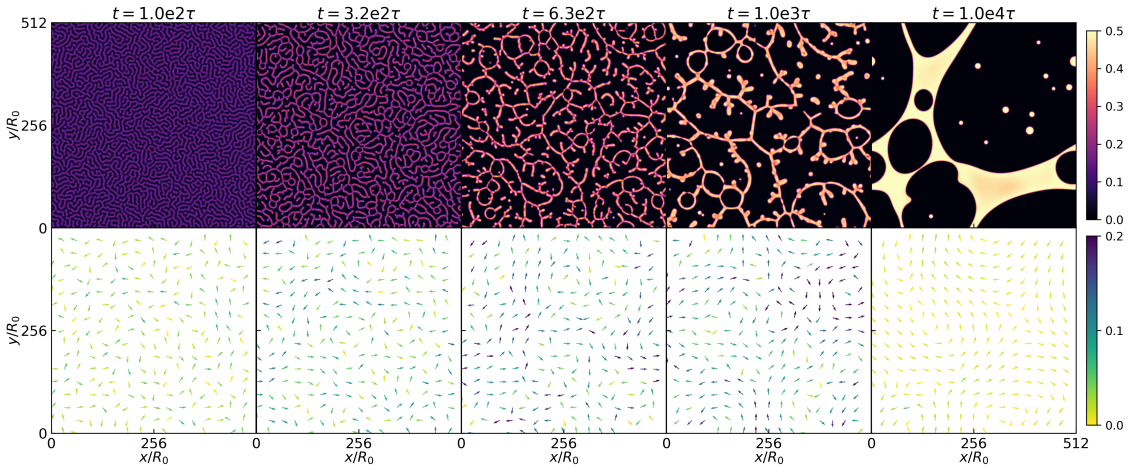

Figure 5.16: Microstructural evolution (top-row) with hydrodynamics in Region C where ($\phi_p^0 = 0.10$, $\phi_n^0 = 0.70$, $\phi_s^0 = 0.20$) and $\phi_p^* = 0.14$. The viscosity contrast was set to $\eta_p/\eta_s = 10^2$. Color bar represents ϕ_p. Velocity-field (bottom-row) unit vectors show direction while their colors reflect their magnitudes.

these contrasts, we demonstrated that coarsening behavior is concentration-dependent. Polymer-rich clusters grow slower than polymer-poor clusters due to the difference in diffusivities between a polymer and a small molecule. We also showed that shape plays a crucial role in determining the rate of domain growth. In Model B, we showed how interfacial diffusion becomes less significant once the discrete domains become circular. In Model H, capillary flows accelerate coarsening up to the point when discrete domains also become circular.

We showed that mobility and viscosity contrasts are effective in mimicking structural arrest for specific average compositions. However, these contrasts can also lead to many unexpected consequences. For specific compositions, we demonstrated how the lever effect increases the fraction of the polymer-rich phase that then changes domain shape and coarsening rates. The lever effect can even cause an inversion of the polymer-rich and polymer-poor domains as the minority and majority phases for near-symmetric mixtures. This inversion not only changes morphology, but it also changes coarsening dynamics.

Chapter 6

Conclusions and outlook

6.1 Conclusions

We modeled and studied membrane formation in nonsolvent-induced phase separation (NIPS) by phase-field simulations. In Chapter 3, we demonstrated that mass-transfer-driven spinodal decomposition, thermal fluctuations, and structural arrest are essential and sufficient to the formation of asymmetric membrane microstructures. Specifically, the competition between the propagation of the phase-separation and glass-transition fronts determines the pore-size distribution of the membrane. In Chapter 4, we explored how these membrane formation mechanisms change with the glass-transition concentration, ϕ_p^*, and the dope composition, two important parameters in the formulation of NIPS systems. We found that if ϕ_p^* and the dope composition are either too close or too far from each other, NIPS will lead to a membrane with a homogeneous pore-size distribution; the distance between ϕ_p^* and the dope composition must be just right to get asymmetric morphologies.

To reduce complexity, the NIPS simulations in Chapters 3 and 4 were restricted to diffusion-only transport, neglecting potential effects from hydrodynamics. In Chapter 5,

we compared bulk phase separation by diffusion and with hydrodynamics. We found that in general, hydrodynamics accelerates coarsening, but their effects attenuate as the capillary flows diminish with increased circularity of the discrete domains. In the presence of a glass transition (implemented as a mobility and viscosity contrast between the polymer-rich and polymer-poor phases), coarsening behavior significantly depends on the average composition. For morphologies with continuous polymer-rich domains, the glass transition serves as an effective structural arrest mechanism. For morphologies with discrete polymer-rich domains, the glass transition changes the transient concentration of the polymer-rich phase, thus leading to a change in shape of the discrete domains. We refer to this phenomenon as the "the lever effect," and it introduces several complexities to the coarsening process, including phase inversion that is normally attributed to viscoelastic phase separation[66].

The studies within this dissertation contributes to our fundamental understanding of membrane formation. Nevertheless, many more mysteries remain in membrane science, and several of them can be tackled with additional features to the same computational tools used herein. The following section outlines these ideas for the ambitious researcher of the future.

6.2 Outlook

6.2.1 Chemical additives

Casting solutions in industry contain additives to modify membrane properties. Several decades of heuristic development has led to complex casting solutions. Industrial formulations are highly guarded secrets; however, certain guidelines are openly known in literature. For example, acetone and tetrahydrofuran are often added to make membranes

more dense—conversely, salts such as zinc chloride are used to make membranes more porous [6]. Surfactants can also be added to control the formation of macrovoids[67]. Additives can also be included for mechanical strength and control of the casting solution's viscosity.

Polymers can also serve as chemical additives: amphiphilic block copolymers—containing hydrophilic and hydrophobic blocks—can be added to improve a membrane's resistance to fouling[68, 69, 70]. During the film's immersion in water (the nonsolvent), the hydrophobic blocks mix with the polymer-rich phase while the hydrophilic blocks mix with the polymer-lean phase. After drying, the hydrophobic blocks integrate into the membrane matrix while the hydrophilic blocks partially cover the pores and the membrane surface. These hydrophilic segments disrupt the hydrophobic interactions between the membrane material and the foulants, discouraging their adhesion to the surface.

Pursuing this project using our in-house phase-field software would require thermodynamic characterization of the four-component system. In the case of the amphiphilic block copolymer, derivation of the appropriate free energy functional is required.

6.2.2 VIPS and Solvent evaporation

Vapor-induced phase separation (VIPS) forms membranes by absorption of the nonsolvent from the vapor phase. Venault et al. [68] showed that VIPS membranes with amphiphilic polymer additives exhibit better anti-fouling properties than NIPS membranes made with the same formulation. VIPS is also often combined with NIPS in the fabrication of hollow fiber membranes[71, 72] as discussed in Section 6.2.5.

Solvent evaporation is the opposite of VIPS—phase separation is induced by loss of solvent to the atmosphere. However, just like VIPS, evaporation is often combined with NIPS: for example, evaporation before nonsolvent immersion is vital to getting defect-

free skin layers in gas permeation membranes[73]. Solvent evaporation can also play a role in the fabrication of hollow fiber membranes as discussed in Section 6.2.5.

6.2.3 Viscoelasticity

Tanaka proposed that membrane morphologies are generated from viscoelastic phase separation[66]. Although we were able to simulate the formation of asymmetric membranes and phase inversion without elastic effects, many membrane features, such as macrvoids, remain unexplained. Inclusion of elastic effects would allow us to explore if they do play a role in the formation of these other membrane features.

Viscoelasticity may also prove essential to membranes subjected to external stresses during formation. As discussed in Section 6.2.5, modelling the formation of hollow fiber membranes will most likely require the incorporation of viscoelasticity[72]. Viscoelasticity may also play a role in the formation of dense skin layers of gas separation membranes[73]. These effects are hard to observe experimentally and numerical simulation is the most straightforward way to test hypotheses regarding the importance of viscoelasticity.

6.2.4 Combining self-assembly and NIPS (SNIPS)

Due to their unique properties, block copolymer applications in membranes are ubiquitous: drug delivery, charge-mosaic membranes, and gas permeation are just a few [74, 75]. A novel fabrication technique that combines block copolymer self-assembly and NIPS (SNIPS)—invented in 2007 by Peinemann and co-workers[76]—allows the fabrication of asymmetric membranes with regularly sized cylindrical pores in the separation layer. The narrow pore size distribution improves membrane selectivity, essential for sensitive separations such as the removal of pathogens from drinking water.

A block copolymer is first chosen as membrane material. The block copolymer is then

dissolved in a mixture of two solvents, one being more volatile than the other. The film is allowed to dry after casting the solution. As the volatile solvent leaves, block copolymers near the surface of the film form cylinders. These cylinders form from the surface down because evaporation drives the composition change leading to the self-assembly. These cylindrical pores are regularly spaced and exhibit small size variance due to microphase separation. Following the standard NIPS procedure, the membrane is then immersed in a nonsolvent bath. The immersion precipitates the rest of the film, allowing it to form a microporous support below the uniform cylindrical pores. There have only been a handful of experimental studies [76, 77, 78, 79, 80, 81] done to explore the parameter space of this process—and no theoretical studies to explain the physics in detail. The limited literature on SNIPS is a combined result of its novelty and complexity, making this field an exciting area to study.

6.2.5 Hollow fiber membranes

In Chapters 3 and 4, we simulated the formation of flat-sheet membranes. In reality, many industrial membreanes are made as hollow fibers. Hollow fiber membranes maximize separation area per volume, leading to very compact modules [6]. Hollow fibers also have better self-mechanical support and are easier to handle during processing and installation [72].

Fabrication of hollow fibers involves several steps. The dope and bore fluid (nonsolvent) are fed into a spinneret. Internal coagulation begins as soon as the dope and bore fluid meet upon exiting the spinneret. As the two jets travel through the air-gap region, phase separation on the external surface is induced by evaporation of solvent and absorption of nonsolvent from the atmosphere. The hollow fibers are then completely solidified upon immersion in the nonsolvent bath.

We can break down the process above to the relevant physical phenomena. The internal coagulation after the spinneret is similar to NIPS; however, the effects of the dope and bore solution's relative velocities need to be considered. In practice, it is known that their relative velocities govern the thickness of the selective layer [6], suggesting that shear flow modifies the NIPS process. Meanwhile, VIPS and solvent evaporation govern the phase separation on the outer surface—again in the presence of flow. Also note that the nascent fibers headed towards the nonsolvent bath are subjected to elongational stresses due to their own weight and the force required to pull them for collection; thus, viscoelasticity needs to be included into any model of the process for it to be useful [72].

Appendix A

Membranes from the Lab

A.1 Membrane Preparation and Characterization

The scanning electron micrographs (SEM images) showed in Figure 1.1 were prepared and characterized in Asahi Kasei, Fuji City, Japan. A dope solution was prepared with 24.79 g of polysulfone, 63.73 g of N,N-dimethylacetamide (DMAc), and 9.43 g of 2-propanol, equivalent to a polymer-nonsolvent-solvent system with dope volume fractions, ($\phi_p = 0.20, \phi_n = 0.68, \phi_s = 0.12$). The solution was mixed in a 50 °C water bath for 6 hours and stirred overnight in room temperature. The dope solution film was cast on a polycarbonate substrate in a glove box with 11% relative humidity. The cast film was immersed in a bath of 2-propanol to make asymmetric membranes (Figure 1.1b). On the other hand, the cast film that produced the symmetric membrane (Figure 1.1a) was left to coagulate in open air for 30 minutes, *i.e.,* the asymmetric membranes were made by NIPS while the symmetric membranes were prepared by VIPS. The films were then dried overnight in room atmosphere. Membrane samples were prepared for analysis by scanning electron microscopy (Hitachi SEM S-4700) by fracturing them in liquid nitrogen, staging them with carbon paste, and coating the fracture site with 4 nm of Osmium.

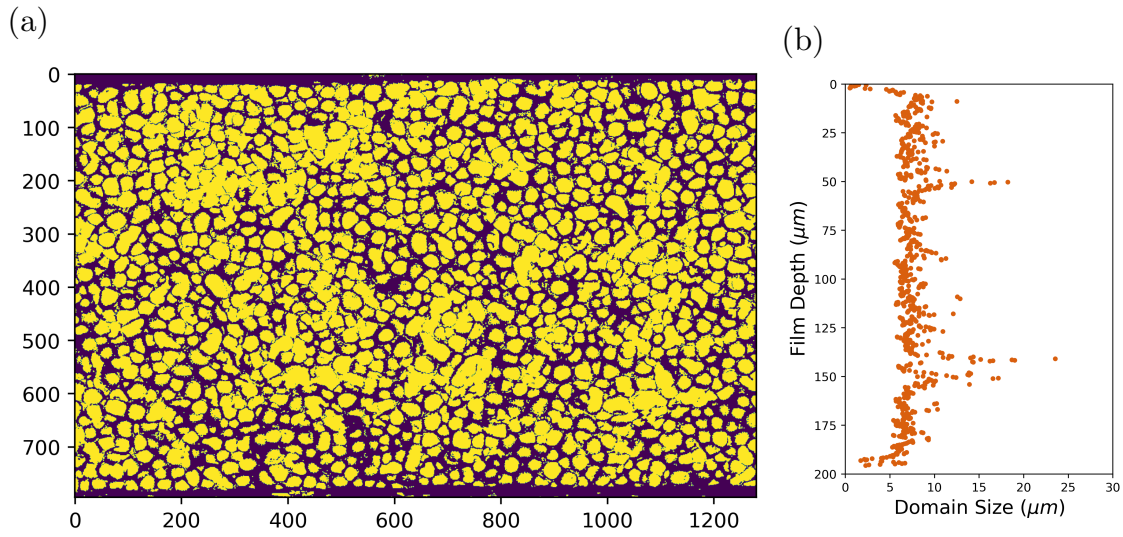

Figure A.1: Image analysis of the SEM image in Figure 1.1a. (a) A binary image is produced by applying a threshold to the SEM image. (b) Domain analysis of the processed image quantifies pore-size distribution along the membrane cross-section.

A.2 Image Analysis of Experimental Microstructures

We developed an image analysis script to extract quantitative pore-size distribution from SEM images. We used available computational tools from the open-source package, `OpenCV`[82]. Figure A.1 shows the analysis for the symmetric microstructure in Figure 1.1a. Similarly, Figure A.2 shows the analysis for the asymmetric microstructure in Figure 1.1b. The slopes for the best-fit lines in Figures A.1b and A.2b are -3.4×10^{-4} and 6.7×10^{-2}, respectively, in dimensionless units of domain-size per film-depth.

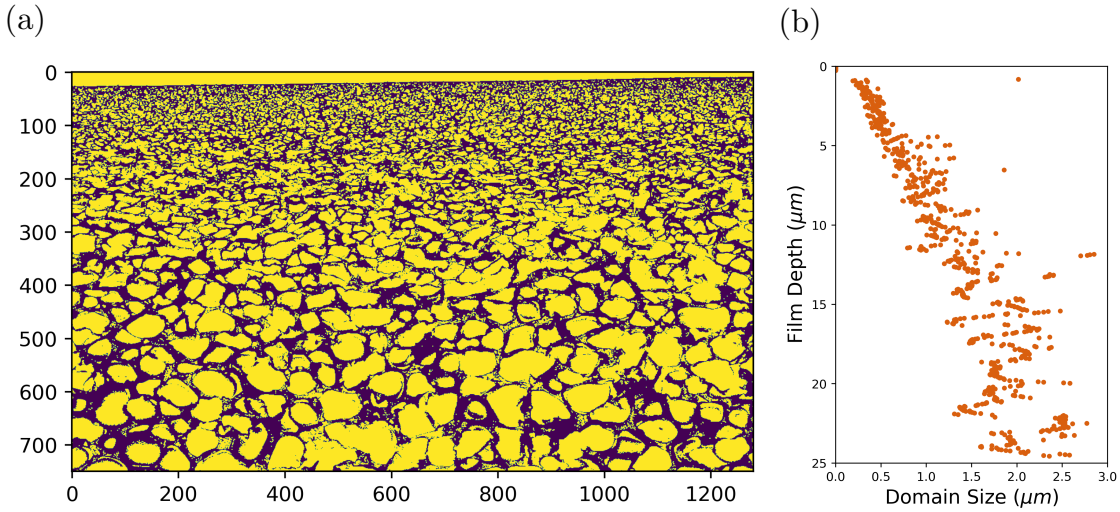

Figure A.2: Image analysis of the SEM image in Figure 1.1b. (a) A binary image is produced by applying a threshold to the SEM image. (b) Domain analysis of the processed image quantifies pore-size distribution along the membrane cross-section.

Appendix B

NIPS Simulation Details

B.1 NIPS simulation setup

In 2D, we set a simulation box of size, $512R_0 \times 2048R_0$ as shown in Figure B.1. As we use Fourier transforms to calculate the spatial derivatives, we set periodic boundary conditions on all sides of the simulation box. To establish no-flux boundary conditions at the bottom of the film and at the top of the bath, we initialize the concentrations to be symmetric across the midpoint, $y = 1024$. For each vertical half of the simulation box, we set the inner half as the initial film and the outer half as the nonsolvent bath. In the main manuscript, we showed only the domains corresponding to the film at the top-half of the simulation box. Pore-size profiling was also limited to the shown domain. Though we set the initial film composition to be symmetric along the y-axis, we did not symmetrize the thermal fluctuations, resulting in the microstructures for the two halves to not be identical, and in fact, they constitute independent statistical realizations of the film and bath dynamics. Nevertheless, the no-flux boundary conditions at the bottom of the film and at the top of the bath are satisfied, as shown in Figure B.1. We use the same setup in 3D with a total simulation box size of $64R_0 \times 512R_0 \times 64R_0$. We

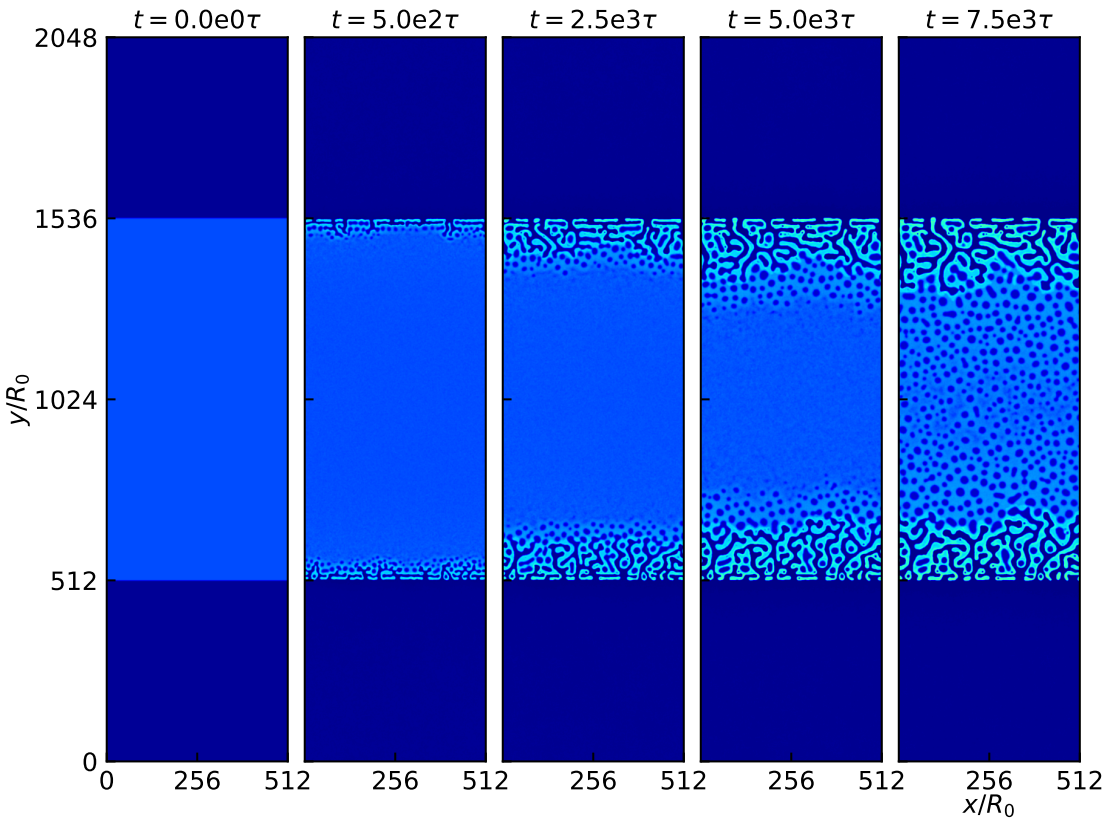

Figure B.1: NIPS simulations in 2D, showing the entire simulation box, with glass transition effects ($\eta_p/\eta_s = 10^4$) for the initial film composition of ($\phi_p = 0.20, \phi_n = 0.45$), corresponding to the green triangle in Figure 3.1. Polymer-rich regions are light green and polymer-poor regions are dark blue, ϕ_p color bar included in Figure 3.2.

used a pseudo-spectral method with semi-implicit time-stepping to solve Eq 3.1. Spatial discretization is set uniformly in each dimension as one discretization point per unit length, R_0, *e.g.*, $L_x/N_x = R_0$, $L_y/N_y = R_0$ for 2D simulations. We used constant time-stepping with $\Delta t = 0.001$ and $\alpha = 0.04$. Simulations were carried out using our custom phase-field software. Our methods paper[33] includes more details of the requisite numerical techniques.

B.2 Pore-size Profile Characterization

We calculate the polymer structure factor for each lateral slice of the film: for 2D simulations, these are structure factors of 1D slices along the y-axis; for 3D simulations, the computed structure factors are 2D slices along the y-axis,

$$S_p(\boldsymbol{q}, y) = \frac{1}{V} \sum_{\boldsymbol{r}} \sum_{\boldsymbol{r'}} e^{-i\boldsymbol{q}\cdot\boldsymbol{r}} \left[\phi_p(\boldsymbol{r}+\boldsymbol{r'}, y)\phi_p(\boldsymbol{r'}, y) - \langle\phi_p\rangle^2\right] \tag{B.1}$$

where V is the number of lattice points for that specific y-slice, and $\boldsymbol{r}$, $\boldsymbol{r'}$, and $\boldsymbol{q}$ are vectors in the $x-z$ plane. The second moment of $S_p(\boldsymbol{q}, y)$ for each y-slice,

$$\left\langle q^2(y)\right\rangle = \frac{\sum\limits_{\boldsymbol{q}} (\boldsymbol{q}\cdot\boldsymbol{q}) S_p(\boldsymbol{q}, y)}{\sum\limits_{\boldsymbol{q}} S_p(\boldsymbol{q}, y)}, \tag{B.2}$$

is used to estimate the characteristic domain size, L, by means of

$$L(y) = \frac{2\pi}{\left\langle q^2(y)\right\rangle^{1/2}}. \tag{B.3}$$

The approach described above is more robust than the traditional method of calculating $\langle q\rangle$ from the 1D histogram of the n-dimensional structure factor $S_p(\boldsymbol{q})$. The calculated value of L using the traditional method is highly sensitive to the number of

bins used for the histogram, especially in simulations where the number of lattice points per slice is limited.

B.3 Porosity Profile Characterization

Figure B.2 shows the porosity profiles of the 3D membranes shown in Figures 3.5 and 3.6. To calculate porosity, a threshold was applied to the density fields to make them binary. We set the threshold arbitrarily to $\phi_p^{thresh} = 0.90\phi_p^*$, *i.e.,* any domain where $\phi_p < \phi_p^{thresh}$ was considered "porous." Porosity was then calculated as the fraction of porous domains. Using this metric, the entire film starts as completely porous as nothing hinders the entry of nonsolvent. As NIPS proceeds, the polymer-rich membrane matrix forms, reducing film porosity. Porosity itself is distinct from pore size; two cross-sections can have the same porosity but exhibit different characteristic pore sizes. Note that we hold more confidence in our pore size analysis than our porosity calculations; we found that porosity is relatively sensitive to the value of ϕ_p^{thresh}, especially for the limited lateral dimensions of our simulations.

B.4 Selecting the mobility contrast η_p/η_s

As discussed in the main manuscript, we model the viscosity as a sigmoidal function of the local polymer volume fraction, $\phi_p(\boldsymbol{r})$:

$$\eta = 1 + \frac{\eta_p/\eta_s - 1}{1 + \exp\left(-\frac{1}{w}\left(\phi_p(\boldsymbol{r}) - \phi_p^*\right)\right)} \tag{B.4}$$

where w is the width of the sigmoid, ϕ_p^* is the glass-transition concentration, and η_p/η_s is the effective contrast in local mobilities between the glassy and non-glassy regions. The

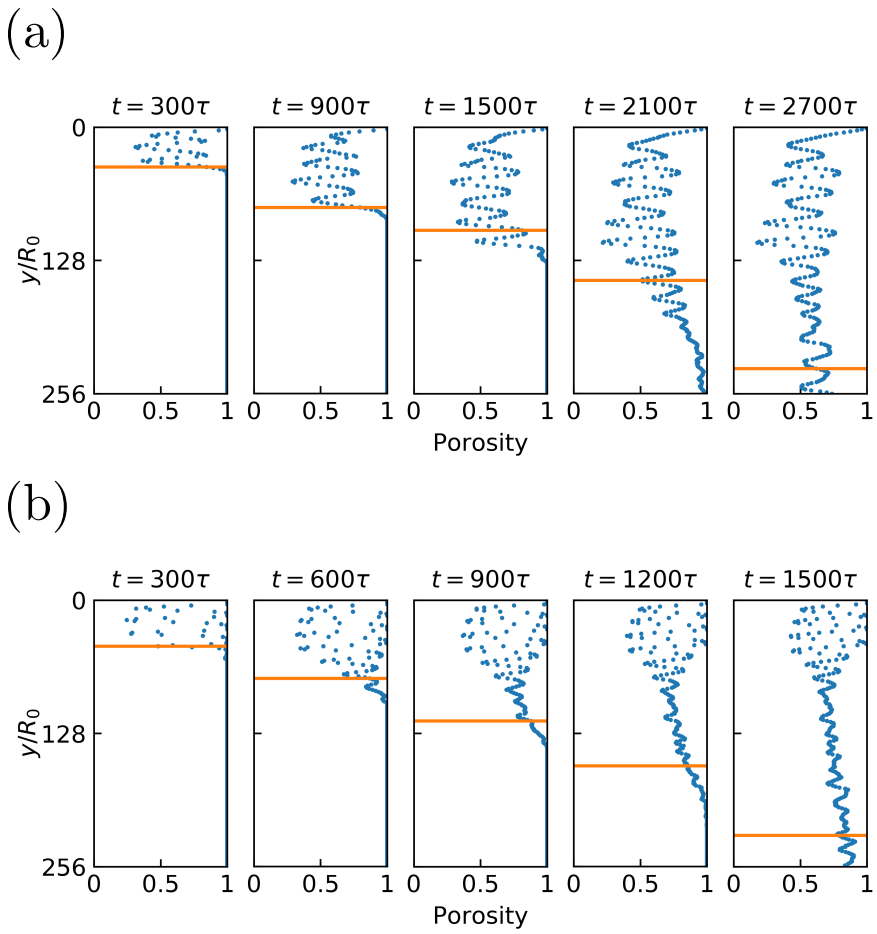

Figure B.2: Porosity profiles for the 3D NIPS simulations shown in (a) Figure 3.5 and (b) Figure 3.6. The orange line represents the glass-transition front.

sigmoidal model mimics the exponential growth in the viscosity of polymer solutions as predicted by the well-known Vogel-Fulcher-Tamman-Hesse (VFTH) and Williams-Landel-Ferry (WLF) equations[42] while bounding the maximum η for computational stability. We need to set η_p/η_s high enough that the sigmoidal model faithfully represents a physical glass transition. On the other hand, we cannot choose an exceedingly high value for η_p/η_s as it will slow down microstructure evolution excessively such that we cannot observe physically meaningful dynamics in accessible simulation times.

Figure B.3 shows a bulk spinodal quench in 1D for different values of η_p/η_s. At

$t = 15.8$, the concentrations are practically identical. However, by $t = 10^2$, the polymer-rich phase concentration for $\eta_p/\eta_s = 1$ has reached equilibrium, crossing the glass transition, ϕ_p^* on the way. We expect this behavior since setting $\eta_p/\eta_s = 1$ disables the glass transition. Meanwhile, the polymer-rich phase concentrations for $\eta_p/\eta_s = 10^4$ and $\eta_p/\eta_s = 10^6$ are approaching ϕ_p^* but have not crossed its value, as expected of a physical glass transition. However, by $t = 10^3$, the polymer-rich phase concentration for $\eta_p/\eta_s = 10^4$ has crossed ϕ_p^*, and the polymer-rich phase becomes even more enriched by $t = 10^4$, although it has still not reached the equilibrium value. On the other hand, the polymer-rich phase concentration for $\eta_p/\eta_s = 10^6$ barely crossed ϕ_p^* even by $t = 10^4$.

Based on Figure B.3, setting $\eta_p/\eta_s = 10^6$ would be preferred. In fact, some experimental studies of membrane formation characterize a gel as a fluid with viscosity, 10^6 centipoise[83, 84]. However, we see that the polymer-rich phase concentration crossing ϕ_p^* does not qualitatively change the coarse features of the NIPS microstructures shown in Figures 3.3 and 3.4. Choosing $\eta_p/\eta_s = 10^6$ leads to sharper interfaces for the finger-like structures shown in Figure 3.3 but doing so significantly slows down microstructure evolution. Meanwhile, we observe no large-scale morphological differences between the two levels of viscosity contrast in Figure 3.4. Thus, we choose to set $\eta_p/\eta_s = 10^4$, trading fine microstructural features for faster microstructure evolution for at least one film composition in 2D.

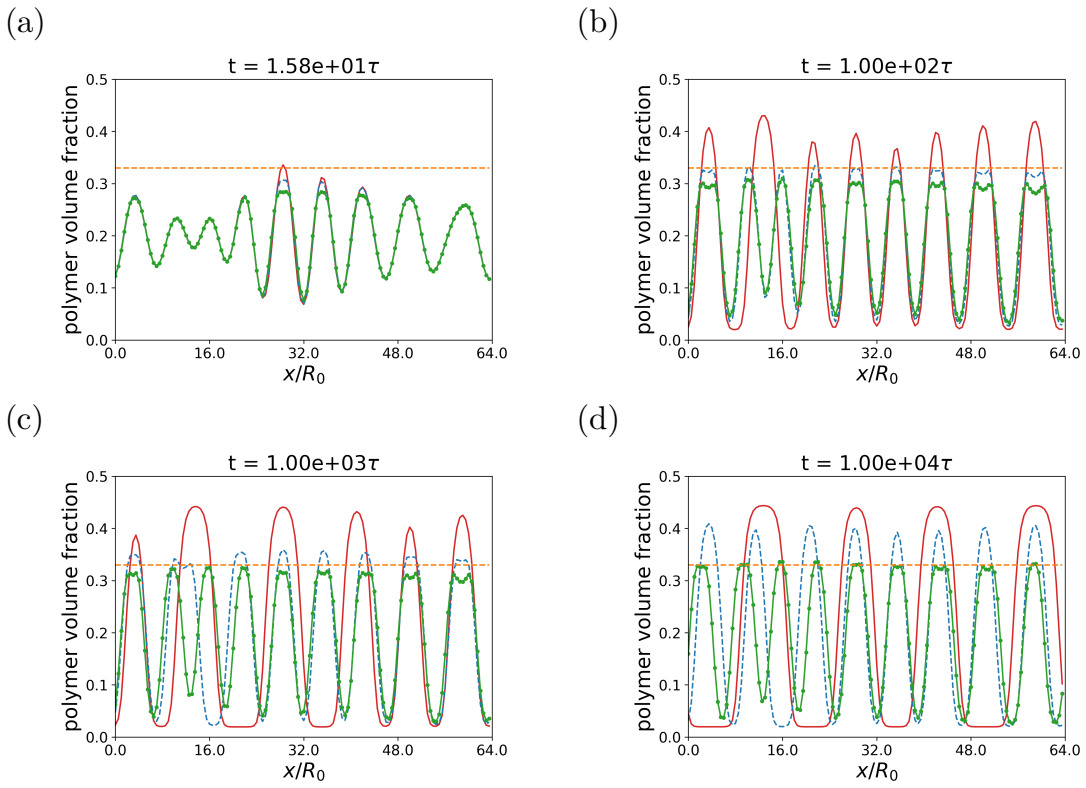

Figure B.3: Spinodal quench ($\phi_p = 0.20, \phi_n = 0.45$) in 1D using the same thermodynamic parameters in this study for simulations of different mobility contrasts: $\eta_p/\eta_s = 10^0$ (solid red line), $\eta_p/\eta_s = 10^4$ (dashed blue line), $\eta_p/\eta_s = 10^6$ (dotted green line). The dashed orange line marks the glass transition concentration, ϕ_p^*. Different panels correspond to different simulation times, (a) $t = 15.8$, (b) $t = 10^2$, (c) $t = 10^3$, (d) $t = 10^4$.

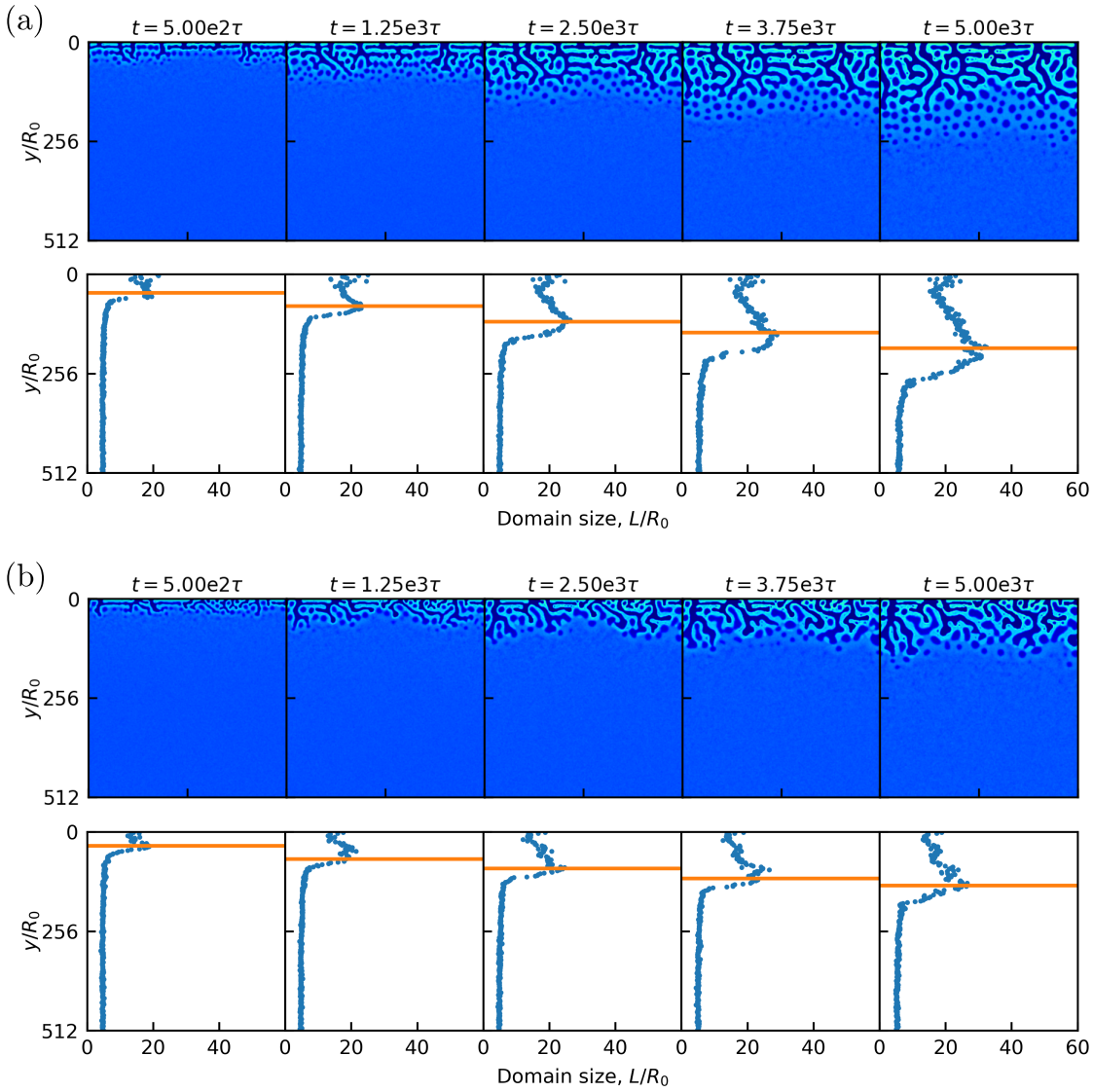

Figure B.4: NIPS simulations in 2D and their domain size profiles for the initial film composition of $(\phi_p = 0.20, \phi_n = 0.45)$, corresponding to the green triangle in Figure 3.1. Mobility contrasts set at (a) $\eta_p/\eta_s = 10^4$, (b) $\eta_p/\eta_s = 10^6$. Each density plot shown is $512R_0 \times 512R_0$. The y-coordinate corresponds to film depth, where $y = 0$ is the film-bath interface and $y = 512$ is the bottom of the film. Polymer-rich regions are light green and polymer-poor regions are dark blue, ϕ_p color bar included in Figure 3.2. The orange line (glass-transition front) in the domain size profile corresponds to the deepest point in the film where at least one grid point has crossed the glass transition concentration, ϕ_p^*.

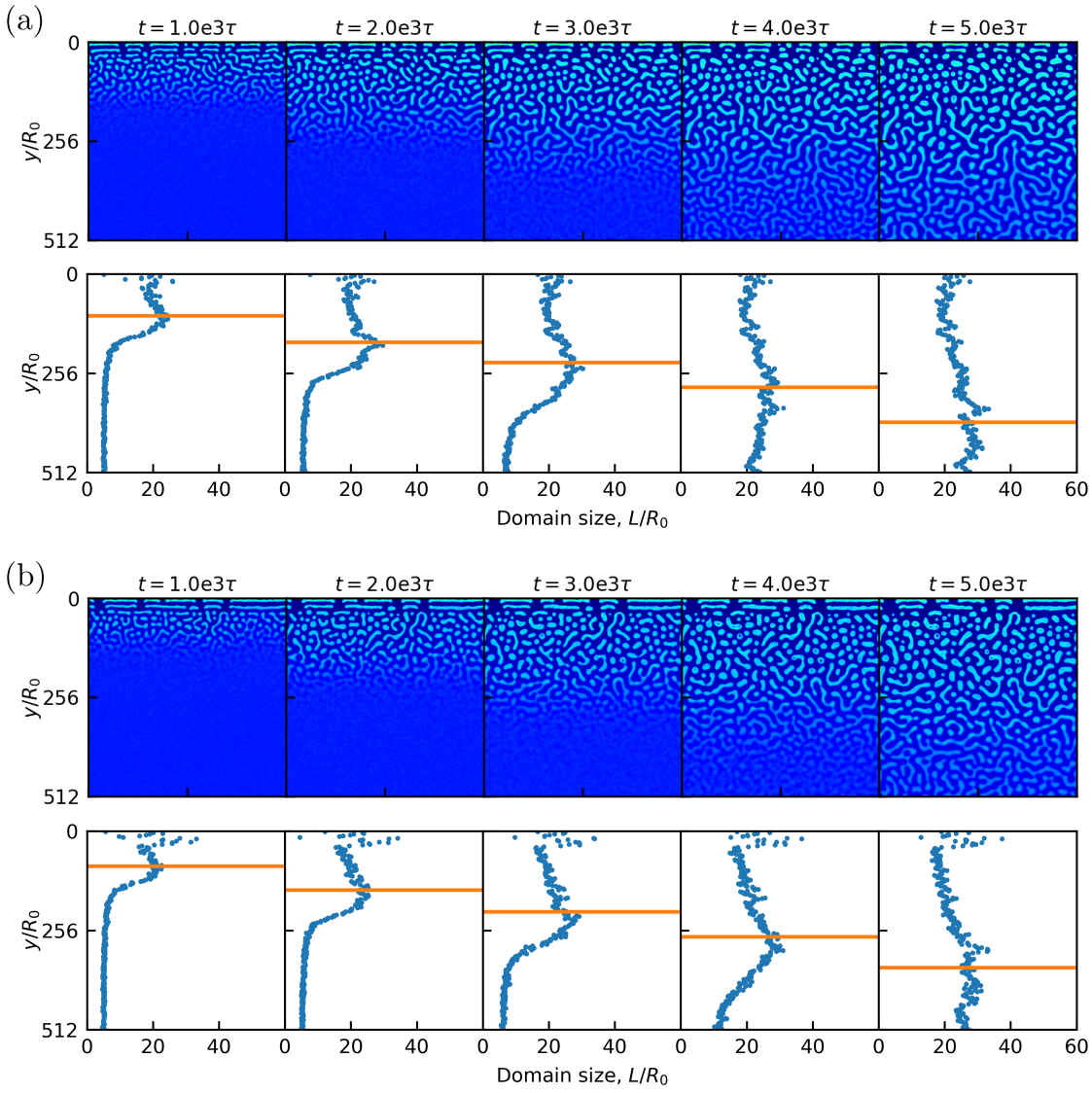

Figure B.5: NIPS simulations in 2D and their domain size profiles for the initial film composition of $(\phi_p = 0.15, \phi_n = 0.50)$, corresponding to the green square in Figure 3.1. Mobility contrasts set at (a) $\eta_p/\eta_s = 10^4$, (b) $\eta_p/\eta_s = 10^6$. Each density plot shown is $512R_0 \times 512R_0$. The y-coordinate corresponds to film depth, where $y = 0$ is the film-bath interface and $y = 512$ is the bottom of the film. Polymer-rich regions are light green and polymer-poor regions are dark blue, ϕ_p color bar included in Figure 3.2. The orange line (glass-transition front) in the domain size profile corresponds to the deepest point in the film where at least one grid point has crossed the glass transition concentration, ϕ_p^*.

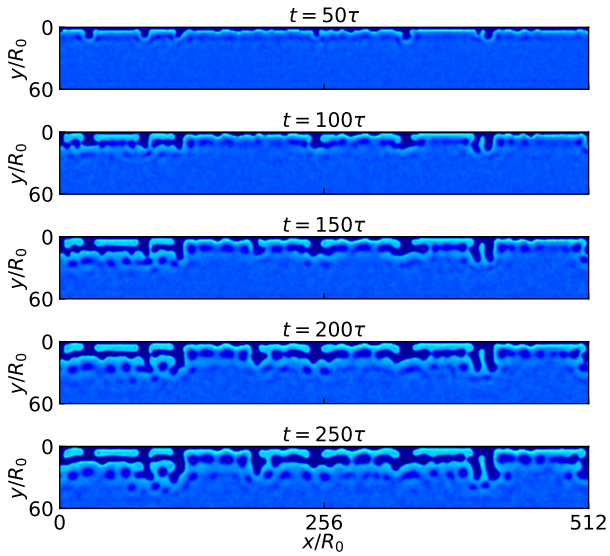

Figure B.6: Formation of finger-like structures at early times in 2D corresponding to the simulation in Figure 3.3b. Polymer-rich regions are light green and polymer-poor regions are dark blue, ϕ_p color bar included in Figure 3.2.

B.5 Formation of the finger-like structures in 2D

We include a close-up view of the formation of the finger-like structures at early times in Figure B.6. These images come from the same simulation as Figure 3.3b.

B.6 Vogel-Fulcher-Tamman-Hesse Viscosity Model

In addition to the phenomenological sigmoidal model used in Chapters 3,4, and 5, we also explored using a Vogel-Fulcher-Tamman-Hesse (VFTH) relationship between the local mixture viscosity, η, and the local polymer volume fraction, ϕ_p, where the viscosity diverges to infinity at the glass transition concentration, $\phi^\dagger$:

$$\eta = A \exp\left(\frac{\gamma}{\phi^\dagger - \phi_p}\right) \tag{B.5}$$

where γ is a non-negative parameter that controls the growth rate of the viscosity towards the glass transition. Requiring that the mixture viscosity simplify to the viscosity of the nonsolvent at zero polymer concentration, *i.e.,* $\phi_p = 0 \rightarrow \eta = \eta_n$, we set the value of the prefactor, A, as

$$A = \eta_n \exp\left(\frac{-\gamma}{\phi^\dagger}\right). \tag{B.6}$$

The pure solvent viscosity, η_s, is not in the model as we implicitly assume $\eta_n = \eta_s$. Note that for $\gamma = 0$, Eq. B.5 simplifies to a constant mixture viscosity of η_n, *i.e.,* our fluid model becomes Newtonian for $\gamma = 0$.

Numerical treatment of this diverging viscosity model is problematic as the largest numerical value a computer can represent is finite. To deal with this issue, we capped the largest non-dimensional viscosity in our simulations to $\eta/\eta_n = 10^{300}$, *i.e.,* we treat this numerical value of the viscosity as equivalent to infinity. Since our code and hardware limit practical simulations to 10^6 non-dimensional time units, such a large value is more than large enough to represent a true diverging viscosity. In fact, using this strategy allowed Model B simulations without problem. However, the unbounded exponential growth of the viscosity pushes the relevant physical time-scales beyond the simulation times accessible with our current computational tools, *i.e.,* the VFTH model slows down phase separation dynamics to the point where we can no longer observe any phenomena of interest.

The challenge of using the VFTH model is exacerbated in Model H. Capping the maximum viscosity allowed solution of the convection-diffusion equation; however, our current algorithm to solve the velocities from the momentum equation failed to converge when using the VFTH model.

Although Eq B.5 is closer to the viscosity-composition relationship observed in experiments, we found that our current numerical methods are not well-suited for its adoption.

Further developments to our numerical methods are necessary to adopt the VFTH model for the glass transition mechanism.

B.7 Time-stepping algorithms

We explored the use of more accurate time-stepping algorithms to stabilize our simulations in the presence of fluctuations. As described in Section 2.6, we implemented the semi-implicit forward Euler as our default time-stepping scheme. Given the PDE, $\partial_t \phi = L(\phi) + N(\phi)$, where L and N respectively represent the linear and non-linear terms of the right-hand side of the original PDE, we discretized the PDE in time as,

$$\frac{\phi^{n+1} - \phi^n}{\Delta t} = L\big(\phi^{n+1}\big) + N(\phi^n). \tag{B.7}$$

We treated the linear terms of the equation implicitly, taking these terms as determined by the future time-step values, ϕ^{n+1}, and the nonlinear terms explicitly, as determined by the current time-step values, ϕ^n. To improve the accuracy of our default time-stepper, we implemented four versions of a predictor-corrector scheme[85, 86]. In each of the following equations, the sub-equation (a) refers to the predictor step, calculating the intermediate "predicted" value, ϕ^*, and the sub-equation (b) refers to the corrector step, designed to improve the initial prediction and calculate the future value, ϕ^{n+1}.

$$\frac{\phi^* - \phi^n}{\Delta t} = L(\phi^*) + N(\phi^n) \tag{B.8a}$$

$$\frac{\phi^{n+1} - \phi^n}{\Delta t} = \frac{1}{2}\left[L\big(\phi^{n+1}\big) + N(\phi^*) + L(\phi^n) + N(\phi^n)\right] \tag{B.8b}$$

$$\frac{\phi^* - \phi^n}{\Delta t} = L(\phi^*) + N(\phi^n) \tag{B.9a}$$

$$\frac{\phi^{n+1} - \phi^n}{\Delta t} = L\big(\phi^{n+1}\big) + \frac{1}{2}\left[N(\phi^*) + N(\phi^n)\right] \tag{B.9b}$$

$$\frac{\phi^* - \phi^n}{\Delta t} = L(\phi^n) + N(\phi^n) \tag{B.10a}$$

$$\frac{\phi^{n+1} - \phi^n}{\Delta t} = \frac{1}{2}\left[L\big(\phi^{n+1}\big) + N(\phi^*) + L(\phi^n) + N(\phi^n)\right] \tag{B.10b}$$

$$\frac{\phi^* - \phi^n}{\Delta t} = L(\phi^n) + N(\phi^n) \tag{B.11a}$$

$$\frac{\phi^{n+1} - \phi^n}{\Delta t} = \frac{1}{2}\left[L(\phi^*) + N(\phi^*) + L(\phi^n) + N(\phi^n)\right] \tag{B.11b}$$

Each predictor-corrector scheme is twice as expensive as the single-step semi-implicit forward Euler; however, the increased accuracy could allow the use of larger Δt, and reduce computation cost in total. For example, if we can maintain the same level of accuracy for $10\Delta t$, then in total we can reduce computational cost by a factor of five. Aside from these predictor-corrector schemes, we also explored the use of a multi-step

method:

$$\frac{3\phi^{n+1} - 4\phi^n + \phi^{n-1}}{2\Delta t} = L\big(\phi^{n+1}\big) + 2N(\phi^n) - N\big(\phi^{n-1}\big) \tag{B.12}$$

The semi-implicit backward differentiation formula (SBDF) shown above was reported to perform well in solving Cahn-Hilliard equations with small noise amplitudes[87]. Unlike the predictor-corrector schemes, SBDF only needs one step, but does require additional memory as a multi-step method. Implementing adaptive time-stepping with this scheme is more challenging.

We tested these time-stepping schemes for a ternary system in a 2D bulk quench. The polymer size was set at $N_p = 50$ and the small-molecule sizes at $N_n = N_s = 1$. Interaction parameters were set at $\chi_{pn} = 1.1$, $\chi_{ps} = \chi_{ns} = 0$ and the gradient coefficients at $\kappa_p = \kappa_n = 2.5$. We initialized the system at a homogeneous composition of $\phi_p = 0.1$, $\phi_n = 0.5$ and introduced uniform noise using the same random seed for all tests. We used the Rouse mobility model without any viscosity-scaling and fluctuations were not enabled. Figure B.7 reports performance for these various time-steppers. We use the structure factor measured for one point in k-space at a specific time, $S(q = 0.443, t = 1 \times 10^2)$, as metric for the accuracy of these schemes. Figure B.8 shows the microstructure at $t = 1 \times 10^2$. As shown in Figure B.7, for small enough time-step sizes, $\Delta t \leq 1 \times 10^{-4}$, all schemes collapse on the same point, representing the accurate value of the metric. As Δt is increased, deviation from the accurate value also increases. Surprisingly, schemes in Eqs. B.8, B.10, and B.11 (not shown in Figure B.7) all have limited stabilities. The maximum usable time-step for each of these three schemes are $\Delta t = 5 \times 10^{-3}$, 1×10^{-3}, and 1×10^{-4}, respectively. Though these 3 schemes are more accurate than the forward Euler scheme when stable, their limited stabilities also limit their practical use. We

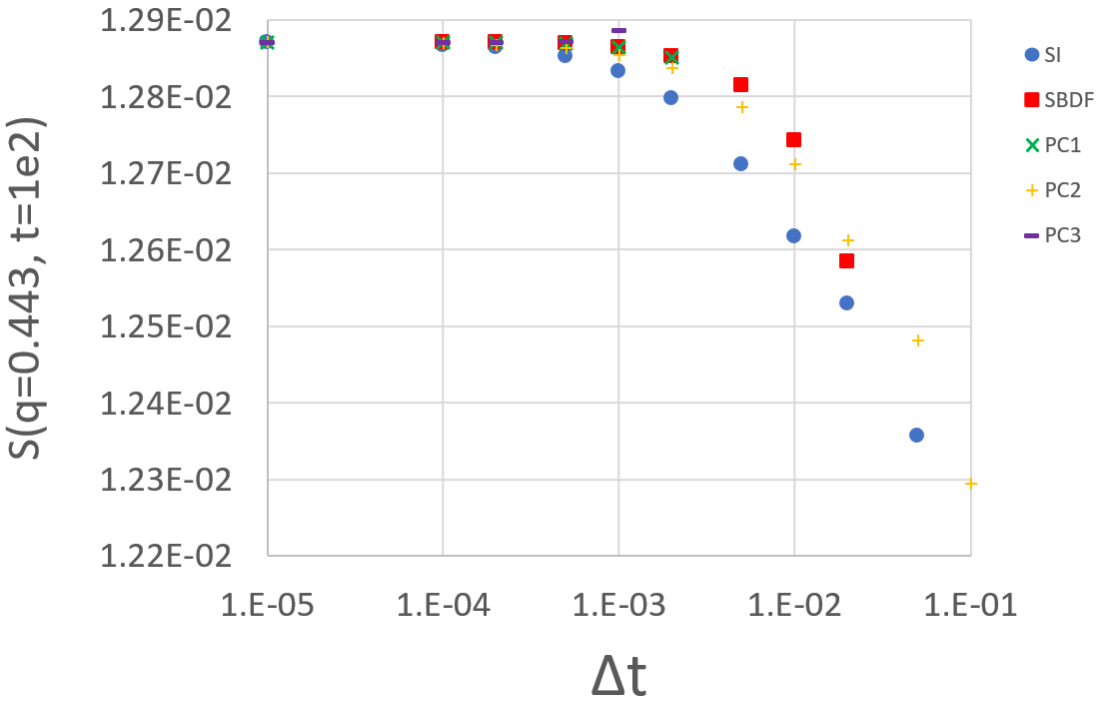

Figure B.7: The calculated structure factor, S, at $q = 0.443$ and $t = 1 \times 10^2$ for different simulation time-step sizes, Δt. As expected, all curves collapse to the same point for small-enough Δt. SI (blue circles) is Eq. B.7, SBDF (red squares) is Eq. B.12, PC1 (green x) is Eq. B.8, PC2 (yellow +) is Eq. B.9, and PC3 (purple -) is Eq. B.10.

attribute their instabilities to the linear term taken explicitly in the respective corrector steps of these schemes. In fact, the instability ceases to be an issue when we take all linear terms implicitly as done in Eq. B.9. Unfortunately, doing so breaks the symmetric form of the trapezoidal rule—the basis of the corrector step—leading to a loss of accuracy. The SBDF scheme proves to be more stable than the predictor-corrector schemes (except for Eq. B.9) since all linear terms are also taken implicitly. Nevertheless, SBDF still does not afford enough accuracy improvement to use fluctuations at full strength, *i.e.,* none of our methods so far allow us to turn fluctuations on with a reduction factor of one.

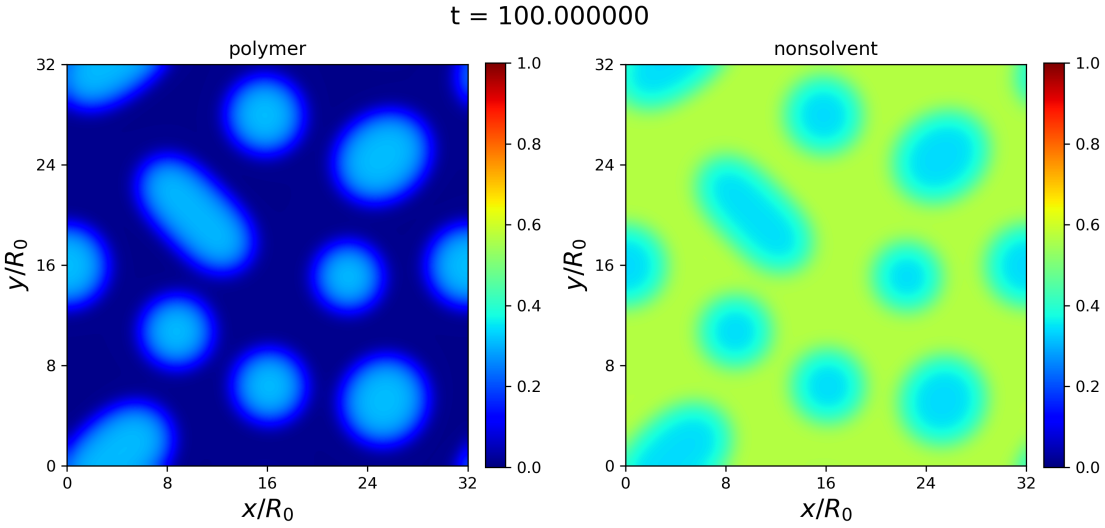

Figure B.8: The microstructure at $t = 100$ for $\Delta t = 1 \times 10^{-4}$. This specific image was taken from the test of the SBDF stepper (Eq. B.12), but microstructures are indistinguishable with the naked eye for different time steppers at $\Delta t = 1 \times 10^{-4}$.

Bibliography

[1] R. Connor, S. Uhlenbrook, and E. Koncaguel, *The United Nations world water development report 2019: leaving no one behind, executive summary*, tech. rep., UNESCO World Water Assessment Programme, 2019.

[2] M. Elimelech and W. A. Phillip, *The future of seawater desalination: Energy, technology, and the environment*, *Science* **333** (2011), no. 6043 712–717.

[3] V. G. Gude, *Desalination and sustainability - An appraisal and current perspective*, *Water Research* **89** (2016) 87–106.

[4] D. M. Warsinger, S. Chakraborty, E. W. Tow, M. H. Plumlee, C. Bellona, S. Loutatidou, L. Karimi, A. M. Mikelonis, A. Achilli, A. Ghassemi, L. P. Padhye, S. A. Snyder, S. Curcio, C. D. Vecitis, H. A. Arafat, and J. H. Lienhard, *A review of polymeric membranes and processes for potable water reuse*, *Progress in Polymer Science* **81** (2018) 209–237.

[5] C. Y. Tang, Z. Yang, H. Guo, J. J. Wen, L. D. Nghiem, and E. Cornelissen, *Potable Water Reuse through Advanced Membrane Technology*, *Environmental Science and Technology* **52** (2018), no. 18 10215–10223.

[6] R. W. Baker, *Membrane Technology and Applications*. John Wiley and Sons, Ltd, West Sussex, United Kingdom, 3rd ed., 2012.

[7] S. Loeb and S. Sourirajan, *High flow porous membranes for separating water from saline solutions (US 3,133,132)*, 1964.

[8] H. Strathmann, *Membranes and membrane separation processes, 1. Principles*, *Ullmann's Encyclopedia of Industrial Chemistry* (2011) 457–480.

[9] R. E. Kesting, *Synthetic polymeric membranes*. Wiley-Interscience, 2nd ed., 1985.

[10] I. Pinnau and B. D. Freeman, *Formation and Modification of Polymeric Membranes: Overview*, *Membrane Formation and Modification* **744** (1999) 1.

[11] A. Venault, Y. Chang, D.-M. Wang, and D. Bouyer, *A Review on Polymeric Membranes and Hydrogels Prepared by Vapor-Induced Phase Separation Process*, *Polym. Rev.* **53** (2013), no. 4 568–626.

[12] G. R. Guillen, Y. Pan, M. Li, and E. M. V. Hoek, *Preparation and Characterization of Membranes Formed by Nonsolvent Induced Phase Separation: A Review*, *Industrial and Engineering Chemistry Research* **50** (2011) 3798–3817.

[13] D.-M. Wang and J.-Y. Lai, *Recent advances in preparation and morphology control of polymeric membranes formed by nonsolvent induced phase separation*, *Current Opinion in Chemical Engineering* **2** (2013), no. 2 229–237.

[14] C. A. Smolders, A. J. Reuvers, R. M. Boom, and I. M. Wienk, *Microstructures in phase-inversion membranes. Part 1. Formation of macrovoids*, *Journal of Membrane Science* **73** (1992), no. 2-3 259–275.

[15] H. Strathmann, K. Kock, P. Amar, and R. W. Baker, *The formation mechanism of asymmetric membranes*, *Desalination* **16** (1975), no. 2 179–203.

[16] H. Strathmann, P. Scheible, and R. W. Baker, *A rationale for the preparation of Loeb-Sourirajan-type cellulose acetate membranes*, *Journal of Applied Polymer Science* **15** (1971), no. 4 811–828.

[17] H. Strathmann and K. Kock, *The formation mechanism of phase inversion membranes*, *Desalination* **21** (1977), no. 3 241–255.

[18] J. G. Wijmans and C. A. Smolders, *Preparation of asymmetric membranes by the phase inversion process*, in *Synthetic Membranes: Science, Engineering and Applications* (P. M. Bungay, H. K. Lonsdale, and M. N. de Pinho, eds.), pp. 39–56. D. Reidel Publishing Company, Dordrecht, Holland, 1983.

[19] L. Broens, F. W. Altena, C. A. Smolders, and D. M. Koenhen, *Asymmetric membrane structures as a result of phase separation phenomena*, *Desalination* **32** (1980), no. C 33–45.

[20] F. W. Altena and C. A. Smolders, *Calculation of liquid-liquid phase separation in a ternary system of a polymer in a mixture of a solvent and a nonsolvent*, *Macromolecules* **15** (1982), no. 6 1491–1497.

[21] C. Cohen, G. B. Tanny, and S. Prager, *Diffusion-controlled formation of porous structures in ternary polymer systems*, *Journal of Polymer Science: Polymer Physics Edition* **17** (1979), no. 3 477–489.

[22] A. J. Reuvers, F. W. Altena, and C. A. Smolders, *Demixing and gelation behavior of ternary cellulose acetate solutions*, *J. Polym. Sci. Part B Polym. Phys.* **24** (1986), no. 4 793–804.

[23] L. Yilmaz and A. J. McHugh, *Modelling of asymmetric membrane formation. I. Critique of evaporation models and development of a diffusion equation formalism for the quench period*, *Journal of Membrane Science* **28** (1986), no. 3 287–310.

[24] L. Yilmaz and A. J. McHugh, *Modeling of Asymmetric Membrane Formation. II. The Effects of Surface Boundary Conditions*, *Journal of Applied Polymer Science* **35** (1988) 1967–1979.

[25] A. J. Reuvers and C. A. Smolders, *Formation of membranes by means of immersion precipitation Part II. The mechanism of formation of membranes prepared from the system cellulose acetate-acetone-water*, *Journal of Membrane Science* **34** (1987) 67–86.

[26] C. S. Tsay and A. J. Mchugh, *Mass transfer modeling of asymmetric membrane formation by phase inversion*, *J. Polym. Sci. Part B Polym. Phys.* **28** (1990), no. 8 1327–1365.

[27] P. Radovanovic, S. W. Thiel, and S. T. Hwang, *Formation of asymmetric polysulfone membranes by immersion precipitation. Part II. The effects of casting solution and gelation bath compositions on membrane structure and skin formation*, *J. Memb. Sci.* **65** (1992), no. 3 231–246.

[28] L.-P. Cheng, Y. S. Soh, A.-H. Dwan, and C. C. Gryte, *An improved model for mass transfer during the formation of polymeric membranes by the immersion-precipitation process*, *Journal of Polymer Science Part B: Polymer Physics* **32** (1994), no. 8 1413–1425.

[29] J. U. Garcia, T. Iwama, E. Y. Chan, D. R. Tree, K. T. Delaney, and G. H. Fredrickson, *Mechanisms of asymmetric membrane formation in nonsolvent-induced phase separation*, *ACS Macro Letters* **9** (2020), no. 11 1617–1624.

[30] A. Akthakul, C. E. Scott, A. M. Mayes, and A. J. Wagner, *Lattice Boltzmann simulation of asymmetric membrane formation by immersion precipitation*, *Journal of Membrane Science* **249** (2005), no. 1-2 213–226.

[31] M. Hopp-Hirschler and U. Nieken, *Modeling of pore formation in phase inversion processes: Model and numerical results*, *Journal of Membrane Science* **564** (2018), no. August 820–831.

[32] B. Zhou and A. C. Powell, *Phase field simulations of early stage structure formation during immersion precipitation of polymeric membranes in 2D and 3D*, *J. Memb. Sci.* **268** (2006), no. 2 150–164.

[33] D. R. Tree, K. T. Delaney, H. D. Ceniceros, T. Iwama, and G. H. Fredrickson, *A multi-fluid model for microstructure formation in polymer membranes*, *Soft Matter* **13** (2017), no. 16 3013–3030.

[34] D. R. Tree, L. F. Dos Santos, C. B. Wilson, T. R. Scott, J. U. Garcia, and G. H. Fredrickson, *Mass-transfer driven spinodal decomposition in a ternary polymer solution*, *Soft Matter* **15** (2019), no. 23 4614–4628.

[35] L.-Q. Chen, *Phase-Field Models for Microstructure Evolution*, *Annual Review of Materials Research* **32** (2002), no. 1 113–140.

[36] V. Badalassi, H. Ceniceros, and S. Banerjee, *Computation of multiphase systems with phase field models*, *Journal of Computational Physics* **190** (2003), no. 2 371–397.

[37] P. G. de Gennes, *Dynamics of Entangled Polymer Solutions. I. The Rouse Model*, *Macromolecules* **9** (1976), no. 4 587–593, [1011.1669].

[38] M. Doi and A. Onuki, *Dynamic coupling between stress and composition in polymer solutions and blends*, *J. Phys. II France* **2** (1992) 1631–1656.

[39] P. J. Flory, *Principles of Polymer Chemistry*. Cornell University Press, Ithaca, NY, 1953.

[40] P. G. de Gennes, *Dynamics of fluctuations and spinodal decomposition in polymer blends*, *J. Chem. Phys.* **72** (1981), no. 9 4756–4763, [1011.1669].

[41] P. C. Hohenberg and B. I. Halperin, *Theory of dynamic critical phenomena*, *Reviews of Modern Physics* **49** (1977), no. 3 435–479.

[42] P. C. Hiemenz and T. P. Lodge, *Polymer Chemistry*. CRC Press, Boca Raton, 2nd ed., 2007.

[43] R. Shimizu and H. Tanaka, *A novel coarsening mechanism of droplet spinodal decomposition*, *Nature Communications* **6** (2015), no. 7407 1–11, [arXiv:1509.0338].

[44] G. H. Fredrickson, *The Equilibrium Theory of Inhomogeneous Polymers*. Oxford University Press, 2006.

[45] H. D. Ceniceros and G. H. Fredrickson, *Numerical Solution of Polymer Self-Consistent Field Theory*, *Multiscale Model. Simul.* **2** (2004), no. 3 452–474.

[46] M. M. Pendergast and E. M. Hoek, *A review of water treatment membrane nanotechnologies*, *Energy and Environmental Science* **4** (2011), no. 6 1946–1971.

[47] M. R. Landsman, R. Sujanani, S. H. Brodfuehrer, C. M. Cooper, A. G. Darr, R. J. Davis, K. Kim, S. Kum, L. K. Nalley, S. M. Nomaan, C. P. Oden, A. Paspureddi, K. K. Reimund, L. S. Rowles, S. Yeo, D. F. Lawler, B. D. Freeman, and L. E. Katz, *Water Treatment: Are Membranes the Panacea?*, *Annual review of chemical and biomolecular engineering* **11** (2020) 559–585.

[48] D. R. Tree, T. Iwama, K. T. Delaney, J. Lee, and G. H. Fredrickson, *Marangoni Flows during Nonsolvent Induced Phase Separation*, *ACS Macro Letters* **7** (2018), no. 5 582–586.

[49] M. R. Cervellere, Y. Tang, X. Qian, D. M. Ford, and P. C. Millett, *Mesoscopic simulations of thermally-induced phase separation in PVDF/DPC solutions*, *Journal of Membrane Science* (2019).

[50] P. van de Witte, P. J. Dijkstra, J. W. a. van den Berg, and J. Feijen, *Phase separation processes in polymer solutions in relation to membrane formation*, *Journal of Membrane Science* **117** (1996), no. 1-2 1–31.

[51] S. G. Li, T. Van De Boomgaard, C. A. Smolders, and H. Strathmann, *Physical gelation of amorphous polymers in a mixture of solvent and nonsolvent*, *Macromolecules* **29** (1996), no. 6 2053–2059.

[52] J. Y. Kim, Y. D. Kim, T. Kanamori, H. K. Lee, K.-j. Baik, and S. C. Kim, *Vitrification Phenomena in Polysulfone / NMP / Water System*, *Journal of Applied Polymer Science* **71** (1998) 431–438.

[53] R. C. Ball and R. L. Essery, *Spinodal decomposition and pattern formation near surfaces*, *Journal of Physics: Condensed Matter* **2** (1990), no. 51 10303–10320.

[54] I. Lifshitz and V. Slyozov, *The kinetics of precipitation from supersaturated solid solutions*, *Journal of Physics and Chemistry of Solids* **19** (apr, 1961) 35–50.

[55] C. Wagner, *Theorie der alterung von niederschlagen durch umlosen (Ostwald-reifung)*, *Zeitschrift fur elektrochemie* (1961), no. 7-8 581–591.

[56] D. M. Koenhen, M. H. V. Mulder, and C. A. Smolders, *Phase separation phenomena during the formation of asymmetric membranes*, *Journal of Applied Polymer Science* **21** (1977), no. 1 199–215.

[57] J. G. Wijmans, J. P. B. Baaij, and C. A. Smolders, *The mechanism of formation of microporous or skinned membranes produced by immersion precipitation*, *Journal of Membrane Science* **14** (1983), no. 3 263–274.

[58] J. G. Wijmans, J. Kant, M. H. V. M, and C. A. Smolders, *Phase separation phenomena in solutions of polysulfone in mixtures of a solvent and a nonsolvent : relationship with membrane formation*, *Polymer* **26** (1985) 1539–1545.

[59] H. H. Wang, J. T. Jung, J. F. Kim, S. Kim, E. Drioli, and Y. M. Lee, *A novel green solvent alternative for polymeric membrane preparation via nonsolvent-induced phase separation (NIPS)*, *Journal of Membrane Science* **574** (2019) 44–54.

[60] A. J. McHugh and C. S. Tsay, *Dynamics of the Phase Inversion Process*, *J. Appl. Polym. Sci.* **46** (1992) 2011–2021.

[61] V. F. Cardoso, G. Botelho, and S. Lanceros-Méndez, *Nonsolvent induced phase separation preparation of poly(vinylidene fluoride-co-chlorotrifluoroethylene) membranes with tailored morphology, piezoelectric phase content and mechanical properties*, *Materials and Design* **88** (2015) 390–397.

[62] J. T. Jung, J. F. Kim, H. H. Wang, E. di Nicolo, E. Drioli, and Y. M. Lee, *Understanding the non-solvent induced phase separation (NIPS) effect during the fabrication of microporous PVDF membranes via thermally induced phase separation (TIPS)*, *Journal of Membrane Science* **514** (2016) 250–263.

[63] K. R. Castleman, *Digital Image Processing*. Prentice-Hall, 1979.

[64] D. Stauffer, *Introduction to percolation theory*. Taylor and Francis, London, 1985.

[65] E. D. Siggia, *Late stages of spinodal decomposition in binary mixtures*, *Physical Review A* **20** (aug, 1979) 595–605.

[66] H. Tanaka, *Viscoelastic phase separation*, *J. Phys.: Condens. Matter* **12** (2000) R207—-R264.

[67] D. M. Wang, F. C. Lin, T. T. Wu, and J. Y. Lai, *Formation mechanism of the macrovoids induced by surfactant additives*, *J. Memb. Sci.* **142** (1998), no. 2 191–204.

[68] A. Venault, Y. Chang, D.-m. Wang, D. Bouyer, A. Higuchi, and J.-y. Lai, *PEGylation of anti-biofouling polysulfone membranes via liquid- and vapor-induced phase separation processing*, *J. Memb. Sci.* **403-404** (2012) 47–57.

[69] A. Venault, Y. Chang, D.-M. Wang, and J.-Y. Lai, *Surface anti-biofouling control of PEGylated poly (vinylidene fluoride) membranes via vapor-induced phase separation processing*, *J. Memb. Sci.* **423-424** (2012) 53–64.

[70] A. Venault, Y.-h. Liu, J.-r. Wu, H.-S. Yang, and Y. Chang, *Low-biofouling membranes prepared by liquid-induced phase separation of the PVDF/polystyrene-b-poly(ethylene glycol) methacrylate blend*, *J. Memb. Sci.* **450** (2014) 340–350.

[71] C. Y. Feng, K. C. Khulbe, T. Matsuura, and A. F. Ismail, *Recent progresses in polymeric hollow fiber membrane preparation, characterization and applications*, *Separation and Purification Technology* **111** (2013) 43–71.

[72] N. Peng, N. Widjojo, P. Sukitpaneenit, M. M. Teoh, G. G. Lipscomb, T. S. Chung, and J. Y. Lai, *Evolution of polymeric hollow fibers as sustainable technologies: Past, present, and future*, *Progress in Polymer Science* **37** (2012), no. 10 1401–1424.

[73] I. Pinnau and W. J. Koros, *A Qualitative Skin Layer Formation Mechanism for Membranes Made by Dry / Wet Phase Inversion*, *Journal of Polymer Science: Part B: Polymer Physics* **31** (1993), no. 4 419–427.

[74] S. P. Nunes and A. Car, *From Charge-Mosaic to Micelle Self-Assembly: Block Copolymer Membranes in the Last 40 Years*, *Ind. Eng. Chem. Res.* **52** (2013).

[75] E. A. Jackson and M. A. Hillmyer, *Nanoporous Membranes Derived from Block Copolymers: From Drug Delivery to Water Filtration*, *ACS Nano* **4** (2010), no. 7 3548–3553.

[76] K.-V. Peinemann, V. Abetz, and P. F. W. Simon, *Asymmetric superstructure formed in a block copolymer via phase separation*, *Nature Materials* **6** (2007), no. December.

[77] S. P. Nunes, R. Sougrat, B. Hooghan, D. H. Anjum, A. R. Behzad, L. Zhao, N. Pradeep, I. Pinnau, U. Vainio, and K.-V. Peinemann, *Ultraporous Films with Uniform Nanochannels by Block Copolymer Micelles Assembly*, *Macromolecules* (2010) 8079–8085.

[78] S. P. Nunes, M. Karunakaran, N. Pradeep, A. R. Behzad, B. Hooghan, R. Sougrat, H. He, and K.-V. Peinemann, *From Micelle Supramolecular Assemblies in Selective Solvents to Isoporous Membranes*, *Langmuir* **27** (2011) 10184–10190.

[79] S. P. Nunes, A. R. Behzad, B. Hooghan, R. Sougrat, M. Karunakaran, N. Pradeep, U. Vainio, and K.-V. Peinemann, *Switchable pH-Responsive Polymeric Membranes Prepared via Block Copolymer Micelle Assembly*, *ACS Nano* (2011), no. 5 3516–3522.

[80] R. M. Dorin, W. A. Phillip, H. Sai, J. Werner, M. Elimelech, and U. Wiesner, *Designing block copolymer architectures for targeted membrane performance*, *Polymer* **55** (2014), no. 1 347–353.

[81] M. M. Pendergast, R. M. Dorin, W. A. Phillip, U. Wiesner, and E. M. V. Hoek, *Understanding the structure and performance of self-assembled triblock terpolymer membranes*, *Journal of Membrane Science* **444** (2013) 461–468.

[82] G. Bradski, *The OpenCV Library*, *Dr. Dobb's Journal of Software Tools* (2000).

[83] L. Zeman and T. Fraser, *Formation of air-cast cellulose acetate membranes. Part I. Study of macrovoid formation*, *Journal of Membrane Science* **84** (1993), no. 1-2 93–106.

[84] L. Zeman and T. Fraser, *Formation of air-cast cellulose acetate membranes Part II. Kinetics of demixing and microvoid growth*, *Journal of Membrane Science* **87** (1994), no. 3 267–279.

[85] E. M. Lennon, G. O. Mohler, H. D. Ceniceros, C. J. Garcia-Cervera, and G. H. Fredrickson, *Numerical solutions of the Complex Langevin equations in polymer field theory*, *Multiscale Model. Simul.* **6** (2008), no. 4 1347–1370.

[86] D. Düchs, K. T. Delaney, and G. H. Fredrickson, *A multi-species exchange model for fully fluctuating polymer field theory simulations*, *Journal of Chemical Physics* **141** (2014), no. 17 [arXiv:1410.0406].

[87] H. D. Ceniceros and G. O. Mohler, *A Practical Splitting Method for Stiff SDEs with Applications to Problems with Small Noise*, *Multiscale Model. Simul.* **6** (2007), no. 1 212–227.